

School of ENGINEERING DUKE UNIVERSITY

AIR-GAPPED STRUCTURES AS MAGNETIC ELEMENTS
FOR USE IN POWER PROCESSING SYSTEMS

by

Anil Kumar Ohri

Prepared under Research Grant No. NGL 34-001-001, Supplement 16

July 6, 1977

REPRODUCED BY
NATIONAL TECHNICAL
INFORMATION SERVICE
U. S. DEPARTMENT OF COMMERCE
SPRINGFIELD, VA. 22161

(NASA-CR-153289) AIR-GAPPED STRUCTURES AS
MAGNETIC ELEMENTS FOR USE IN POWER
PROCESSING SYSTEMS Ph.D. Thesis (Duke
Univ.) 191 p HC A09/MF A01

N77-26627

CSCL 10B

G3/44

Unclas
35451



AIR-GAPPED STRUCTURES AS MAGNETIC ELEMENTS
FOR USE IN POWER PROCESSING SYSTEMS

by

Anil Kumar Ohri

July 6, 1977

Prepared under Research Grant No. NGL 34-001-001, Supplement 16

Department of Electrical Engineering

School of Engineering

Duke University

Durham, North Carolina

for

NATIONAL AERONAUTICS AND SPACE ADMINISTRATION

AIR-GAPPED STRUCTURES AS MAGNETIC ELEMENTS
FOR USE IN POWER PROCESSING SYSTEMS

by

Anil Kumar Ohri

Department of Electrical Engineering
Duke University

Date:

July 6, 1977

Approved:

Harry A. Owen, Jr.
Harry A. Owen, Jr., Supervisor

Thomas S. Wilson

W. T. Jones

Merrell L. Patrick

A dissertation submitted in partial fulfillment of
the requirements for the degree of Doctor of
Philosophy in the Department of Electrical
Engineering in the Graduate School of
Arts and Sciences of Duke University

1977

100

ABSTRACT
(Electrical Engineering)

AIR-GAPPED STRUCTURES AS MAGNETIC ELEMENTS
FOR USE IN POWER PROCESSING SYSTEMS

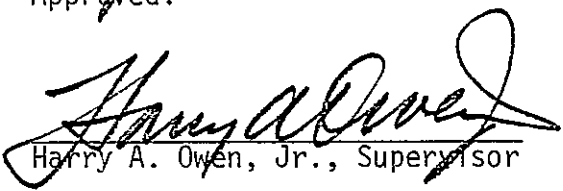
by

Anil Kumar Ohri

Department of Electrical Engineering
Duke University

Date: July 6, 1977

Approved:


Harry A. Owen, Jr., Supervisor

Thomas G. Wilson

W. T. Joines

Merrill L. Patrick

An abstract of a dissertation submitted in partial
fulfillment of the requirements for the degree
of Doctor of Philosophy in the Department of
Electrical Engineering in the Graduate
School of Arts and Sciences of
Duke University

ABSTRACT

Magnetic elements, inductors and/or transformers are among the most important elements found in electronic power processing and filter circuits. In filter circuits, the inductor is used to smooth the current flowing to the load and its output voltage. In energy-storage dc-to-dc converters used in power processing applications, the inductor or transformer is used to store and transfer energy in some controlled manner between source and load. The magnetic element is nearly always a custom designed and constructed element as opposed to other elements used in these circuits. Therefore, the design of the magnetic element is a crucial step in the design of power processing and filter circuits as a whole. In high-power applications, usually it is desirable to design these inductors using air-gapped magnetic-core structures. This dissertation presents methodical approaches to the design of inductors for use in LC-filters and dc-to-dc converters using air-gapped magnetic structures.

In addition to the design procedures for the inductors, methods for the analysis and design of full-wave rectifier LC-filter circuits operating with the inductor current in both the continuous-conduction and the discontinuous-conduction modes are presented. In the continuous-conduction mode,

linear circuit analysis techniques are employed, while in the case of the discontinuous mode, the method of analysis requires computer solutions of the piecewise-linear differential equations which describe the filter in the time domain. Using these methods of analysis, a family of design curves is obtained relating filter parameter values of inductance, capacitance, and load resistance to the performance factors of percentage output ripple voltage, average output voltage level, rms and peak transformer-winding currents, and input power factor.

Three procedures for designing filter inductors using air-gapped cores are presented. The first procedure requires digital computation to yield a design which is optimized in the sense of minimum core volume and minimum number of turns. The second procedure does not yield an optimized design as defined above, but the design can be done by hand calculations or with a small calculator. The third procedure is based on the use of specially prepared magnetic core data and provides an easy way to quickly reach a workable design.

The procedure for designing air-gapped energy-storage reactors for dc-to-dc converters is based on an earlier study of the storage and transfer of energy in the magnetic reactors. The continuation of a study in this direction leads to a simple relationship for the required minimum volume of the air gap. Determination of this minimum air-gap volume then permits the selection of either an air-gap length or a cross-sectional core area, thus identifying a workable magnetic structure.

It is believed that the analytical guidance in conjunction with the design procedures presented in this dissertation can significantly reduce

the time, and hence the cost, of designing full-wave rectifier LC-filter circuits, air-gapped magnetic-core inductors for use in filters, and energy-storage reactors in dc-to-dc converters using air-gapped magnetic structures.

ACKNOWLEDGEMENTS

This research was supported by Research Grant NGL-34-001-001 from the National Aeronautic and Space Administration, Washington, D.C. to Duke University. The technical liaison was conducted by the Space Technology Division, Engineering Directorate of the Goddard Space Flight Center, Greenbelt, Maryland.

I would like to express my deepest appreciation to Dr. Harry A. Owen, Jr., and Dr. Thomas G. Wilson, both my professors, for their guidance and constant inspiration throughout the course of my graduate study. Their advice and efforts have been most important in the development and in the writing of this dissertation.

I would also like to thank Mr. Steve Huffman, my friend, for his proofreading of this dissertation; Mr. Jimmy Hartley, laboratory assistant, for his drafting work; and to Ms. Gladys Weeks for her typing.

Last, but not the least, my appreciation goes to my parents and my wife. Their love, patience, inspiration and understanding have always been with me and have made this work possible.

Anil Kumar Ohri

CONTENTS

ABSTRACT	iii
ACKNOWLEDGEMENT	vi
LIST OF FIGURES	x
LIST OF TABLES	xiii
I. INTRODUCTION	2
II. ANALYSIS AND DESIGN OF FULL-WAVE RECTIFIER LC FILTERS WITH CONTINUOUS OR DISCONTINUOUS INDUCTOR CURRENT	7
2.1 Introduction ,7	
2.2 Circuit Analysis , 10	
2.2.1 Continuous-Conduction Mode , 10	
2.2.2 Discontinuous-Conduction Mode , 13	
2.2.3 Algorithm to Determine Steady-State Values of v_0 and i_x , 16	
2.2.4 Critical Condition , 19	
2.2.5 Relationship Between κ , ω_N , Q , ξ , and ω , 22	
2.2.6 Power Factor , 22	
2.3 Design and Performance Curves and Approximate Relationships	
2.3.1 Design and Performance Curves , 23	
2.3.2 Approximate Analytical Design Relationships , 26	
2.4 Design Examples , 28	
2.5 Conclusions , 32	
III. ANALYSIS AND DESIGN OF LC-FILTERS WITH NON-ZERO SOURCE IMPEDANCE	34
3.1 Introduction , 34	
3.2 Circuit Analysis , 36	
3.2.1 Continuous-Conduction Mode , 36	
3.2.2 Discontinuous-Conduction Mode , 38	
3.2.3 Critical Condition , 41	
3.3 Design and Performance Curves and Approximate Relationships , 42	

3.3.1	Design and Performance Curves , 42	
3.3.2	Approximate Analytical Design Relationships , 52	
3.4	Design Example , 54	
3.4.1	Example , 57	
3.4.2	Example Using Approximate Design Relationships, 61	
3.5	Conclusions, 63	
IV.	DESIGN OF AIR-GAPPED MAGNETIC-CORE INDUCTORS FOR SUPER-IMPOSED DIRECT AND ALTERNATING CURRENTS	65
4.1	Introduction, 65	
4.2	Design Requirements, 67	
4.3	Analysis, 68	
4.4	Design Procedures, 75	
4.4.1	Flow Chart 1, 76	
4.4.2	Flow Chart 2, 78	
4.4.3	Flow Chart 3, 83	
4.5	Example to Illustrate the Design Procedure, 86	
4.6	Conclusions, 89	
V.	DESIGN OF AIR-GAPPED INDUCTORS USING SPECIALLY PREPARED MAGNETIC CORE DATA	91
5.1	Introduction, 91	
5.2	Design Relationships Used in Generating Hanna's Curves, 92	
5.3	Design Relationships when AC Flux Excursions Are Large, 98	
5.4	Design Curves, 100	
5.5	Design Procedure, 105	
5.5.1	Example Using New Design Curve, 107	
5.5.2	Example Using Hanna's Curve, 108	
5.6	Comparison with Hanna's Method , 110	
5.7	Experimental Verifications, 110	
5.8	Conclusions, 111	
VI.	DESIGN OF ENERGY-STORAGE REACTORS FOR DC-TO-DC CONVERTERS USING AIR-GAPPED MAGNETIC-CORE STRUCTURES	113
6.1	Introduction, 113	
6.2	Analysis of the Magnetic Circuit , 115	
6.3	Design Procedure , 119	
6.4	Conclusion , 124	
VII.	CONCLUSIONS AND SUGGESTIONS FOR FUTURE RESEARCH	126
7.1	Conclusions , 126	
7.2	Suggestions for Future Research , 128	
APPENDIX A.	DERIVATION OF EXPRESSIONS FOR THE LC FILTER OPERATING IN THE CONTINUOUS-CONDUCTION MODE, CHAPTER II	131

APPENDIX B.	DERIVATION OF EXPRESSIONS FOR THE LC FILTER OPERATING IN THE DISCONTINUOUS-CONDUCTION MODE, CHAPTER II	135
B.1	Diodes Conducting, 135	
B.1.1	Solution for v_{Q1} , 136	
B.2	Diodes not Conducting, 139	
APPENDIX C.	DERIVATION OF EXPRESSIONS FOR THE LC FILTER WITH NON-ZERO SOURCE IMPEDANCE OPERATING IN THE CONTINUOUS-CONDUCTION MODE, CHAPTER III	141
APPENDIX D.	DERIVATION OF EXPRESSIONS FOR THE LC FILTER WITH NON-ZERO SOURCE IMPEDANCE OPERATING IN THE DISCONTINUOUS-CONDUCTION MODE, CHAPTER III	144
APPENDIX E.	DERIVATION OF $F_1(\hat{B}_{mAC}, \mu_\Delta, H_{mQ}, L, I_{DC}, V_{AC}, f, (\ell_m, A_m) = 0$, CHAPTER IV	148
APPENDIX F.	DERIVATION OF THE SCREENING RULE FOR A PHYSICALLY REALIZABLE AIR GAP, CHAPTER IV	151
APPENDIX G.	DISCUSSION ON THE QUADRATIC ROOTS FOR ℓ_g , CHAPTER IV	155
APPENDIX H.	ALGORITHM FOR GENERATING DESIGN CURVES FOR AIR-GAPPED INDUCTORS, CHAPTER V	157
H.1	Flow Chart, 157	
LIST OF REFERENCES		161
GLOSSARY OF SYMBOLS		165

LIST OF FIGURES

FIGURES	PAGE
2.1. LC-filter circuit supplied by (A) center-tapped transformer rectifier and (B) full-wave bridge rectifier.	8
2.2. (A) Equivalent diagram for the rectifier-filter circuits operating in the continuous-conduction mode.	11
(B) Associated voltage and current waveforms from computer solutions of circuit equations.	11
2.3. Equivalent diagrams for the rectifier-filter circuits operating in the discontinuous-conduction mode during interval (A) when diodes are conducting and (B) when diodes are not conducting. (C) Associated voltage and current waveforms from computer solutions of circuit equations.	14
2.4. Flow-chart of algorithm for rapid determination of the periodic steady-state of the rectifier-filter circuit operating in the discontinuous-conduction mode.	17
2.5. Plot of κ_{cr} versus ω_N and identification regions.	21
2.6. Design and performance curves for LC-filters operating both in the continuous- and discontinuous-conduction modes.	24
3.1. LC-filter circuit with non-zero source impedance R_I and L_I supplied by (A) center-tapped transformer rectifier and (B) full-wave bridge rectifier.	35
3.2. (A) Equivalent diagram for the rectifier-filter circuits with non-zero source impedance operating in the continuous-conduction mode.	37

(B)	Associated voltage and current waveforms from computer solutions of circuit equations.	37
3.3.	Equivalent diagrams for the rectifier-filter circuits with non-zero source impedance operating in the discontinuous-conduction mode during interval (A) when diodes are conducting and (B) when diodes are not conducting. (C) Associated voltage and current waveforms from computer solutions of circuit equations.	39
3.4.	Plot of κ_{Cr} versus ω_N for various values of $\rho = R_I/R_L$.	43
3.5.	Design and performance curves for LC-filters with $\rho = 0.0005$ operating both in the continuous- and discontinuous-conduction modes.	44
3.6.	Design and performance curves for LC-filters with $\rho = .01$ operating both in the continuous- and discontinuous-conduction modes.	45
3.7.	Design and performance curves for LC-filters with $\rho = .05$ operating both in the continuous- and discontinuous-conduction modes.	46
3.8.	Design and performance curves for LC-filters with $\rho = 0.1$ operating both in the continuous- and discontinuous-conduction modes.	47
3.9.	Design and performance curves for LC-filters with $\rho = 0.2$ operating both in the continuous- and discontinuous-conduction modes.	48
3.10.	Design and performance curves for LC-filters with $\rho = 0.3$ operating both in the continuous- and discontinuous-conduction modes.	49
3.11.	Design and performance curves for LC-filters with $\rho = 0.4$ operating both in the continuous- and discontinuous-conduction modes.	50
3.12.	Design and performance curves for LC-filters with $\rho = 0.5$ operating both in the continuous- and discontinuous-conduction modes.	51
4.1.	Type "C" core with associated winding.	69
4.2.	Curve 1: negative air gap line. Curve 2: normal magnetization curve.	71
4.3.	Relative incremental permeability versus peak value of sinusoidal flux density excursion for various values of H_{mQ} on normal magnetization curve for 3-percent grain-oriented silicon steel.	73

4.4.	Flow chart 1: algorithm for computing N and g .	77
4.5.	Flow chart 2: algorithm for optimized inductor design.	79
4.6.	Illustration of use of data-base points to calculate $\mu_{\Delta, \min}$ and $\mu_{\Delta, \max}$ for a trial value of H_{mQ} lying between $H_m(K-1)$ and $H_m(K)$. Also, illustration of the two iterations used to obtain a value of μ_{Δ} for an arbitrary trial H_{mQ} and $\hat{B}_{mAC, \text{trial}}$. X are the experimentally determined incremental permeability data points stored as a part of the data base. \odot are six data-base points nearest to the trial value of H_{mQ} used to calculate $\mu_{\Delta, \min}$ corresponding to $\hat{B}_{mAC, \min}$, and six points used to calculate $\mu_{\Delta, \max}$ corresponding to $\hat{B}_{mAC, \max}$. \circ are the values of μ_{Δ} for $\hat{B}_{mAC, \text{trial}}$ obtained by interpolation for the six values of H_m in the data base closest to the trial value of H_{mQ} . \square are the values of $\mu_{\Delta, \min}$, $\mu_{\Delta, \max}$, and the trial value of μ_{Δ} obtained by interpolation using the \odot and \circ values.	82
4.7.	Flow chart 3: algorithm for screening cores for physically realizable air gap.	84
5.1.	Relative incremental permeability versus dc operating point H_{mQ} on normal magnetization curve for small values of ac flux excursions.	94
5.2.	Example of Hanna's curves generated by computer program for 3-percent grain-oriented silicon steel.	95
5.3.	Example of Hanna's curves generated by computer program for Permalloy 80	96
5.4.	Example of Hanna's curves generated by computer program for Supermendur.	97
5.5.	Design curves for 3-percent grain-oriented silicon steel which take finite ac flux excursions into account.	101
5.6	Design curves for Permalloy 80 which take finite ac flux excursions into account.	102
5.7	Design curves for Supermendur which take finite ac flux excursions into account.	103
6.1	Four energy-storage dc-to-dc converters. (A) Single-winding voltage stepup. (B) Single-winding current stepup. (C) Single-winding voltage stepup/current stepup. (D) Two-winding voltage stepup/current stepup.	114
H.1	Flow chart illustrating the algorithm for calculating the optimum quiescent point $H_{mQ, \text{opt}}$, and generating design curves for various air-gap ratios.	158

LIST OF TABLES

Tables	Page
2.1. Approximate design and performance relationships for LC-filter operating both in the continuous- and discontinuous-conduction modes.	27
3.1. Approximate design and performance relationships for LC-filters with non-zero source impedance operating in the continuous-conduction mode.	53
3.2. Approximate design and performance relationships for LC-filters with non-zero source impedance operating in the discontinuous-conduction mode.	55
3.3. Values for the various coefficients which introduce the dependency on p in the approximate analytical relationships given in Table 3.2.	56

AIR-GAPPED STRUCTURES AS MAGNETIC ELEMENTS
FOR USE IN POWER PROCESSING SYSTEMS

(1)

CHAPTER I

INTRODUCTION

One of the most important elements found in electronic power processing and filter circuits is the magnetic element which may be an inductor and/or a transformer. While other components in these circuits, such as semiconductor elements and capacitors, are chosen from populations of standard sizes and ratings, the magnetic element is nearly always a custom designed and constructed element. As power processing circuits and systems have become more complex, the design of the magnetic element has necessarily become a more difficult and subtle art. Few elements available to the power processing engineer can be designed so closely to the desired parameters as the magnetic element, even though there are standard size and permeability groupings available for the magnetic cores on which windings are placed. While giving the designer a greater range of choice in circuit planning, this extra degree of freedom is not without its disadvantages. The complexity of the designer's problem is only partially indicated by the multiplicity of nonlinearities in the large range of magnetic materials available. The variety of structures and shapes is extensive as well, with shapes ranging from presized toroidal cores with known effective permeabilities to cut and pot cores for which the designer must determine the

air gap and, therefore the effective permeability. In every case, the primary goal of the designer is to determine the proper number of turns and wire size required, given that a particular magnetic structure has been selected, so that some set of design parameters will be achieved. While the design parameters frequently are a specified inductance value for a given dc current, there are other important criteria in power processing circuits which lead to different specified design parameters. By approaching the inductor design problem from a broader point of view, it is possible to take into account other factors of great importance in overall system design, such as size and weight.

In an inductor-capacitor (LC) filter circuit which follows a full-wave rectifier, the inductor is used to smooth the current flowing to the load and capacitor due to the rectifier and its output voltage which consists of unidirectional half sinusoids, thus producing across the load a dc output voltage with a small ac ripple superimposed. The filter can operate in one of two steady-state modes, usually referred to as the continuous-conduction and the discontinuous-conduction modes. In the continuous mode, current through the filter inductor L is always greater than zero. In the discontinuous mode, current through the inductor is equal to zero during a portion of each steady-state cycle. Various procedures have been reported in the literature for the analysis of rectifier-filter circuits; however, most of the design techniques employed today are based on procedures developed in the 1930's and 40's and are limited to considering RC filters, or LC filters restricted to the continuous-conduction mode [1-5]. Recently, an analysis of a rectifier with LC-filter circuit operating in the discontinuous mode was presented under the assumption that the value of the capacitance C was so large that the output ripple voltage was negligibly small [6].

In energy-storage dc-to-dc converter circuits, the inductor serves as a medium of exchange or transfer of energy between source and load. In the past, design procedures for the energy-storage reactor have been developed particularly with powdered permalloy and ferrite toroidal cores in mind [7-12]. These procedures make use of a collection of data for a finite population of core sizes and discrete effective permeabilities. In high-power applications, it may be advantageous to design and fabricate these inductors using air-gapped magnetic cores. The use of air-gapped cores permits the selection to be made from an innumerable population of core structure-size-permeability combinations and makes available a wider range of magnetic core sizes, particularly in the larger volume sizes.

An important characteristic of inductors for these applications is the ability to carry direct current without significant change in inductance over a specified range of circuit operating conditions. To avoid saturation of the magnetic material due to the dc component of winding current, it is necessary to introduce an air gap in the magnetic material. In the powder cores, the powdered magnetic material is insulated with a ceramic material which effectively provides a uniformly distributed air gap. In high power applications, it may be desirable to design these inductors using air-gapped magnetic-core structures. However, there are some disadvantages associated with the use of air-gapped structures. Introduction of an air gap in the magnetic circuit produces coupling to the fields due to other components as well as its own external fields. The air-gapped structures also tend to be more noisy acoustically than those without an air gap.

The purpose of this dissertation is three-fold:

- (1) to present the analysis of an LC-filter driven by a full-wave rectifier circuit which leads to a design procedure for the inductance value for the

general case in which the effective load resistance R_L and filter capacitance C are constraint parameters and in which both discontinuous- and continuous-conduction modes are considered.

- (2) to develop design procedures for air-gapped magnetic-core inductors for use in LC-filters for full-wave rectifier supplies.
- (3) to develop procedures for designing the energy-storage reactor for dc-to-dc converters using air-gapped magnetic structures.

This dissertation is based in part on material presented in a series of publications [13, 14, and 15] of which the writer is the principal author.

Chapter II presents the analysis of LC-filter circuits with zero source impedance which leads to a set of curves and approximate relationships which are useful for designing these filters. A similar approach is followed in Chapter III to generate design curves for filters with a non-zero source impedance. This impedance is always present in an actual physical system, and its inclusion in the analysis and in the design algorithm yields a more accurate and complete design.

In Chapter IV, two procedures for designing filter inductors using air-gapped cores are presented. The first procedure requires a digital computation to yield a design which is optimized in the sense of minimum core volume and minimum number of turns. The second procedure does not yield an optimized design as defined above, but the necessary computations may readily be carried out on an electronic pocket calculator. Using the results of the analysis developed in Chapter IV, and following the procedure presented by Hanna [16], special magnetic core curves are generated. Using these design curves, a new procedure for designing air-gapped inductors is presented in Chapter V.

In Chapter VI, a procedure for designing energy-storage reactors for dc-to-dc converters using air-gapped cores is presented. This procedure is

based on the design relationships developed in References [9–12] for gapless powdered permalloy and ferrite toroidal cores.

Conclusions which can be drawn from this work are presented in Chapter VII with suggestions for future research. The derivation of some of the more important analytical expressions presented in the text are outlined in the Appendices. The International System of Units (SI) is used throughout, and a glossary of symbols and their associated units is placed at the end of this dissertation.

CHAPTER II

ANALYSIS AND DESIGN OF FULL-WAVE RECTIFIER LC FILTERS WITH CONTINUOUS OR DISCONTINUOUS INDUCTOR CURRENT

2.1 Introduction

Conversion of ac sinusoidal voltage to dc voltage for power applications by rectification often is accomplished using the familiar center-tapped transformer rectifier or the full-wave bridge rectifier followed by an inductor-input low-pass LC filter which supplies the load R_L as shown in Figure 2.1. The sinusoidal source voltage is converted to a train of unidirectional half-sinusoids by the rectifier and is then smoothed by the LC-filter, producing across the load R_L a dc output voltage with a small ac ripple superimposed. The design of the filter for a full-wave rectifier power supply involves the determination of values for the inductor L and the capacitor C , the selection of suitable diodes, and the sizing of the transformer windings to meet the various application requirements. The requirements often include accommodation of the network to conditions of varying input source voltage and output load. Possible design specifications include the dc output voltage level, maximum allowable peak-to-peak output ripple voltage as a percentage of the dc output voltage, maximum allowable peak or rms currents in the diodes and transformer

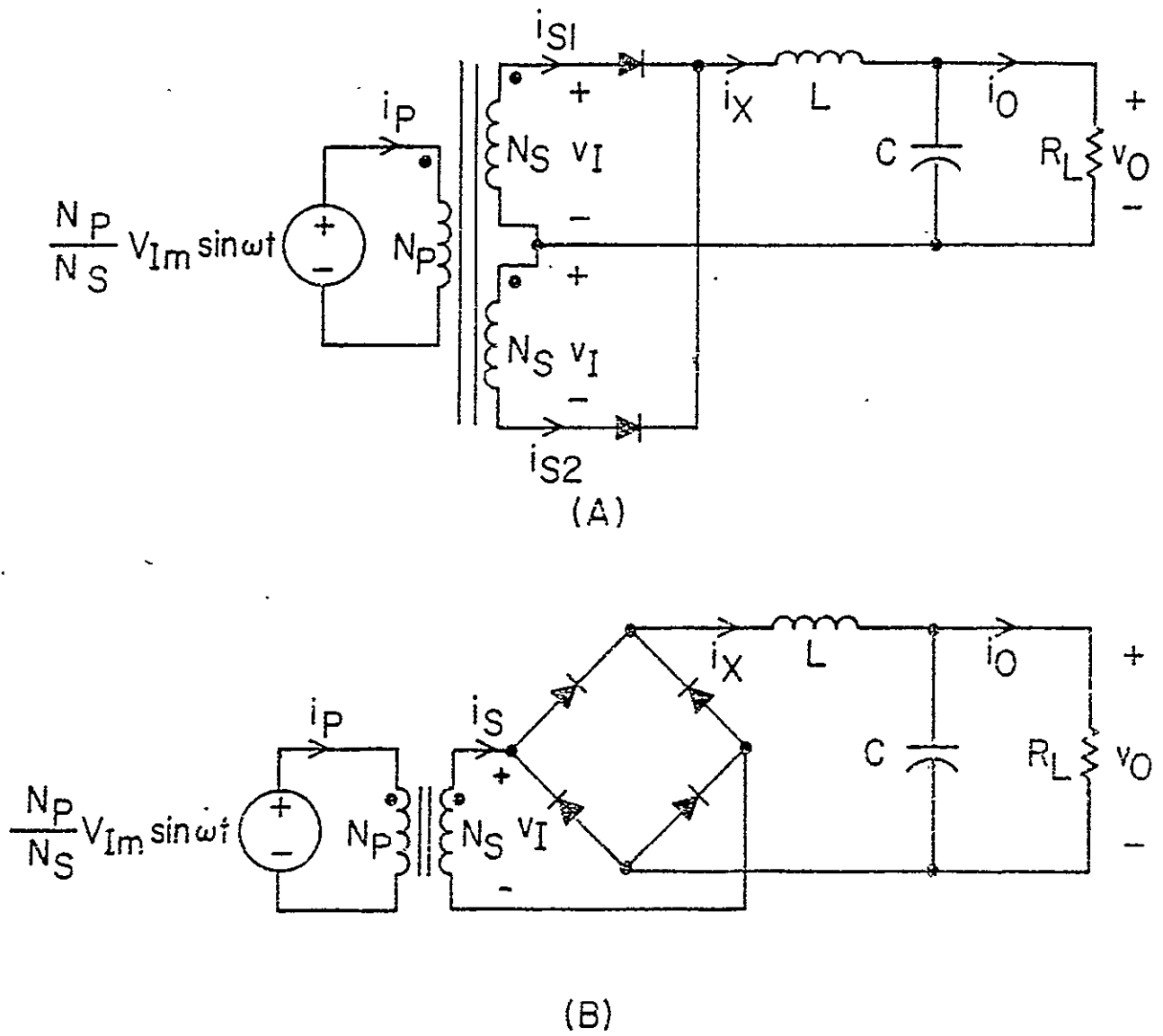


Figure 2.1. LC-filter Circuit Supplied by (A) Center-Tapped Transformer Rectifier and (B) Full-Wave Bridge Rectifier.

windings, and minimum permissible power factor at the input terminals to the network.

This chapter presents an analysis and a design procedure for the LC-filter circuit operating either in the continuous and/or in the discontinuous mode. In this chapter it is assumed in the analysis that the impedance of the sinusoidal source is negligibly small and is not included in the development of design and performance relationships. However, an analysis of the LC-filter circuit with non-zero sinusoidal source impedance is presented in the next chapter.

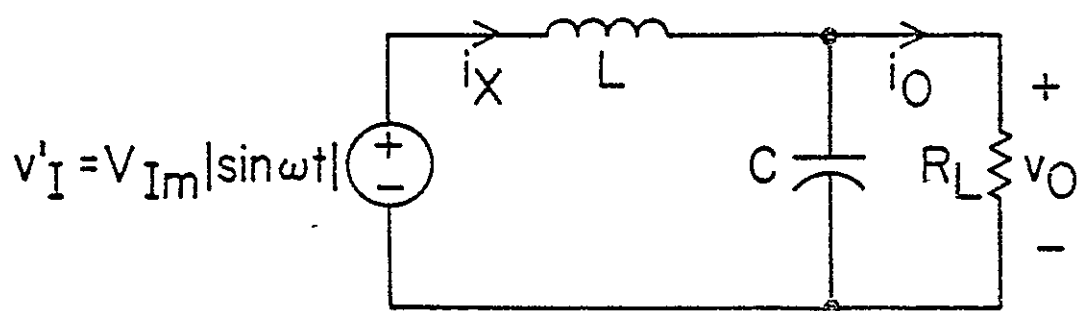
A critical condition is established as the boundary between the two modes of operation. For each value of the dimensionless angular frequency parameter ω_N , defined as ω/ω_0 , where ω is the angular frequency of the sinusoidal input voltage source in radians per second and $\omega_0 = 1/\sqrt{LC}$ is the undamped natural frequency of the low-pass filter, there exists another dimensionless parameter κ , defined as $\omega L/R_L$, for which a critical value κ_{cr} exists. For $\kappa > \kappa_{cr}$, the filter operates in the continuous-conduction mode; for $\kappa \leq \kappa_{cr}$, it operates in the discontinuous mode. For values of $\kappa > \kappa_{cr}$, the filter circuit is analyzed using Fourier series and linear circuit analysis techniques. For values of $\kappa \leq \kappa_{cr}$, the filter circuit, described analytically by piecewise-linear differential equations, is analyzed with the help of the digital computer. An algorithm for rapid determination of the periodic steady-state conditions is used to reduce the computation time for calculations involving the discontinuous mode of operation. From the analyses, a set of curves useful for design purposes is generated. The derivations of useful expressions are presented in Appendices A and B.

2.2 Circuit Analysis

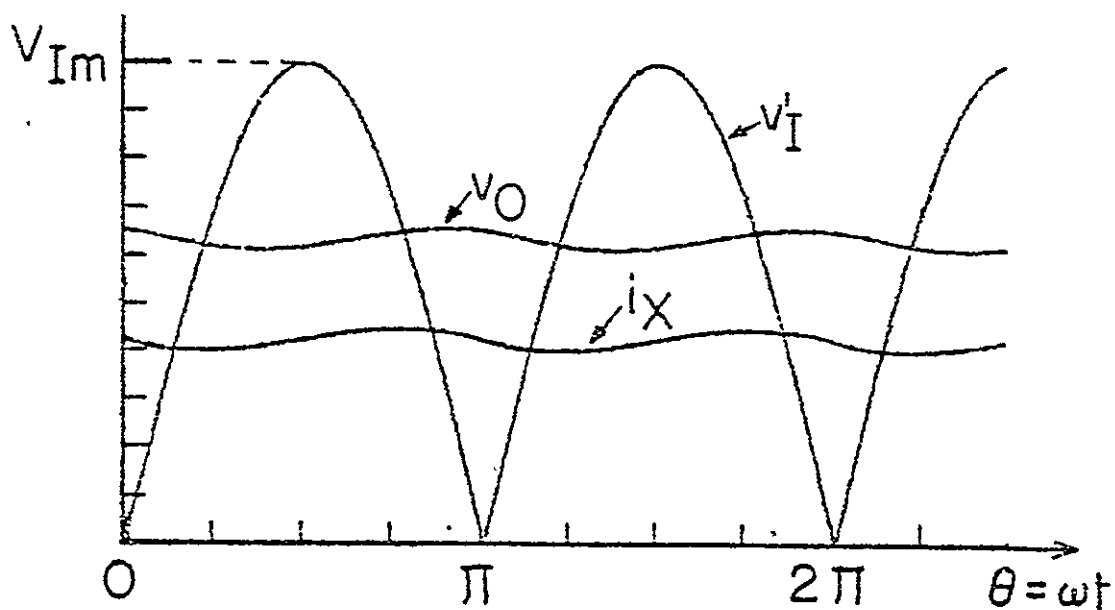
In this section, the rectifier-filter circuit is analyzed to obtain relationships useful for design purposes. In the continuous-conduction mode, linear circuit analysis techniques are employed, while in the case of the discontinuous mode, the method of analysis requires computer solutions of the piecewise-linear differential equations. In both cases, all of the elements of the circuit are assumed to be ideal with the equivalent load R_L as the only dissipative element.

2.2.1 Continuous-Conduction Mode

As mentioned earlier, in the continuous-conduction mode, current i_x in the filter inductor L is always greater than zero so that the source of voltage always is connected through forward conducting diodes to the filter input terminals. Assuming ideal diodes, the equivalent circuit for both of the configurations in Figure 2.1 is given in Figure 2.2 along with typical waveforms of inductor current i_x and output voltage v_o . Although the effect of diode forward voltage drop can be important in rectifier-filter circuits, particularly in those providing low output voltages, it is not included in the analysis since this factor would add an additional parameter to the family of curves presented later for design and performance evaluation. In one of the examples presented in a later section however, it is shown how diode voltage drops may be taken into account. The effectual value of the voltage source in the equivalent circuit, designated as v_I' , is the full-wave rectified value of the sinusoidal input voltage v_I . This linear equivalent circuit can be analyzed for steady-state solutions using Fourier-series techniques. The effectual source voltage v_I' is represented by its Fourier-series expansion consisting of a dc



(A)



(B)

Figure 2.2. (A) Equivalent Diagram for the Rectifier-Filter Circuits Operating in the Continuous-Conduction Mode.

(B) Associated Voltage and Current Waveforms from Computer Solutions of Circuit Equations.

component followed by a series of ac sinusoidal terms with amplitudes and frequencies given by the expression:

$$v_I' = V_{Im} |\sin \theta| = \frac{4V_{Im}}{\pi} \left(\frac{1}{2} - \frac{\cos 2\theta}{3} - \frac{\cos 4\theta}{15} - \frac{\cos 6\theta}{35} \dots - \frac{\cos 2n\theta}{4n^2-1} - \dots \right) \quad (2.1)$$

where $\theta = \omega t = 2\pi f t$, where f is the ac supply frequency, and n is a positive integer.

All current and voltage components in the circuit are computed separately by sinusoidal steady-state methods. The total current or voltage in any branch of the circuit may be found by summing the separate harmonic components from the individual terms of (2.1) using the superposition principle. Analysis of the filter circuit shows that its transfer function falls off at the rate of 40 dB per decade (12 dB per octave) as an asymptotic slope limit. In addition to the increasing attenuation of the filter with increasing frequency, the magnitudes of the sinusoidal components of the input voltage v_I' also fall off rapidly with harmonic number. Assuming that all harmonic terms, beginning with the second term in the expression for v_I' given by (2.1), lie in the range of the 40 dB per decade slope of the filter transfer function, the combination of attenuation and harmonic-term magnitudes yield values of 0.05 and 0.0053 for the ratios of the fourth-harmonic and sixth-harmonic terms of v_0 to the second harmonic term of the output voltage. Thus, the second harmonic of the input ac supply is seen to be the only component of significance in determining the output ripple voltage when the circuit is operated in the continuous-conduction mode, and the equivalent input voltage v_I' may be approximated by the expression:

$$v_I' = \frac{4V_{Im}}{\pi} \left(\frac{1}{2} - \frac{\cos 2\theta}{3} \right) \quad (2.2)$$

The transfer function of the filter circuit operating in the continuous mode is given by the following

$$\frac{v_0(s)}{v_I(s)} = \frac{1}{[s^2 LC + s(L/R_L) + 1]} \quad (2.3)$$

Using the expression in (2.2) and the transfer function of the filter given by (2.3), a number of useful relations for various voltage and current components may be derived:

DC output voltage:
$$V_0 = \frac{2V_{Im}}{\pi} \quad (2.4)$$

Peak-to-peak ripple voltage:
$$V_{Op} = \left(\frac{8V_{Im}}{3\pi} \right) / \left(\sqrt{1 - 8\omega_N^2 + 16\omega_N^4 + 4\kappa^2} \right) \quad (2.5)$$

Rms inductor current:
$$I_{Xe} = \frac{4V_{Im}}{\pi R_L} \left(\sqrt{\frac{1}{4} + \frac{1 + (4\omega_N^4/\kappa^2)}{18(1 - 8\omega_N^2 + 16\omega_N^4 + 4\kappa^2)}} \right) \quad (2.6)$$

Peak inductor current:
$$I_{Xm} = \frac{4V_{Im}}{\pi R_L} \left(\frac{1}{2} + \frac{1}{3} \sqrt{\frac{1 + (4\omega_N^4/\kappa^2)}{1 - 8\omega_N^2 + 16\omega_N^4 + 4\kappa^2}} \right) \quad (2.7)$$

2.2.2 Discontinuous-Conduction Mode

In the discontinuous mode the action of the diodes is such that the current i_x is equal to zero during a portion of each steady-state cycle. The equivalent circuit when diodes are conducting is the same as for the continuous mode and is shown in Figure 2.3(A) where the second subscript 1 is added to signify the voltages and currents associated with this portion of the cycle. The output voltage v_{01} is obtained from solution of the following equation:

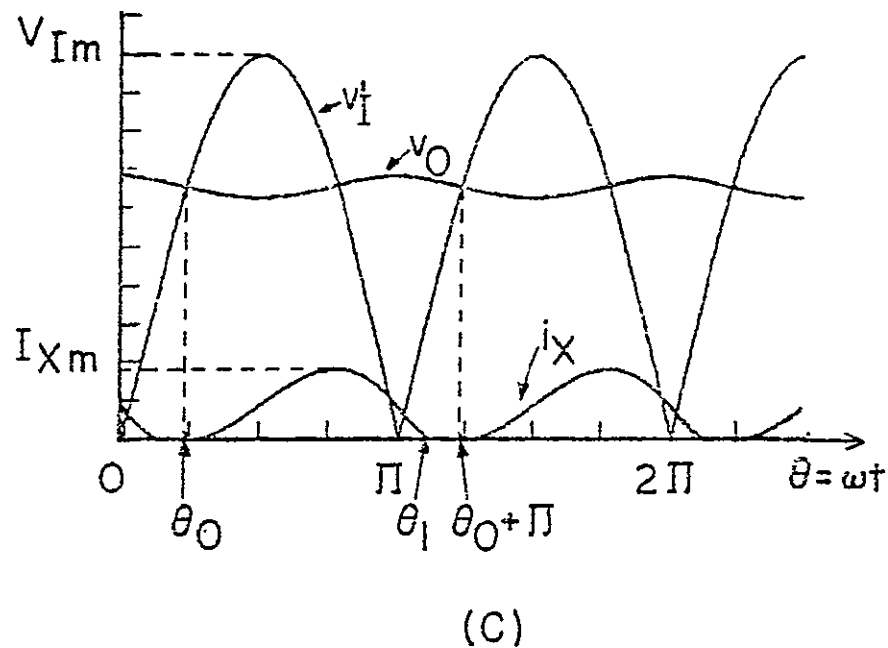
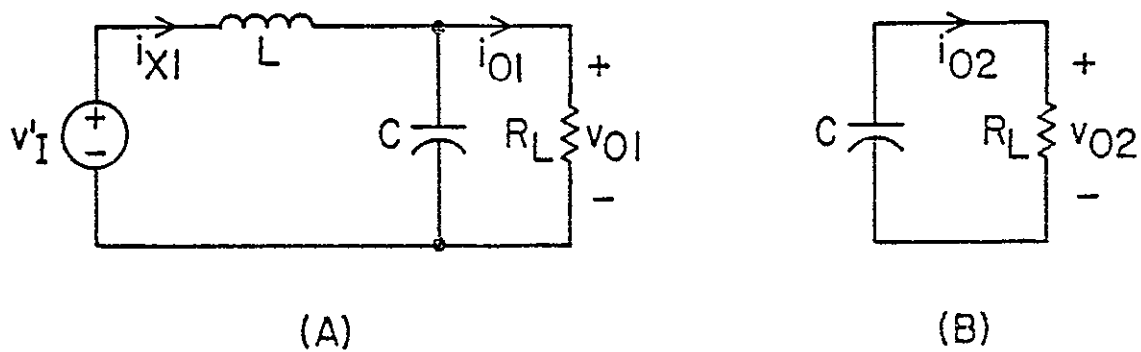


Figure 2.3. Equivalent Diagrams for the Rectifier-Filter Circuits Operating in the Discontinuous-Conduction Mode During Interval (A) When Diodes are Conducting and (B) When Diodes are not Conducting. (C) Associated Voltage and Current Waveforms from Computer Solutions of Circuit Equations.

$$\omega_N^2 \frac{d^2 v_{01}}{d\theta^2} + \kappa \frac{dv_{01}}{d\theta} + v_{01} = V_{Im} |\sin(\theta - \theta_0)| \quad (2.8)$$

The value of inductor current i_{X1} is given by

$$i_{X1} = \omega C \frac{dv_{01}}{d\theta} + \frac{v_{01}}{R_L} \quad (2.9)$$

The range of applicability of θ is from θ_0 to θ_1 , corresponding to the beginning and the end of the conduction interval, so that

$$i_{X1}(\theta_0) = i_{X1}(\theta_1) = 0 \quad (2.10)$$

The solutions to (2.8) and (2.9), subject to the constraints given by (2.10), yield the following expressions for v_{01} and i_{X1} :

$$v_{01}(\theta) = A_V \sin\theta + B_V \cos\theta + \exp(\beta\theta) [C_V \sin(\alpha\theta) + D_V \cos(\alpha\theta)] \quad (2.11)$$

$$i_{X1}(\theta) = \frac{1}{R_L} \{A_i \sin\theta + B_i \cos\theta + \exp(\beta\theta) [C_i \sin(\alpha\theta) + D_i \cos(\alpha\theta)]\} \quad (2.12)$$

for $\theta_0 \leq \theta \leq \theta_1$. The values for the various coefficients depend on κ , ω_N , and θ_0 , and expressions for them are given in the glossary of symbols.

When the diodes are not conducting, the equivalent circuit is that shown in Figure 2.3(B), where the second subscript 2 denotes this operating condition. The output voltage v_{02} and current i_{X2} for this part of the cycle are described by the following equations:

$$\omega C \frac{dv_{02}}{d\theta} + \frac{v_{02}}{R_L} = 0 \quad (2.13)$$

$$i_{X2}(\theta) = 0 \quad (2.14)$$

where the range of θ is from θ_1 to $(\theta_0 + \pi)$, corresponding to the interval during which the inductor current is zero. Solving (2.13) yields the expression:

$$v_{02}(\theta) = v_{02}(\theta_1) \exp[-(\theta - \theta_1)/\omega CR_L] \quad (2.15)$$

From the requirements for a steady state in the discontinuous mode, and from the requirement of continuity of the output voltage across capacitor C, the following conditions must be satisfied:

$$v_{02}(\theta_0 + \pi) = v_{01}(\theta_0) \quad (2.16)$$

$$v_{02}(\theta_1) = v_{01}(\theta_1) \quad (2.17)$$

$$i_{x1}(\theta_0) = i_{x1}(\theta_1) = 0 \quad (2.18)$$

In order to obtain the steady-state solutions for v_0 and i_x the two transcendental equations given by (2.11) and (2.15) must be solved simultaneously subject to the conditions imposed by (2.16), (2.17), and (2.18). The implicit relationships in this type of simultaneous equation pair suggest that digital computation be employed to obtain numerical answers for the solutions. An algorithm, described in the section which follows, was devised to rapidly determine the steady-state voltages and currents.

2.2.3 Algorithm to Determine Steady-State Values of v_0 and i_x

A simple algorithm for quickly determining the periodic steady-state is illustrated in the flow chart in Figure 2.4. Two first-trial initial values of output voltage $v_0^{(1)}$ and $v_0^{(2)}$ are entered as starting values and the corresponding initial trial values of θ_0 , $\theta_0^{(1)}$ and $\theta_0^{(2)}$, are calculated using the relationship

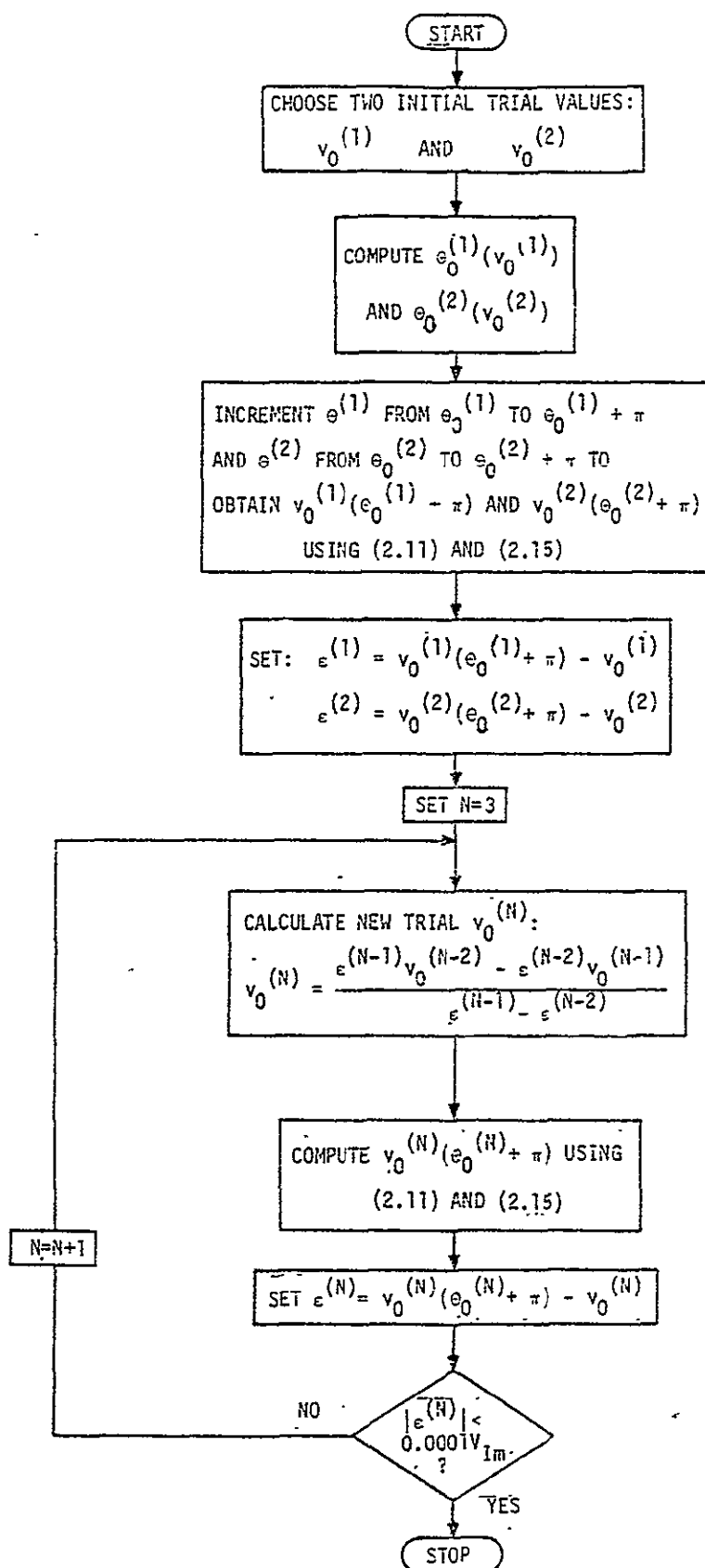


Figure 2.4 Flow-Chart of algorithm for rapid determination of the periodic steady-state of the rectifier-filter circuit operating in the discontinuous-conduction mode.

$$\theta_0^{(N)} = \arcsin (v_0^{(N)}/V_{Im})$$

The values of $\theta^{(1)}$ and $\theta^{(2)}$ are then incremented by a prescribed small amount from the starting values of $\theta_0^{(1)}$ and $\theta_0^{(2)}$, respectively, and the corresponding values $v_0^{(1)}(\theta)$ and $v_0^{(2)}(\theta)$ and $i_{x1}^{(1)}(\theta)$ and $i_{x2}^{(2)}(\theta)$ are computed using (2.11) and (2.12). If the values of $i_x^{(1)}$ or $i_x^{(2)}$ are computed to be equal to or less than zero, the values of $\theta^{(1)}$ and $\theta^{(2)}$ are identified tentatively as $\theta_1^{(1)}$ and $\theta_1^{(2)}$, which mark the end of the inductor conduction interval. As $\theta^{(1)}$ and $\theta^{(2)}$ are incremented over the interval from $\theta_1^{(1)}$ to $\theta_0^{(1)} + \pi$ and $\theta_1^{(2)}$ to $\theta_0^{(2)} + \pi$, respectively, $v_0^{(1)}$ and $v_0^{(2)}$ are computed using (2.15). The inductor currents, $i_x^{(1)}$ and $i_x^{(2)}$ remain zero during this interval. The error $\epsilon^{(1)}$ is computed as the difference between the computed value of $v_0^{(1)}$ at $\theta^{(1)} = \theta_0^{(1)} + \pi$ and the initial guess for $v_0^{(1)}$ at $\theta^{(1)} = \theta_0^{(1)}$. Similarly, the error $\epsilon^{(2)}$ is computed for the second trial. Using $\epsilon^{(1)}$ and $\epsilon^{(2)}$, and initial values $v_0^{(1)}$ and $v_0^{(2)}$, a new trial value for $v_0^{(3)}$ at $\theta^{(3)} = \theta_0^{(3)}$ is computed by linear interpolation or extrapolation as shown in flow chart. The above process is repeated until the solution for $v_0(\theta_0)$ converges, thus yielding the values of θ_0 and θ_1 . Results obtained from a number of computer runs show that usually only three or four iterations are required to obtain solutions which converge to within a prescribed error bound of $0.0001V_{Im}$. By incorporating this algorithm in the computer program, considerable reduction in the computation time involved in the steady-state analysis of rectifier-filter circuits when they are operated in the discontinuous-conduction modes, is obtained.

With these data the steady-state time waveforms of v_0 and i_X can be calculated. The peak-to-peak output ripple voltage and the peak inductor current are recorded, and computer calculations are made for the average output voltage and the rms inductor current. Computer calculations are also made for the input power factor of the transformer-filter circuit.

In the next section, an expression for the critical condition is derived.

2.2.4 Critical Condition

As mentioned in an earlier section, the critical condition establishes the boundary between the two modes of operation. Using (2.2), the inductor current i_X in the continuous mode is given by the expression:

$$i_X = \frac{4V_{Im}}{\pi} \left[\frac{1}{2R_L} - \frac{\cos(2\theta - \psi)}{3|Z(j2\omega)|} \right] \quad (2.19)$$

where $|Z(j2\omega)|$ and ψ are the magnitude and phase of the filter impedance seen from the source v_1 at the second harmonic of the sinusoidal ac supply voltage and are defined in terms of κ , R_L , and ω_N as follows:

$$|Z(j2\omega)| = R_L \sqrt{\frac{1 - 8\omega_N^2 + 16\omega_N^4 + 4\kappa^2}{1 + (4\omega_N^4/\kappa^2)}} \quad (2.20)$$

$$\psi = \arctan[2\kappa/(1 - 4\omega_N^2)] - \arctan[2\omega_N^2/\kappa] \quad (2.21)$$

From (2.19), the minimum instantaneous value of i_X occurs when the cosine term has a value of unity. For the critical-condition boundary between the continuous- and discontinuous-conduction modes of operation, the

minimum value of i_x just reaches zero or

$$\frac{4V_{Im}}{\pi} \left(\frac{1}{2R_L} - \frac{1}{3|Z(j2\omega)|} \right) = 0 \quad (2.22)$$

Rearranging (2.22) and substituting for $|Z(j2\omega)|$ from (2.20) leads to the relationship:

$$\sqrt{\frac{1 - 8\omega_N^2 + 16\omega_N^4 + 4\kappa^2}{1 + (4\omega_N^4/\kappa^2)}} = \frac{2}{3} \quad (2.23)$$

Squaring (2.23) and simplifying yields the expression:

$$F(\kappa, \omega_N) = 0 = \kappa^4 + \kappa^2 \left(\frac{5}{36} - 2\omega_N^2 + 4\omega_N^4 \right) - \frac{4\omega_N^4}{9} \quad (2.24)$$

For a given value of ω_N , the value of κ satisfying the critical condition $F(\kappa, \omega_N) = 0$, referred to as κ_{cr} , can be found. Since both κ and ω_N have a physical interpretation only for positive values, for a given value of ω_N , κ_{cr} is single valued. A plot of κ_{cr} for various values of ω_N is shown in Figure 2.5. The abscissa, $\omega_N = \omega\sqrt{LC}$, depends only on filter parameters and the frequency of the sinusoidal ac supply voltage. The value of κ , previously defined as $\omega L/R_L$, additionally depends on the filter load resistance R_L . For heavy loads, i.e., R_L small, the value of κ is greater than κ_{cr} , causing the filter circuit to operate in the continuous mode and the circuit is analyzed using Fourier-series techniques. For light loads, the value of κ is less than κ_{cr} , the rectifier-filter circuit operates in the discontinuous mode, and the filter behavior is analyzed using piecewise-linear differential equations. The value of κ_{cr} is approximately equal to its asymptotic value of $1/3$ for values of ω_N greater than 5.0. The critical

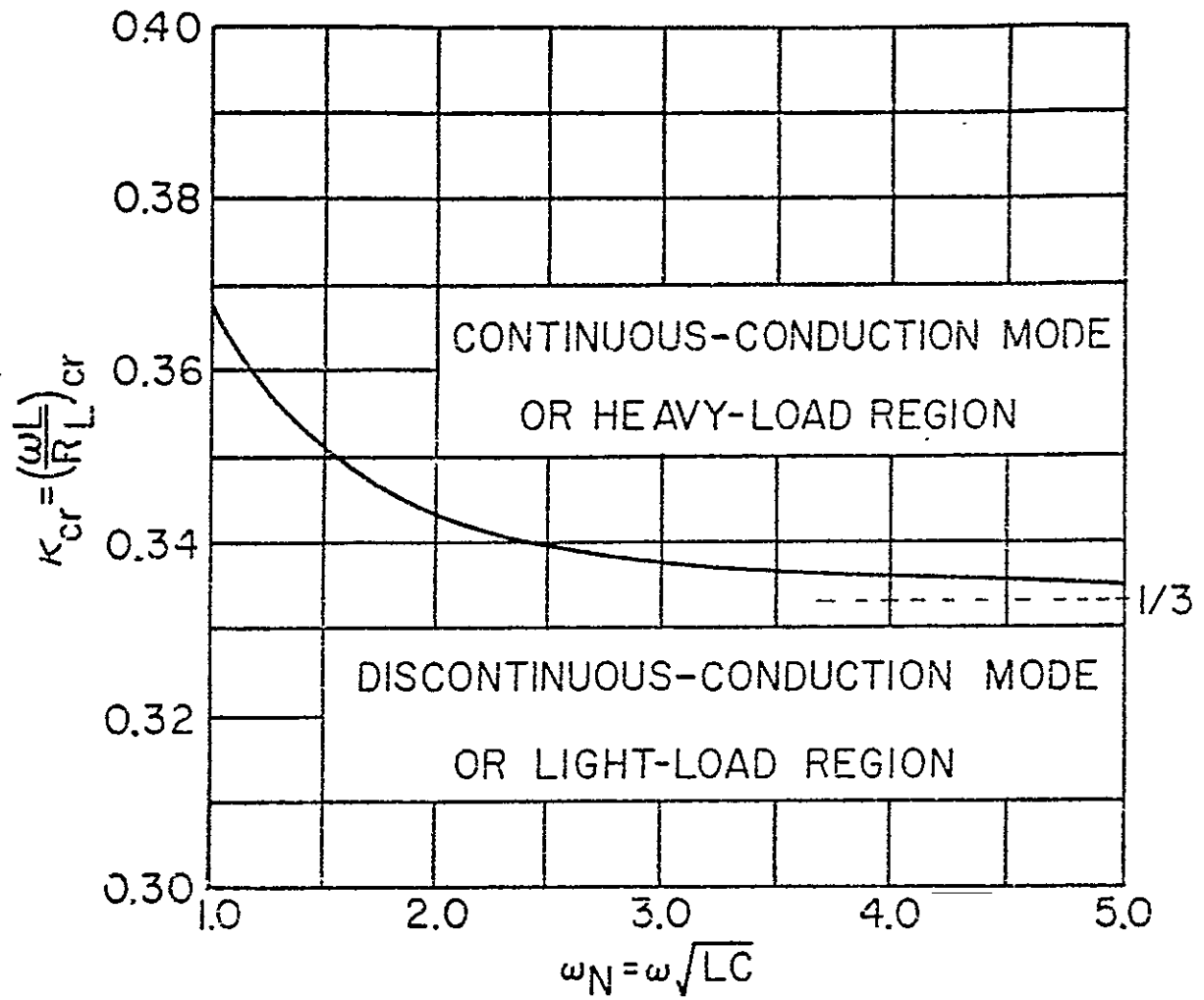


Figure 2.5. Plot of κ_{cr} Versus ω_N and Identification Regions.

condition and the circuit-analysis methods for continuous and discontinuous modes which have been described are used in a later section for generating design curves.

2.2.5 Relationship Between κ , ω_N , Q , ξ , and ω

The transfer function of the filter circuit operating in the continuous mode, shown in Figure 2.2, is given by (2.3) and may be written in the familiar form $V_0(s)/V_I(s) = 1/[(s/\omega_0)^2 + (1/Q)(s/\omega_0) + 1]$ where s is the complex frequency variable, $\omega_0 = 1/\sqrt{LC}$ is the familiar undamped resonant frequency of oscillation in radians per second, and $Q = R_L/\omega_0 L$ is the quality factor at the resonant frequency. The damping factor ξ is related to Q by $\xi = 1/2Q$. From the previously given definition of ω_N , the damping factor can be expressed as

$$\xi = \kappa/2\omega_N \quad (2.25)$$

The quality factor Q is related to κ and ω_N by the expression:

$$Q = \omega_N/\kappa \quad (2.26)$$

The relationships shown in (2.25) and (2.26) should be helpful in identifying and attaching extended meanings to the design parameters κ and ω_N .

2.2.6 Power Factor

The input power factor for a nonlinear ac load such as either of the transformer-filter circuits of Figure 2.1 is defined by Schwarz [6], and by Kornrumpf and Walden [17] as the ratio of the power dissipated in the network to the product of the rms values of the ac input voltage and the ac input

current. Because of symmetry considerations and because the rectifiers and filter elements have been assumed lossless, the product of the ac input rms values $(N_p/N_s)V_{Ie}I_{Pe}$ equals the product of the rms values at the input to the LC filter $V_{Ie}I_{Xe}$. Also, the output power to the load calculated as V_{Oe}^2/R_L is equal to the input power. Thus, the expression

$$\text{Power Factor} = \frac{V_{Oe}^2/R_L}{V_{Ie} I_{Xe}} \quad (2.27)$$

has been used in calculating this performance measure of the network.

2.3 Design and Performance Curves and Approximate Relationships

2.3.1 Design and Performance Curves

Using the methods of analysis described in the previous sections, a set of curves useful for both designing and analyzing rectifier LC-filter circuits was generated by digital computation and is shown in Figure 2.6.

In the upper curves, the ratio of peak-to-peak output ripple voltage V_{Op} to dc output voltage V_O is plotted against κ for values of ω_N lying between 2.0 and 10.0. The dashed line in this plot represents the critical condition obtained from a solution of (2.24) and separates the plot into regions of continuous conduction and discontinuous conduction. In the second graph, two families of plots are presented for the same range of values for ω_N and κ . They show the ratio of the dc output voltage V_O to the peak value of input source V_{Im} and the power factor P.F. of the ac input to the rectifier-filter combination. These curves, V_O/V_{Im} and P.F. versus κ , actually consist of multiple plots of curves for the same values of ω_N as used in the top graph but appear to approach two single curves because of their weak dependency upon ω_N . As seen from the V_O/V_{Im} curve, for rectifier-filter circuits operating in the discontinuous-conduction mode, a larger dc output volt-

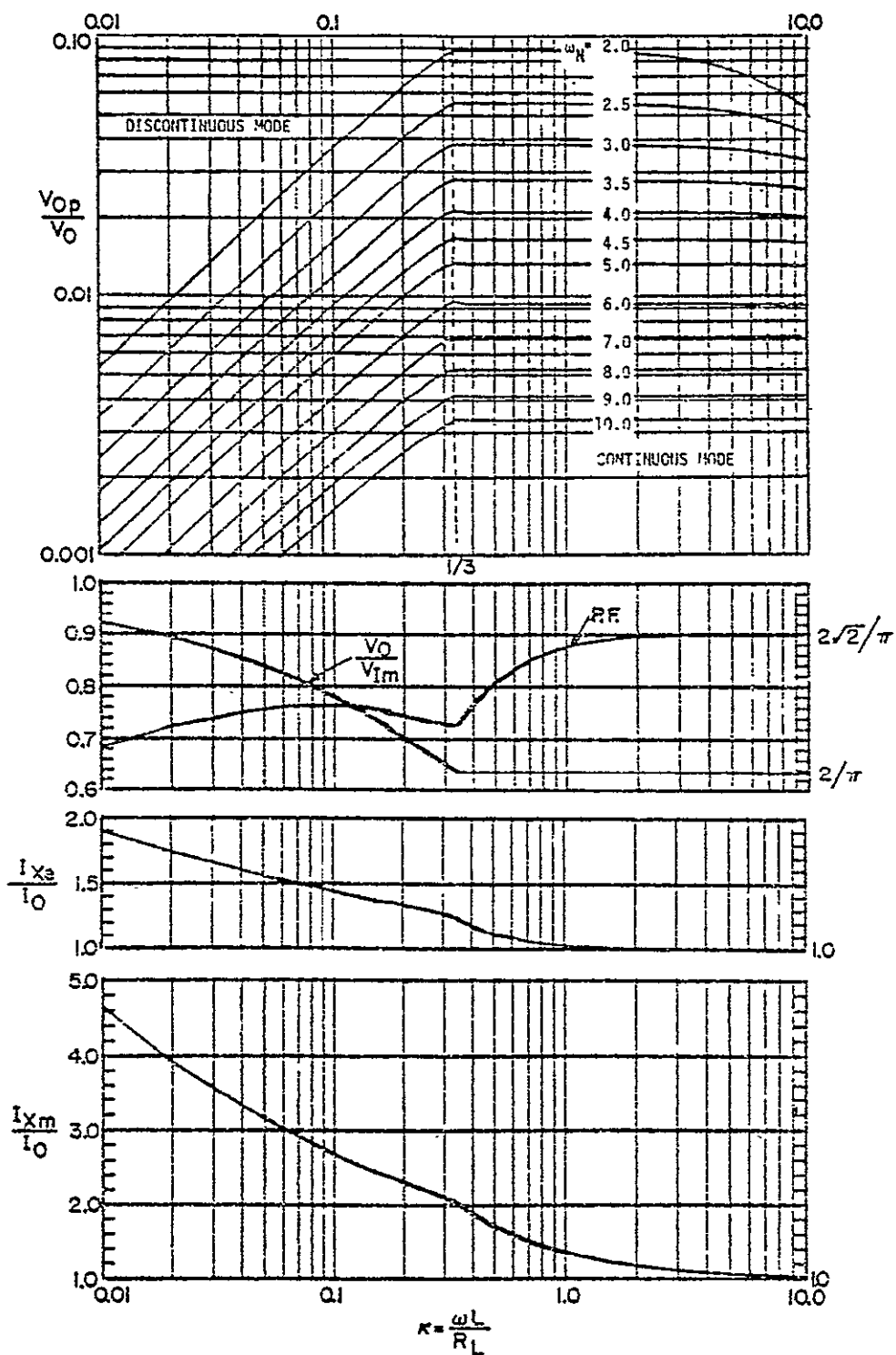


Figure 2.6. Design and performance curves for LC-filters operating both in the continuous- and discontinuous-conduction modes.

age is obtained than that in the continuous-conduction mode for a given value of input supply voltage V_{Im} . Other useful design curves, the ratio of the rms value of current in the inductor I_{Xe} to the average dc load current I_0 , and the ratio of the peak value of inductor current I_{Xm} to I_0 are plotted as the third and fourth graphs of the same figure. Again, although appearing as single isolated curves these are actually the result of superimposed multiple plots over the range of ω_N previously stated.

Additional use may be made of the graphs in Figure 2.6 to calculate the values of the rms currents in the transformer windings. In terms of the rms inductor current I_{Xe} , useful relationships are:

$$\text{Center-tapped secondary:} \quad I_{Se} = I_{Xe}/\sqrt{2} \quad (2.28)$$

$$\text{Single-winding secondary:} \quad I_{Se} = I_{Xe} \quad (2.29)$$

$$\text{Either configuration:} \quad I_{Pe} = (N_S/N_P) I_{Xe} \quad (2.30)$$

A study of the V_{Op}/V_0 curves at the top of Figure 2.6 shows that various combinations of κ and ω_N may be chosen to meet a specified (V_{Op}/V_0) ripple requirement. Consequently, an additional specification must be provided to complete the information required for the design procedure. While the additional constraint which usually is imposed is the desired output voltage, the peak or the rms value of the current in an individual diode, the maximum allowable current in the transformer windings, or the minimum desired power factor, may be used. Having chosen the additional constraint, the design process can continue, leading to values for the remaining unconstrained rectifier-filter parameters which can be determined from the other plots in Figure 2.6. To illustrate the design procedure, several examples are worked out in section 2.4.

2.3.2 Approximate Analytical Design Relationships

The design curves for various performance parameters, shown in Figure 2.6, can be approximated by analytical design relationships given in Table 2.1. The values for the performance parameters computed from these approximate design relationships are reasonably close to the computed values or those read from the design curves. The approximate design relationships can be automated on a digital computer or electronic pocket calculator to yield quickly designs for LC-filters. These relationships, therefore, provide an alternate method to the reading of data from the design curves. In Table 2.1, the analytical expressions are given for design relationships $V_{Op}/V_0(\kappa, \omega_N)$, $V_0/V_{Im}(\kappa)$, $I_{Xe}/I_0(\kappa)$, $I_{Xm}/I_0(\kappa)$, and $P.F.(\kappa)$. For the continuous mode, these approximate design relationships are obtained from the exact relationships given in Appendix A under the assumption that $4\omega_N^2$ is much larger than 1 and κ .

For the discontinuous mode, a good approximation to the (V_{Op}/V_0) curve shapes in Figure 2.6 is obtained if they are considered to be straight lines parallel to each other and starting at the continuous mode point for $\kappa = 1/3$. One such approximation for (V_{Op}/V_0) for the discontinuous mode is shown in Table 2.1, and values computed from this approximate relationship lie within ten percent of the values read from the curves. As mentioned earlier, the other performance parameters, V_0/V_{Im} , I_{Xe}/I_0 , I_{Xm}/I_0 , and $P.F.$ are weakly dependent on ω_N and hence are approximated by polynomials of second degree passing through the points on the curves for these latter parameters and are functions of κ only. The values computed for these latter parameters from the approximations given in Table 2.1 lie within five percent of values read from the curves. In addition to the design relationships for the performance parameters, expressions for inverse relationships $\omega_N(V_{Op}/V_0, \kappa)$, $\kappa(V_{Op}/V_0, \omega_N)$,

Table 2.1. Approximate design and performance relationships for LC-filter operating both in the continuous- and discontinuous-conduction modes.

	$\kappa \leq 1/3$ DISCONTINUOUS MODE	$\kappa \geq 1/3$ CONTINUOUS MODE
$\frac{V_{00}}{V_0}(\kappa, \omega_N)$	$(0.766 \kappa^{0.758})/\omega_N^2$	$\frac{2}{3\sqrt{\kappa^2 - 2\omega_N^2 + 4\omega_N^4}}$
$\frac{V_0}{V_{Im}}(\kappa)$	$0.466 - 0.398 \log \kappa - 0.086 (\log \kappa)^2$	$\frac{2}{\pi}$
$\frac{I_{Xe}}{I_0}(\kappa)$	$1.0552 - 0.334 \log \kappa + 0.044 (\log \kappa)^2$	$\sqrt{1 + \frac{1}{18\kappa^2}}$
$\frac{I_{Xm}}{I_0}(\kappa)$	$1.642 - 0.518 \log \kappa + 0.485 (\log \kappa)^2$	$1 + \frac{1}{3\kappa}$
P.F. (κ)	$0.713 - 0.111 \log \kappa - 0.064 (\log \kappa)^2$	$\frac{2\sqrt{2}}{\pi\sqrt{1 + 1/(18\kappa^2)}}$
$\omega_N(V_{0p}/V_0, \kappa)$	$\sqrt{\frac{0.766\kappa^{0.758}}{(V_{0p}/V_0)}}$	$\frac{1}{2}\sqrt{2\sqrt{\left\{\frac{4}{9(V_{0p}/V_0)^2} - \kappa^2\right\}} + 1}$
$\kappa(V_{0p}/V_0, \omega_N)$	$10^{\left(\frac{\log[\omega_N^2(V_{0p}/V_0)/0.766]}{0.758}\right)}$	$2\sqrt{\frac{4}{9(V_{0p}/V_0)^2} + 2\omega_N^2 - 4\omega_N^4}$
$\kappa(V_0/V_{Im})$	$10^{\left(\frac{[0.398 - \sqrt{0.158 - 0.343((V_0/V_{Im}) - 0.466)^2}]}{0.117}\right)}$	Independent of V_0/V_{Im}
$\kappa(I_{Xe}/I_0)$	$10^{\left(\frac{[0.334 - \sqrt{0.112 + 0.176((I_{Xe}/I_0) - 1.055)^2}]}{0.088}\right)}$	$\frac{1}{3\sqrt{2}\sqrt{(I_{Xe}/I_0)^2 - 1}}$
$\kappa(I_{Xm}/I_0)$	$10^{\left(\frac{[0.518 - \sqrt{0.268 + 1.94((I_{Xm}/I_0) - 1.642)^2}]}{0.971}\right)}$	$\frac{1}{3[I_{Xm}/I_0 - 1]}$
$\kappa(P.F.)$	$10^{\left(\frac{[0.11 - \sqrt{0.012 - 0.38((P.F.) - 0.713)^2}]}{0.127}\right)}$	$\frac{1}{3\sqrt{2}\left[18/(\pi^2(P.F.)^2) - 1\right]}$

$\kappa(V_0/V_{Im})$, $\kappa(I_{Xe}/I_0)$, $\kappa(I_{Xm}/I_0)$, and $\kappa(P.F.)$ are also given. In the continuous mode, V_0/V_{Im} is independent of κ and hence there is no inverse relationship $\kappa(V_0/V_{Im})$ for the continuous mode in Table 2.1.

These approximate design relationships should be used carefully depending on the desired accuracy of the design.

2.4 Design Examples

To illustrate the usefulness of the curves presented in the preceding section, examples of two different filter designs now are discussed. These examples illustrate how two rather different application requirements can be satisfied. The International System (SI) of Units is used in the examples.

Example 1.

The values of the inductor and capacitor elements in an LC-filter circuit with nominal output voltage $V_0 = 5\text{ V}$, nominal load current $I_0 = 10\text{ A}$, and ripple ratio $V_{Op}/V_0 = 0.05$ are to be found. The supply voltage to the rectifiers is provided by the secondary windings of a center-tapped transformer, the primary of which is excited by an ac supply of 117 v rms at 60 Hz. The inductor-capacitor filter circuit is to operate in the continuous-conduction mode.

Given that the ripple ratio $V_{Op}/V_0 = 0.05$ and that the filter is in the continuous-conduction mode, the design procedure begins with the V_{Op}/V_0 curves in Figure 2.6. Choosing the curve for $\omega_N = 2.5$ as an example, the ripple constraint under nominal load is met with a value of $\kappa = 6.0$. Using the equivalent load resistance R_L corresponding to nominal output voltage and load current, $R_L = 0.5\text{ ohm}$, the values of L and C may be obtained using the relationships $\kappa = \omega L/R_L$ and $\omega_N = \omega\sqrt{LC}$, to yield $L = 7.96\text{ mH}$ and $C = 5526\text{ }\mu\text{F}$.

Having established values for ω_N , κ , L and C , the performance of the filter network and the determination of important parameters useful in completing the design of the remainder of the complete power supply may be obtained. For example, if the filter circuit always is to operate in the continuous-conduction mode, the minimum value of κ is approximately 1/3 corresponding to a load resistance 18 times the nominal load resistance. Since V_0/V_{Im} is very nearly constant over this range, the minimum load current before the output voltage begins to rise is ($I_{0,nominal}/18$) or 0.56A. If the maximum load current is, for example, 1.5 times the nominal I_0 value of 10 A, the corresponding maximum value κ reaches is 6.0 ($15/10$) = 9.0.

Using $\omega_N = 2.5$ and the range of κ from 1/3 to 9.0, the performance of the filter circuit is obtained from the various curves in Figure 2.6 as follows:

Ratio	Load Condition		
	Minimum	Nominal	Maximum
$\kappa = \omega L/R_L$	1/3	6.0	9.0
Average output voltage, V_0	5.02 V	5.02 V	5.02 V
Peak-to-peak ripple voltage to output voltage, V_{0p}/V_0	0.055	0.05	0.043
Output voltage to peak input voltage, V_0/V_{Im}	0.64	0.64	0.64
Average load current, I_0	0.56 A	10.0 A	15.0 A
Peak reactor current to load current, I_{Xm}/I_0	2.0	1.03	1.0
Rms reactor current to load current, I_{Xe}/I_0	1.2	1.0	1.0
Rms transformer secondary current to load current, I_{Se}/I_0	0.85	0.71	0.71
Power factor of filter circuit	0.73	0.90	0.90

Of particular interest is the performance curve for the ratio of output voltage to peak input voltage V_0/V_{Im} which approaches the asymptotic value $2/\pi \approx 0.64$ for values of κ greater than κ_{cr} .

From the knowledge of the ratio V_0/V_{Im} , I_{Xe}/I_0 and I_{Xm}/I_0 , it is now possible to determine the characteristics required of the center-tapped transformer and the diodes in the power supply circuit. Using the nominal load voltage and current values for this example, it is noted that the diode forward voltage drop V_{diode} (approximately 0.7 for silicon diodes) is a significant fraction of the output voltage V_0 . Recognizing that in the continuous-conduction mode the average output voltage must be the average input voltage to the rectifier-filter less the constant diode drop, the required peak voltage on the transformer secondaries must be $V_{Im} \approx [V_0 + V_{diode}]\pi/2$. For this example, $V_{Im} = 8.95$ V. Using the specified primary supply voltage, the turns ratio N_S/N_P is computed to be 1/18.5.

Using the nominal value of I_0 as the maximum value for sustained operation, the peak reactor current I_{Xm} is approximately 10.3 A, while the rms reactor current $I_{Xe} = 10.0$ A. The rms secondary winding current I_{Se} in a center-tapped secondary is equal to the rms reactor current I_{Xe} divided by $\sqrt{2}$ and has a value of 7.07 A. The rms primary winding current, neglecting magnetizing current and using a turns ratio of 1/18.5, is 0.54 A. The power factor P.F. is approximately 0.9, approaching closely the asymptotic value $2\sqrt{2}/\pi$. The diodes because of their shorter thermal time constant should be selected on the basis of the peak current to be encountered 10.3 A.

Example 2.

In this example, an LC filter circuit driven by a full-wave bridge rectifier connected directly to the ac supply is to operate in the discontinuous-conduction mode. The specifications are: nominal output voltage $V_0 = 115$ V, nominal load current $I_0 = 5$ A, with a ripple ratio $V_{op}/V_0 = 0.02$. The ac supply voltage is 117 V rms, 400 Hz.

Under nominal output voltage and load conditions, the ratio $V_0/V_{Im} = 0.695$ and from the curve for this parameter in Figure 2.6, $\kappa = 0.2$. To meet the ripple requirement $V_{op}/V_0 = 0.02$, the curve corresponding to $\omega_N = 3.5$ is selected. Using the value of $R_L = 23$ ohms for the nominal load, the values of the filter components are computed to be: $L = 1.83$ mH; $C = 1060$ μ F.

If the filter circuit is to operate in the discontinuous-conduction mode for all loads within the range of the curves in Figure 2.6, κ can vary from 0.01 to 1/3. Examining the characteristics of the combined transformer-rectifier-filter circuit over this range in κ yields the following results:

Ratio	Load Condition		
	Minimum	Nominal	Maximum
$\kappa = \omega L/R_L$	0.01	0.2	1/3
Average output voltage, V_0	152.2 V	115.8 V	105.8 V
Peak-to-peak ripple voltage to output voltage, V_{op}/V_0	0.0018	0.02	0.027
Output voltage to peak input voltage, V_0/V_{Im}	0.92	0.70	0.64
Average load current, I_0	0.33 A	5.0 A	7.6 A
Peak reactor current to load current, I_{xm}/I_0	4.6	2.3	2.0
Rms reactor current to load current, I_{xe}/I_0	1.9	1.3	1.2

continued

Ratio	Load Condition		
	Minimum	Nominal	Maximum
Rms ac supply line current to load			
current, I_{Ie}/I_0	1.9	1.3	1.2
Power factor of filter circuit, P.F.	0.68	0.74	0.73

Using the nominal load voltage and current values as before, additional information on the characteristics of the remainder of the power supply circuit may be obtained. Since the diode forward voltage drop is small compared with the output voltage in this example it will be neglected. The peak reactor current I_{Xm} and the peak current through the rectifier diodes is 11.5 A (5.0×2.3). The rms reactor current is found to be 6.5 A (5.0×1.3) which is also the value of the rms ac supply line current for the full-wave bridge combination. The power factor P.F. is 0.74.

Although the two examples which are provided to illustrate the use of the design and performance curves in Figure 2.6 are specified for either all continuous-conduction mode or all discontinuous-conduction mode operation over the load range, there is no reason for restricting the operation to one or the other modes. The designer has the choice of specifying the nominal load conditions and ripple requirement to fall in either mode and to enter the other mode under changing load conditions, provided the V_0/V_{Im} requirement can be met with appropriate turns ratio.

2.5 Conclusions

Methods for analyzing full-wave rectifier LC-filter circuits were presented and these methods were used to develop design procedures for the rectifier-filter combination. The procedures cover the cases of operation in

both the continuous-conduction mode and the discontinuous-conduction mode. An algorithm was presented which permits rapid determination of the periodic steady state in the discontinuous mode using digital computation. Using the results for both modes of conduction, a set of design curves was generated, providing a straightforward procedure for designing both the inductor and the capacitor for a rectifier-filter circuit operating in the discontinuous mode and continuous mode. The use of the parameter $\kappa = \omega L / R_L$ and the establishment of a boundary condition on κ for separating the two modes of operation were shown to be useful in choosing operating conditions.

From the design curves, currents in the different windings of the transformer and in each diode can be calculated. Using these curves, a designer can select the inductor, the capacitor, the diodes, and the transformer to meet various applications requirements. Some of the requirements are: varying ac input supply magnitude, maximum allowable ripple, maximum rms and peak diode and transformer-winding currents, minimum power factor and load conditions. Two examples were presented to illustrate the design procedures using the design curves. Results of experimental and simulation runs using the inductor and capacitor design values agree closely with the results predicted from the design procedures.

CHAPTER III

ANALYSIS AND DESIGN OF LC-FILTERS WITH NON-ZERO SOURCE IMPEDANCE

3.1 Introduction

In Chapter II, an analysis and design procedure for the LC-filter circuit operating both in the continuous and discontinuous modes, with the sinusoidal voltage source impedance assumed to be zero, is presented. In this chapter, the basic concept used in Chapter II is extended to include LC-filter circuits with non-zero source impedance. Figure 3.1 shows the transformer-rectifier-filter networks of Figure 2.1 connected to a sinusoidal voltage source through a primary-circuit impedance consisting of a series resistance $\left(\frac{N_p}{N_s}\right)^2 R_I$ and a series inductance $\left(\frac{N_p}{N_s}\right)^2 L_I$. This series resistance-inductance combination represents the Thevenin equivalent impedance of the usually encountered source and line impedance as seen from the transformer primary-winding terminals. The transformers, shown in Figure 3.1, are assumed to be ideal. As mentioned earlier, the inclusion of source impedance in the design algorithm yields a more accurate and complete design. For each value of the dimensionless parameter ρ , defined as R_I/R_L where R_I is the value of source resistance referred to the secondary side of the trans-

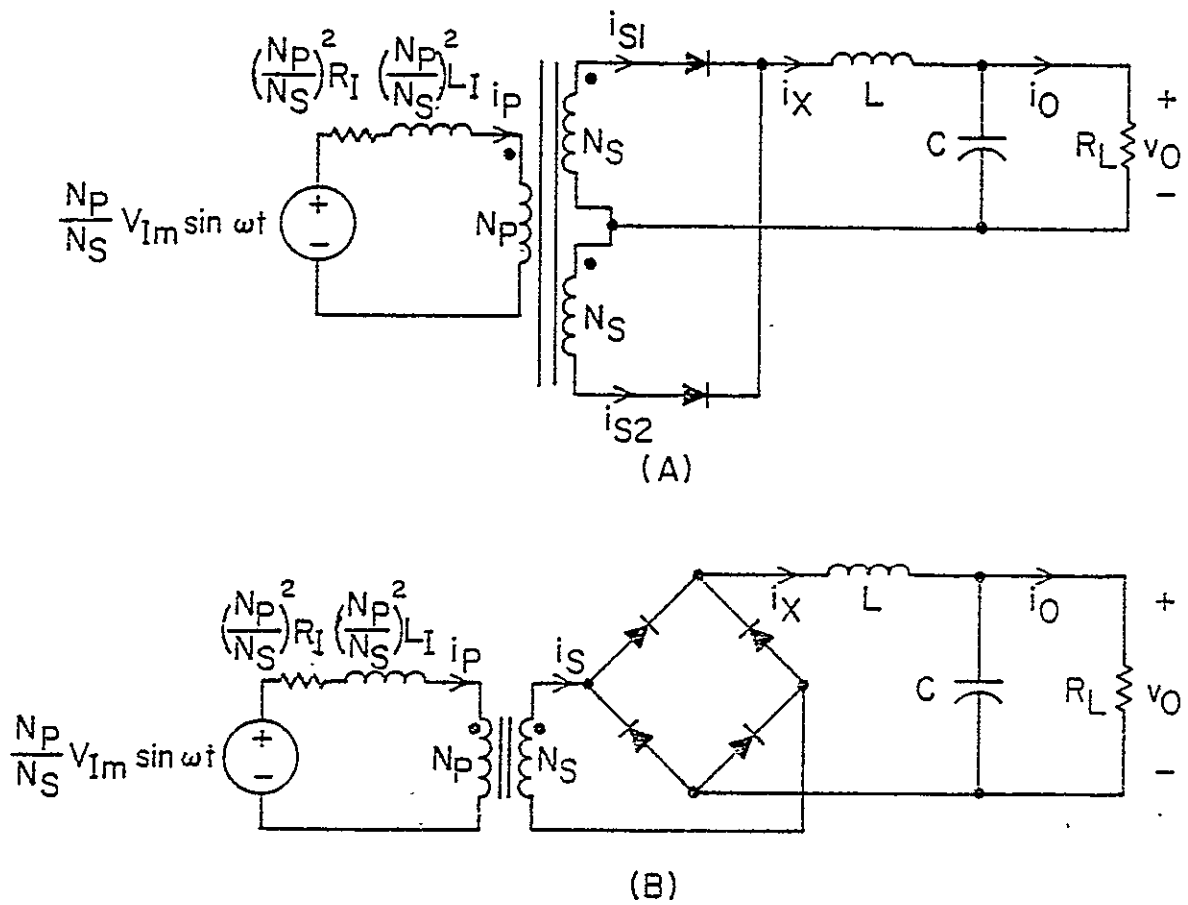


Figure 3.1. LC-filter circuit with non-zero source impedance $(\frac{N_P}{N_S})^2 R_I$ and $(\frac{N_P}{N_S})^2 L_I$ supplied by (A) center-tapped transformer rectifier and (B) full-wave bridge rectifier.

former, a set of design curves, similar to one shown in Figure 2.6 for the case with zero-source impedance, is obtained.

The format of the presentation here follows closely that of the preceding chapter. The derivations of the useful expressions are presented in Appendices C and D.

3.2 Analysis

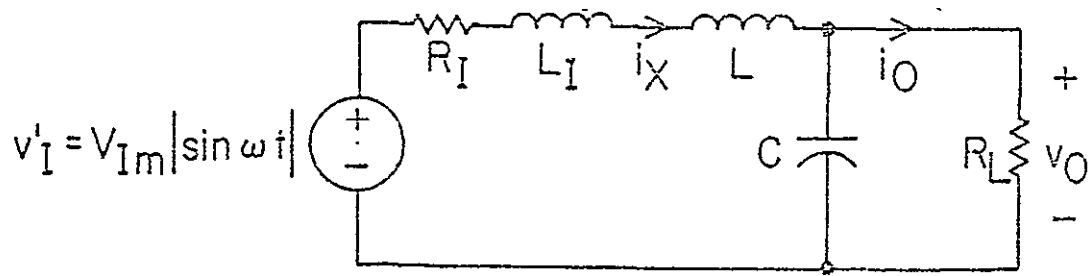
As in Chapter II, in the continuous-conduction mode, linear circuit analysis techniques are employed, while in the case of the discontinuous mode, the method of analysis requires computer solutions of the piecewise-linear differential equations.

3.2.1 Continuous-Conduction Mode

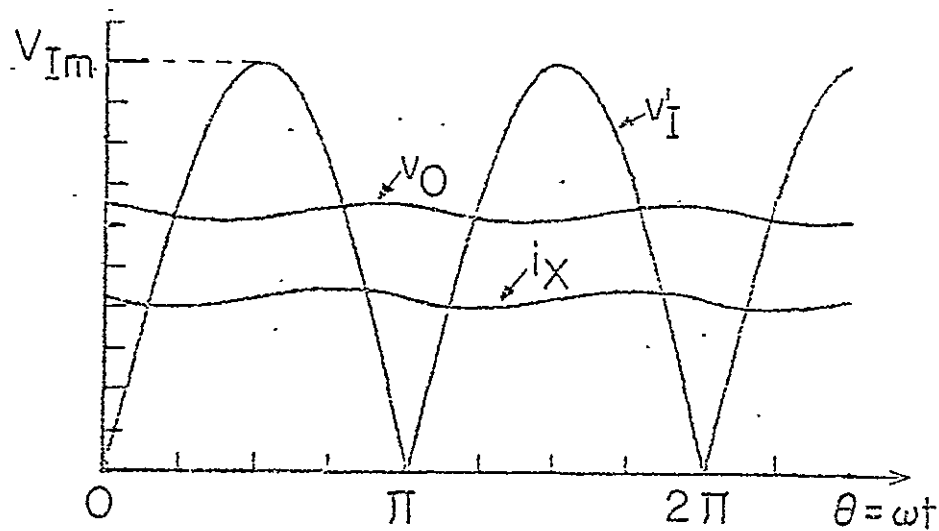
Assuming ideal diodes, the equivalent circuit for both of the configurations in Figure 3.1 is given in Figure 3.2 along with typical waveforms of inductor current and output voltage. The two dimensionless parameters ω_N and κ defined in Chapter II are redefined as $\omega \sqrt{L_{eq}C}$ and $\omega L_{eq}/R_L$, where $L_{eq} = L_I + L$ is the sum of the source inductance referred to the secondary side of the transformer and the filter inductance. As described in Chapter II, the equivalent input voltage v_I' may be approximated by the following expression when the circuit is operated in the continuous-conduction mode:

$$v_I' = \frac{4V_{Im}}{\pi} \left(\frac{1}{2} - \frac{1}{3} \cos 2\theta \right) \quad (3.1)$$

Using the expression in (3.1) and the transfer function of the filter, which includes R_I and L_I , the useful relations for various voltage and cur-



(A)



(B)

Figure 3.2. (A) Equivalent diagram for the rectifier-filter circuits with non-zero source impedance operating in the continuous-conduction mode.

(B) Associated voltage and current waveforms from computer solutions of circuit equations.

rent components can be derived as in Chapter II with the results:

DC output voltage:

$$V_0 = \frac{2V_{Im}}{\pi(\rho+1)} \quad (3.2)$$

Peak-to-peak ripple voltage:

$$V_{Op} = \frac{8V_{Im}}{3\pi} \left/ \left(\sqrt{(\rho+1-4\omega_N^2)^2 + (2\kappa+(2\rho\omega_N^2/\kappa))^2} \right) \right. \quad (3.3)$$

Rms inductor current:

$$I_{Xe} = \frac{4V_{Im}}{\pi R_L} \left[\sqrt{\frac{1}{4(\rho+1)^2} + \frac{(1+4\omega_N^4/\kappa^2)}{18\{(\rho+1-4\omega_N^2)^2 + (2\kappa+(2\rho\omega_N^2/\kappa))^2\}}} \right] \quad (3.4)$$

Peak inductor current:

$$I_{Xm} = \frac{4V_{Im}}{\pi R_L} \left[\frac{1}{2(\rho+1)} - \frac{1}{3} \sqrt{\frac{1+(4\omega_N^4/\kappa^2)}{(\rho+1-4\omega_N^2)^2 + (2\kappa+(2\rho\omega_N^2/\kappa))^2}} \right] \quad (3.5)$$

3.2.2 Discontinuous-Conduction Mode

The equivalent circuit when diodes are conducting is the same as for the continuous mode and is repeated in Figure 3.3(A). The output voltage v_{01} is obtained from the solution of the following equation:

$$\omega_N^2 \frac{d^2 v_{01}}{d\theta^2} + [\kappa + (\rho\omega_N^2/\kappa)] \frac{dv_{01}}{d\theta} + (\rho+1)v_{01} = V_{Im} |\sin(\theta-\theta_0)| \quad (3.6)$$

The value of inductor current i_{X1} is given by

$$i_{X1} = \omega C \frac{dv_{01}}{d\theta} + \frac{v_{01}}{R_L} \quad (3.7)$$

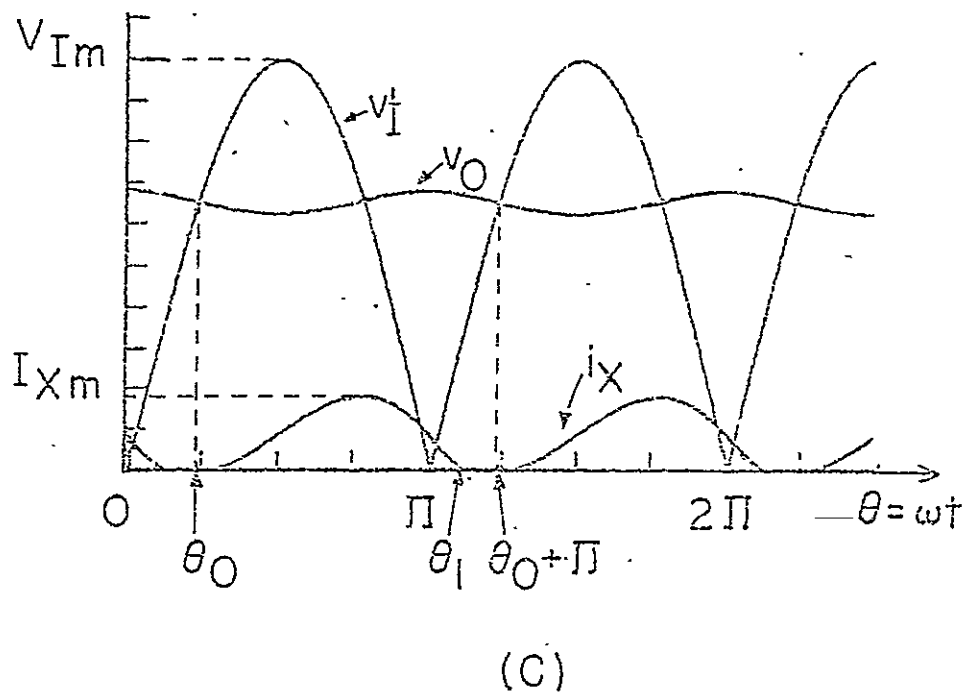
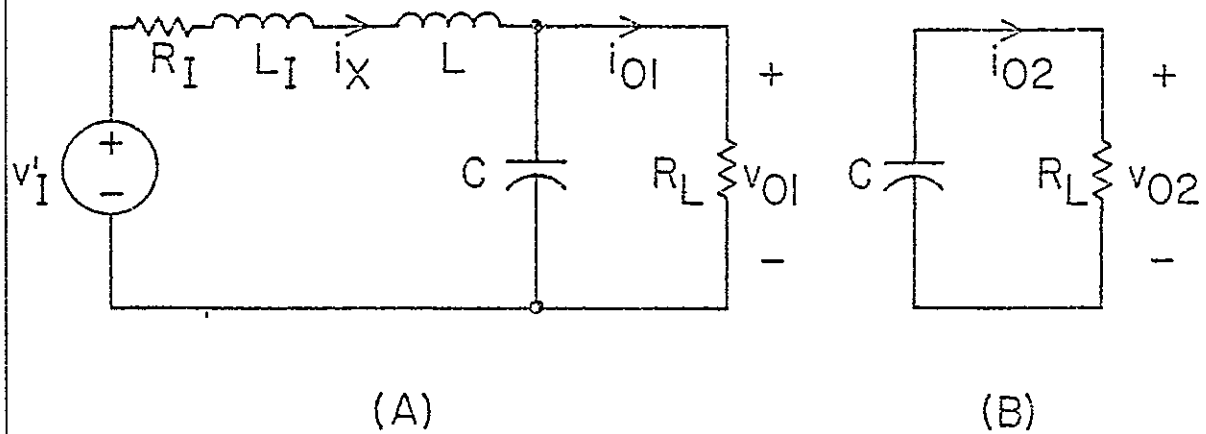


Figure 3.3. Equivalent diagrams for the rectifier-filter circuits with non-zero source impedance operating in the discontinuous-conduction mode during interval (A) when diodes are conducting and (B) when diodes are not conducting. (C) Associated voltage and current waveforms from computer solutions of circuit equations.

The solutions to (3.6) and (3.7) for the values of $(\kappa + (\rho\omega_N^2/\kappa)) < 4\omega_N^2(\rho+1)$, yield the following expressions for v_{01} and i_{x1} :

$$v_{01}(\theta) = A_{vr}\sin\theta + B_{vr}\cos\theta + \exp(\beta_r\theta)[C_{vr}\sin(\alpha_r\theta) + D_{vr}\cos(\alpha_r\theta)] \quad (3.8)$$

$$i_{x1}(\theta) = \frac{1}{R_L} \left[A_{ir}\sin\theta + B_{ir}\cos\theta + \exp(\beta_r\theta)[C_{ir}\sin(\alpha_r\theta) + D_{ir}\cos(\alpha_r\theta)] \right] \quad (3.9)$$

For the values of $[\kappa + (\rho\omega_N^2/\kappa)] > 4\omega_N^2(\rho+1)$, the expressions for v_{01} and i_{x1} are given by the following:

$$v_{01}(\theta) = A_{vr}\sin\theta + B_{vr}\cos\theta + C'_{vr}\exp(\alpha_1\theta) + D'_{vr}\exp(\alpha_2\theta) \quad (3.10)$$

$$i_{x1}(\theta) = \frac{1}{R_L} \left[A_{ir}\sin\theta + B_{ir}\cos\theta + C'_{ir}\exp(\alpha_1\theta) + D'_{ir}\exp(\alpha_2\theta) \right] \quad (3.11)$$

The values for the various coefficients depend on κ , ω_N , ρ , and θ_0 , and expressions for them are derived in Appendices C and D.

When the diodes are not conducting, the equivalent circuit is that shown in Figure 3.3(B). The output voltage v_{02} and current i_{x2} for this part of the cycle are described by the equations (2.13) and (2.14) given in Chapter II. The expression for v_{02} is obtained, as given in Chapter II,

$$v_{02}(\theta) = v_{02}(\theta_1)\exp[-(\theta-\theta_1)/\omega CR_L] \quad (3.12)$$

The steady-state solutions for v_0 and i_x are obtained by solving the transcendental equations given by (3.8), (3.9), (3.10), (3.11), (3.12), and (2.14), as described in Chapter II.

3.2.3 Critical Condition

The critical condition, $\kappa = \kappa_{cr}$, corresponds to the boundary between the two modes of operation. Using (3.1), the inductor current i_X in the continuous mode is given by the expression:

$$i_X = \frac{4V_{Im}}{\pi} \left[\frac{1}{2R_L(\rho+1)} - \frac{\cos(2\theta-\psi)}{3|Z(j2\omega)|} \right] \quad (3.13)$$

where $|Z(j2\omega)|$ and ψ are given by the following

$$|Z(j2\omega)| = R_L \sqrt{\left[\frac{(\rho+1-4\omega_N^2)^2 + [2\kappa+(2\rho\omega_N^2/\kappa)]^2}{1 + (4\omega_N^4/\kappa^2)} \right]} \quad (3.14)$$

$$\psi = \arctan [2\kappa+(2\rho\omega_N^2/\kappa)]/(\rho+1-4\omega_N^2) - \arctan (2\omega_N^2/\kappa) \quad (3.15)$$

For the critical condition, the minimum value of i_X just reaches zero or

$$\frac{4V_{Im}}{\pi} \left[\frac{1}{2R_L(\rho+1)} - \frac{1}{3|Z(j2\omega)|} \right] = 0 \quad (3.16)$$

Rearranging (3.16) and substituting for $|Z(j2\omega)|$ from (3.14) leads to the relationship:

$$\sqrt{\left(\frac{(\rho+1-4\omega_N^2)^2 + [2\kappa+(2\rho\omega_N^2/\kappa)]^2}{1+(4\omega_N^4/\kappa^2)} \right)} = \frac{2}{3} (\rho+1) \quad (3.17)$$

Squaring (3.17) and simplifying yields the expression

$$F(\kappa, \omega_N) = 0 = \kappa^4 + \kappa^2 \left[\frac{5}{36}(\rho+1)^2 - 2\omega_N^2 + 4\omega_N^4 \right] - \frac{\omega_N^4}{9} (4+8\rho-5\rho^2) \quad (3.18)$$

For a given value of ω_N , the value of $\kappa = \kappa_{cr}$ which satisfies the critical condition $F(\kappa, \omega_N) = 0$ given by (3.18), can be found. A plot of κ_{cr} versus ω_N for various values of ρ is shown in Figure 3.4. For a given ρ , the value of κ_{cr} approaches asymptotically $(\sqrt{1+2\rho-1.25\rho^2})/3$ for values of ω_N greater than 5.0.

3.3. Design and Performance Curves and Approximate Relationships

3.3.1 Design and Performance Curves

Using the methods of analysis described in the previous sections, sets of curves, similar to the one shown in Figure 2.6, for various assigned values of $\rho = R_I/R_L$ were generated and are shown in Figure 3.5 through Figure 3.12. Following the method in Chapter II, these curves may be used to calculate various performance factors for LC-filters with non-zero source impedance. As seen from the design curves shown in Figure 3.5 through Figure 3.12, for a particular value of κ and ω_N , the value of the ratio of peak-to-peak ripple voltage to average output voltage V_{0p}/V_0 slowly increases with an increase in the value for the parameter $\rho = R_I/R_L$. The values for the other performance parameters V_0/V_{Im} , P.F., I_{Xe}/I_0 , and I_{Xm}/I_0 , decrease with increasing ρ . The dependence of the parameters V_0/V_{Im} , I_{Xe}/I_0 , and I_{Xm}/I_0 on ρ is greater in the discontinuous mode than in the continuous mode. The dependence of the other two parameters V_{0p}/V_0 , and P.F. on ρ is greater in the continuous mode than in the discontinuous mode. In the continuous mode, the parameter V_0/V_{Im} is most sensitive to variations in ρ and I_{Xe}/I_0 is least sensitive. In the discontinuous mode, the parameter V_0/V_{Im} is again most sensitive to variations in ρ and P.F. is least sensitive. Thus, for particular values of the filter components L , C , and R_L , the ripple ratio

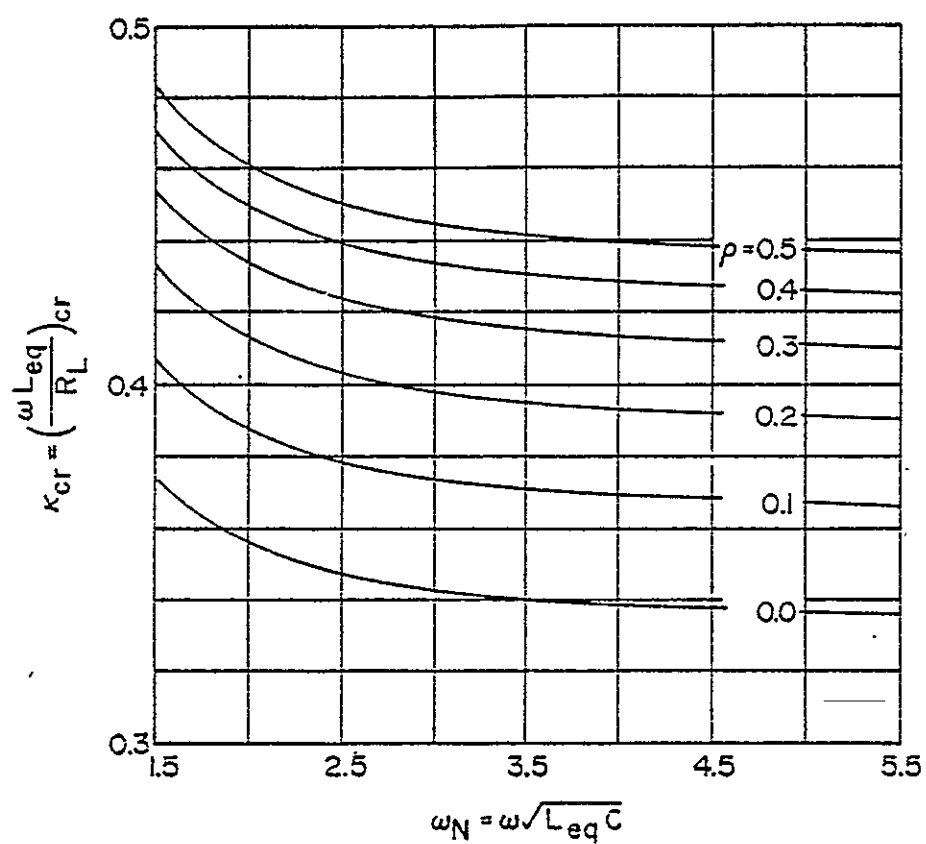


Figure 3.4. Plot of κ_{cr} versus ω_N for various values of $\rho = R_I/R_L$.

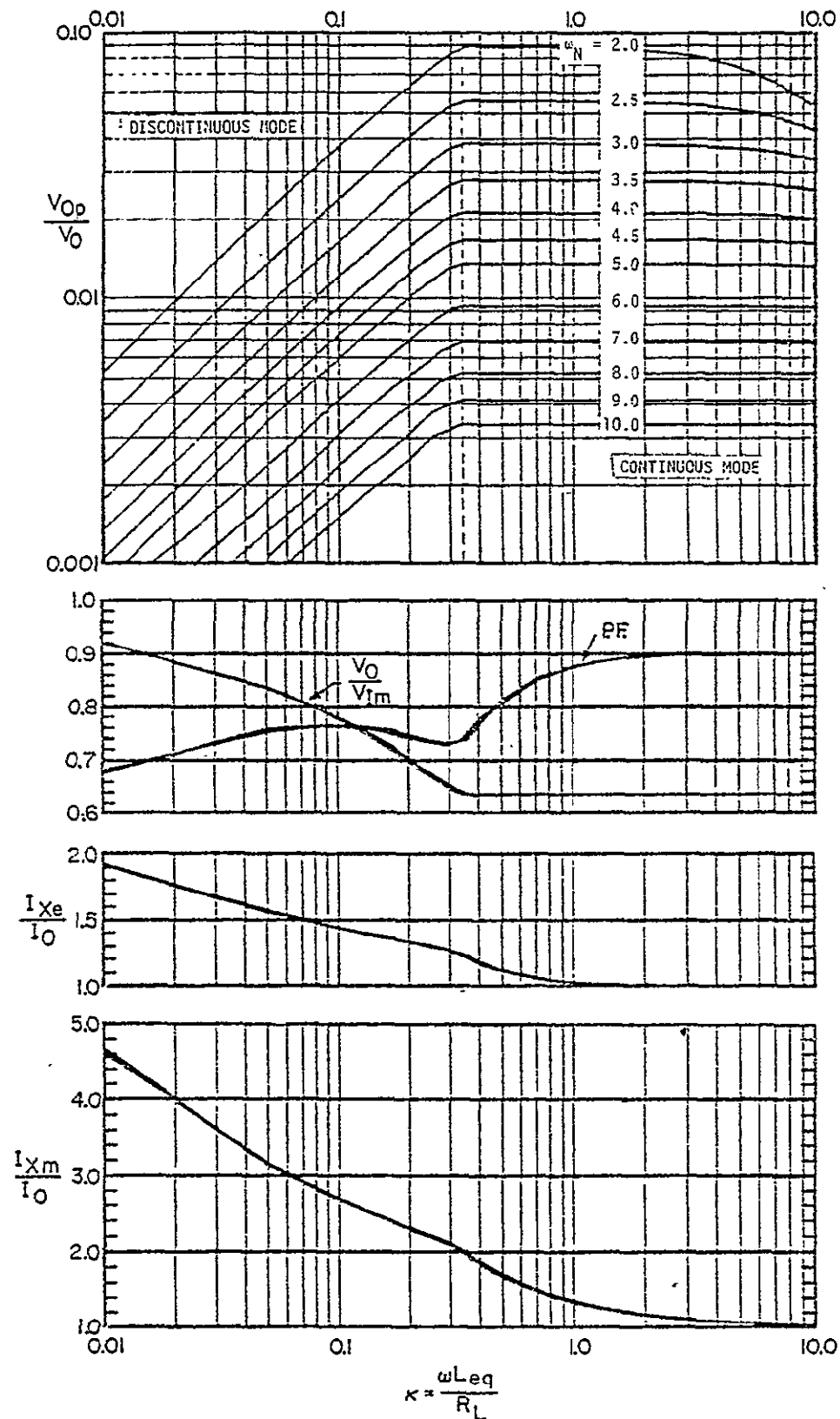


Figure 3.5 Design and performance curves for LC-filters with $\rho=0.0005$ operating both in the continuous- and discontinuous-conduction modes.

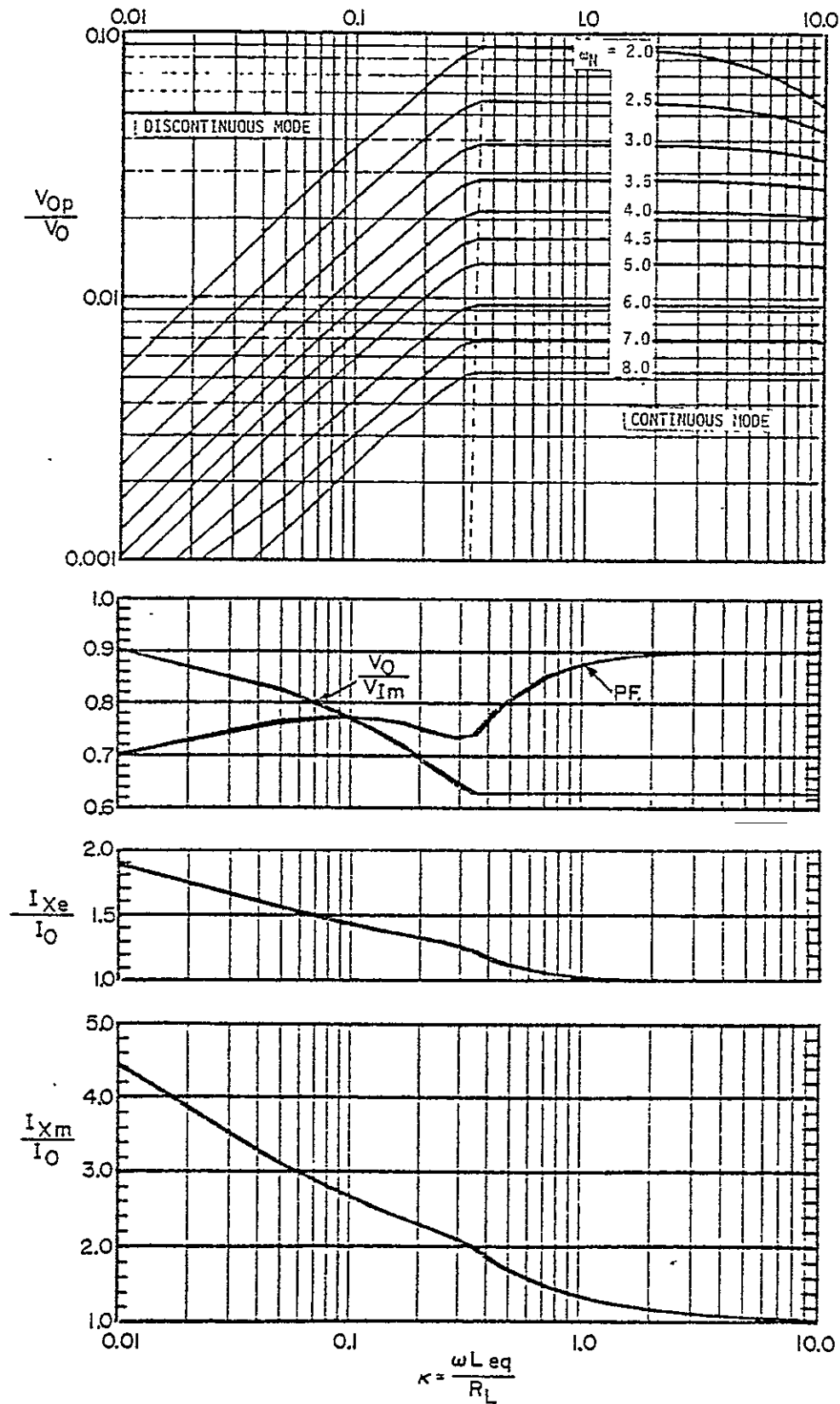


Figure 3.6 Design and performance curves for LC-filters with $\rho = 0.01$ operating both in the continuous- and discontinuous conduction modes.

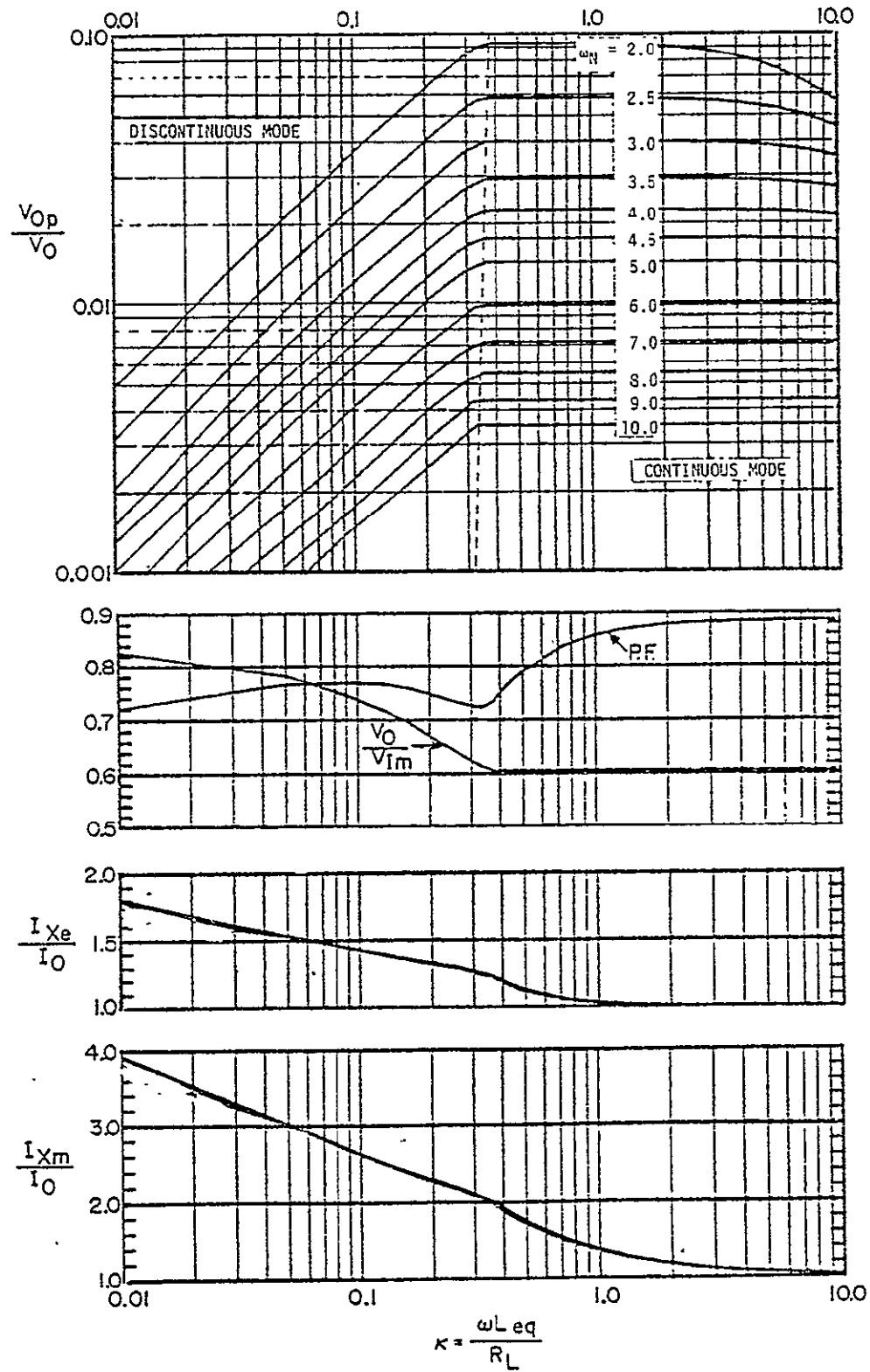


Figure 3.7 Design and performance curves for LC-filters with $\rho = 0.05$ operating both in the continuous- and discontinuous-conduction modes.

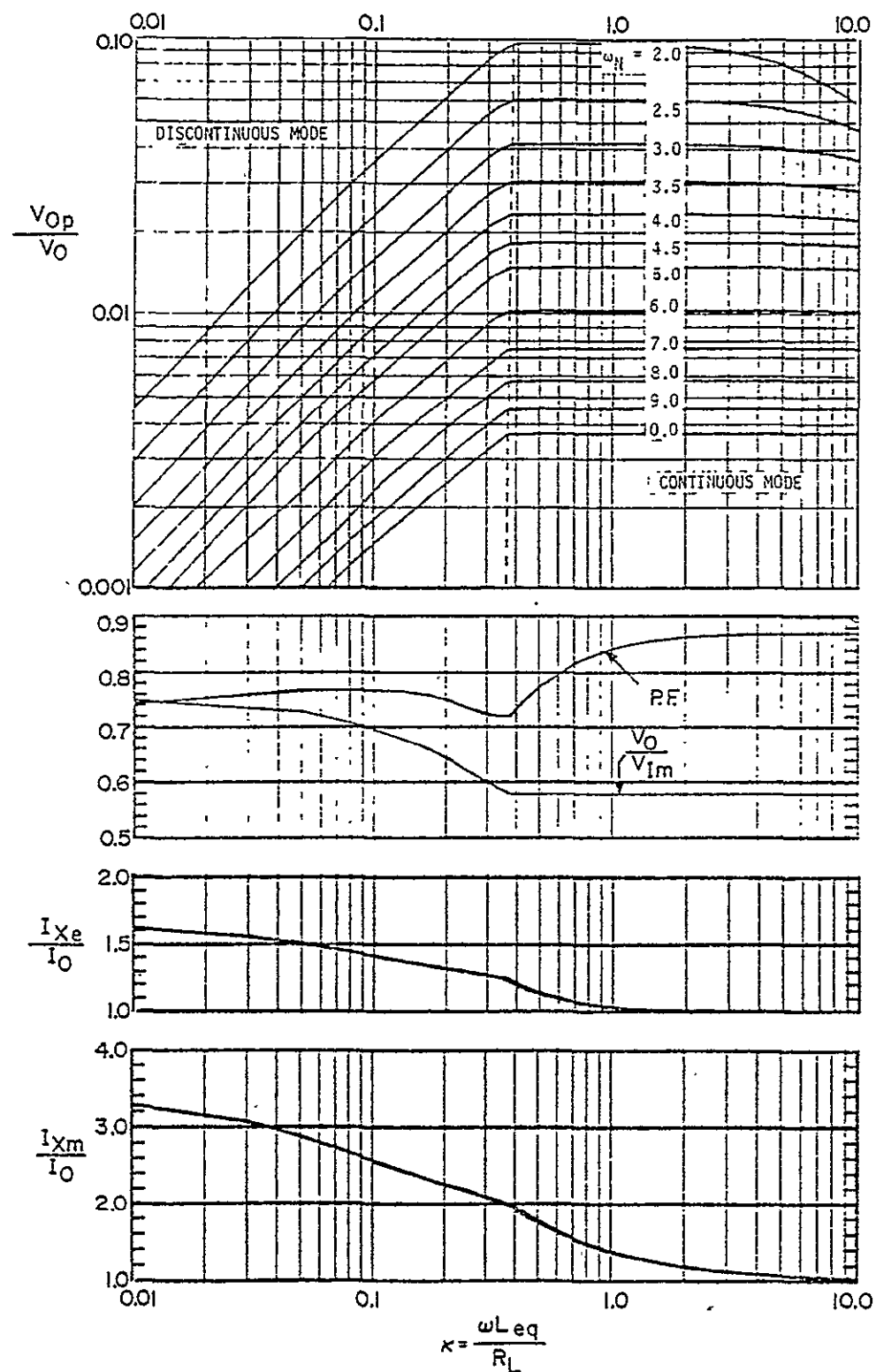


Figure 3.8 Design and performance curves for LC-filters with $\rho = 0.1$ operating both in the continuous- and discontinuous-conduction modes.

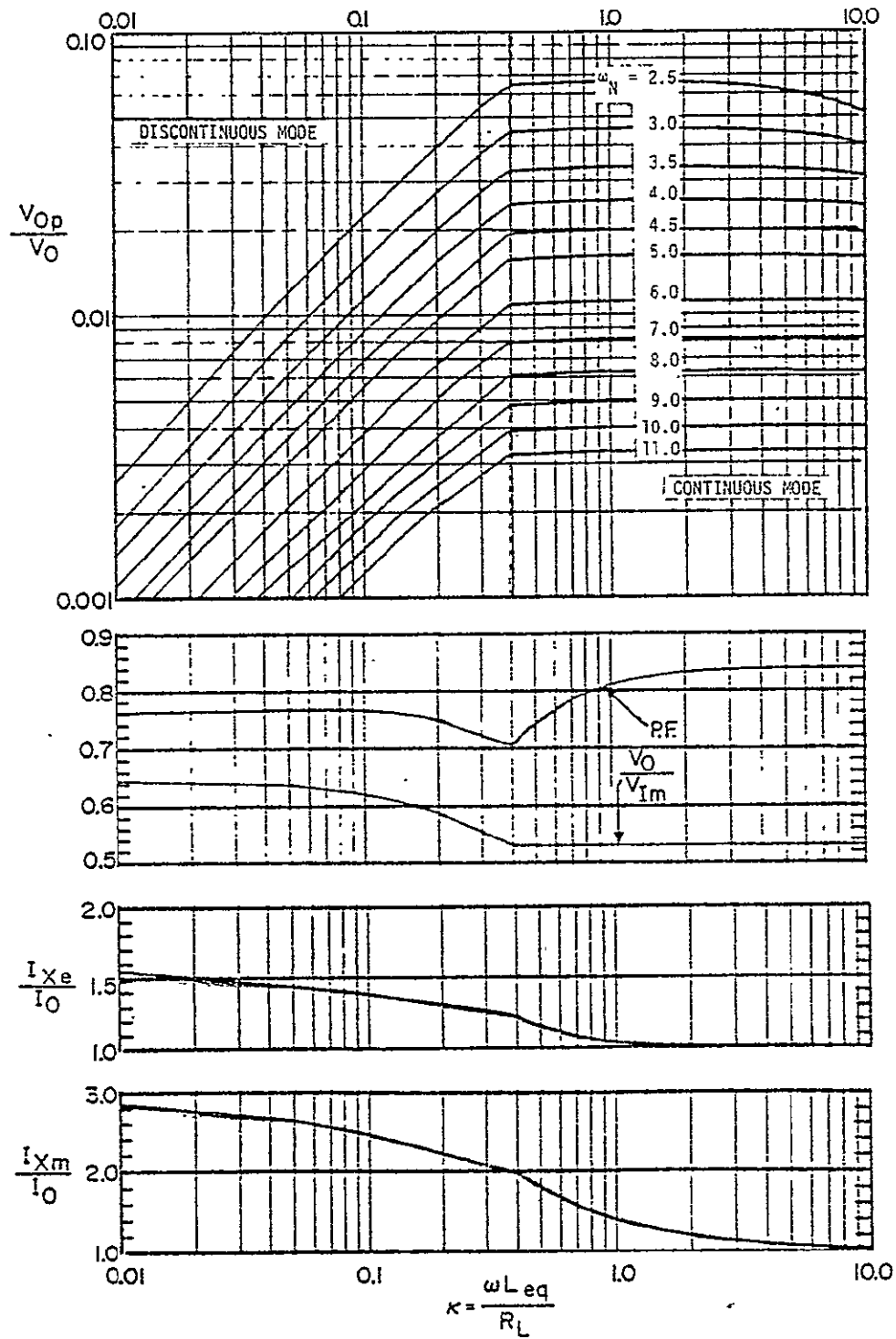


Figure 3.9 Design and performance curves for LC-filters with $\rho = 0.2$ operating both in the continuous- and discontinuous-conduction modes.

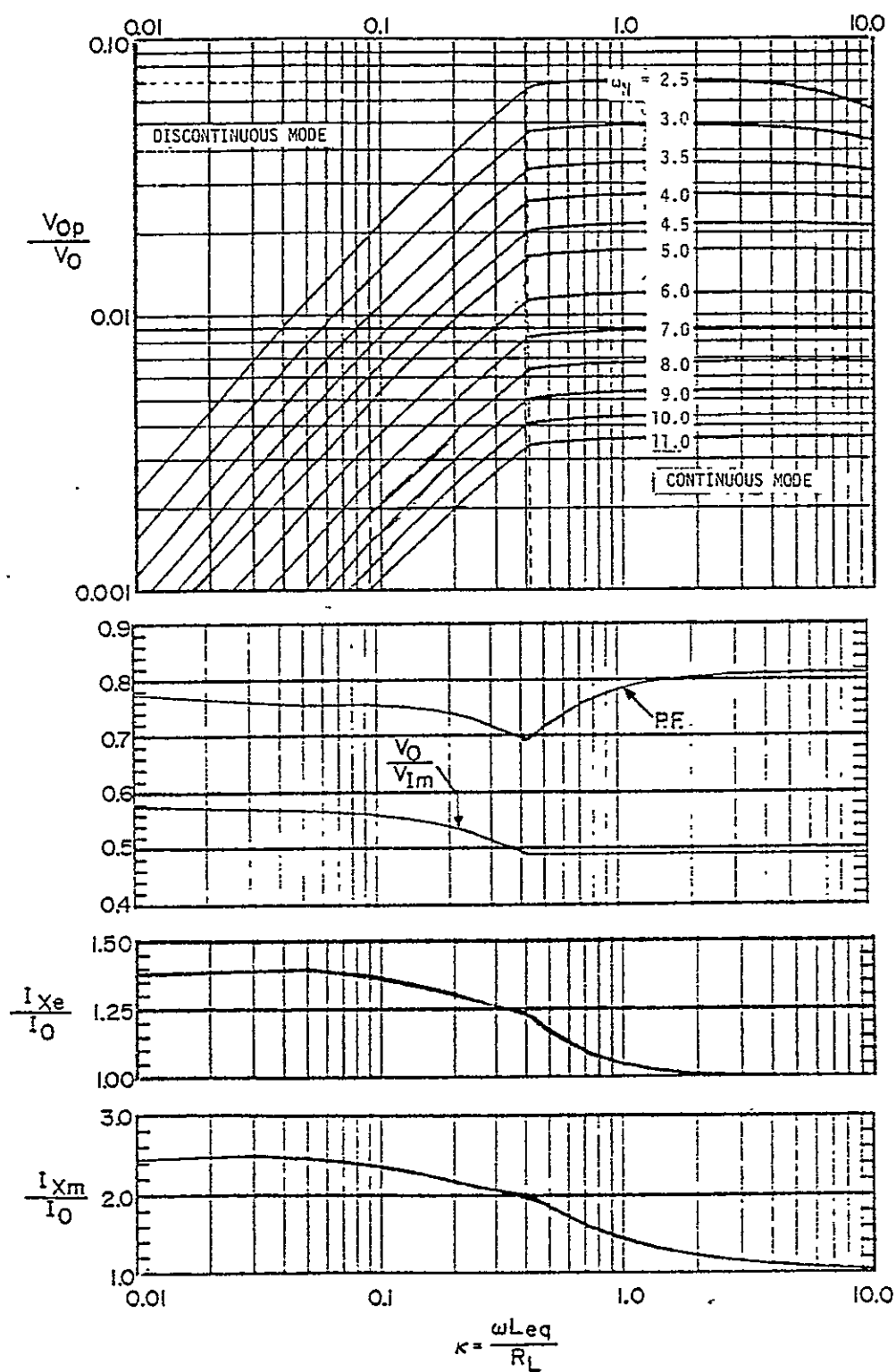


Figure 3.10 Design and performance curves for LC-filters with $\rho = 0.3$ operating both in the continuous- and discontinuous-conduction modes.

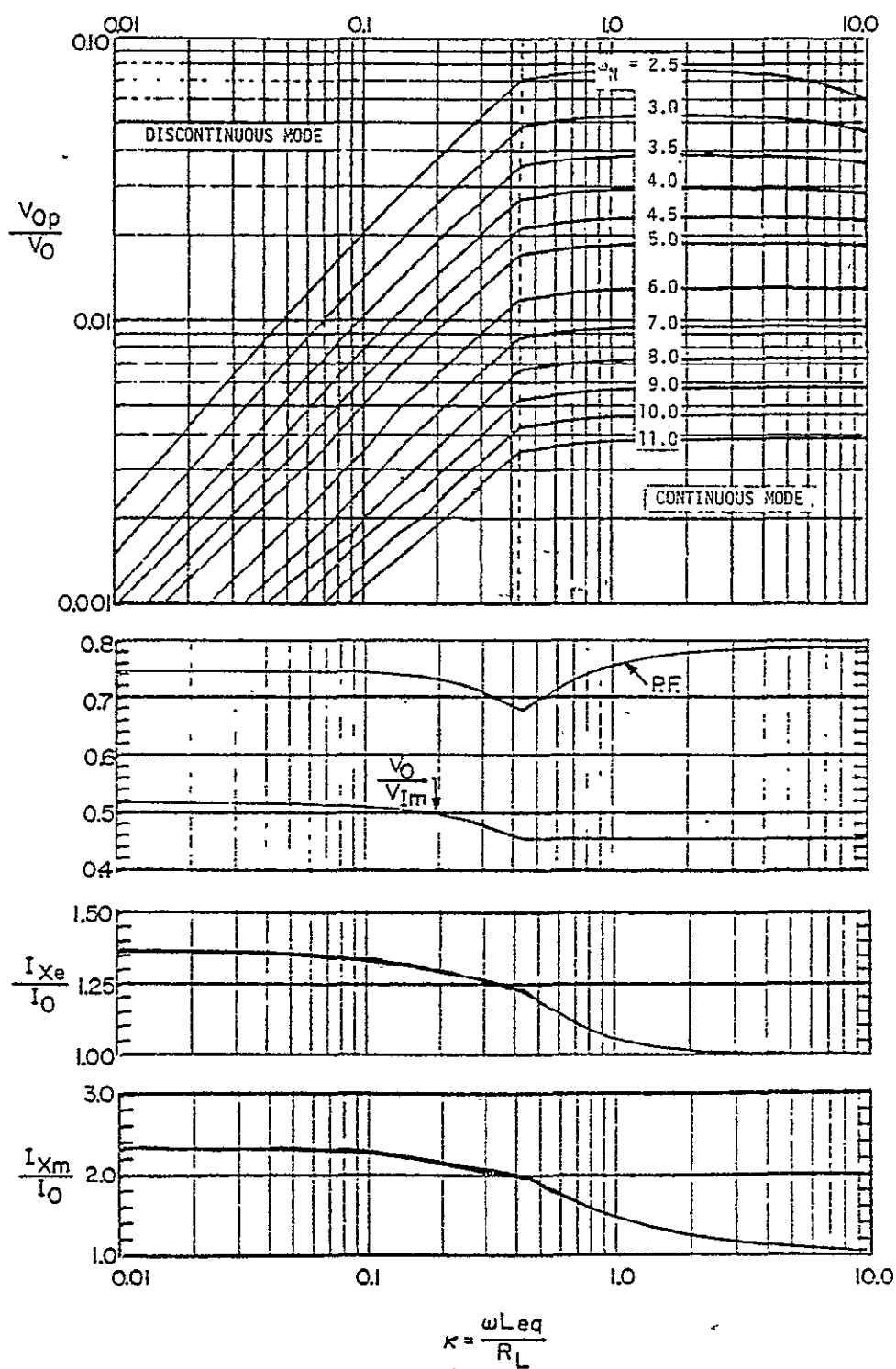


Figure 3.11 Design and performance curves for LC-filters with $\rho = 0.4$ operating both in the continuous- and discontinuous-conduction modes.

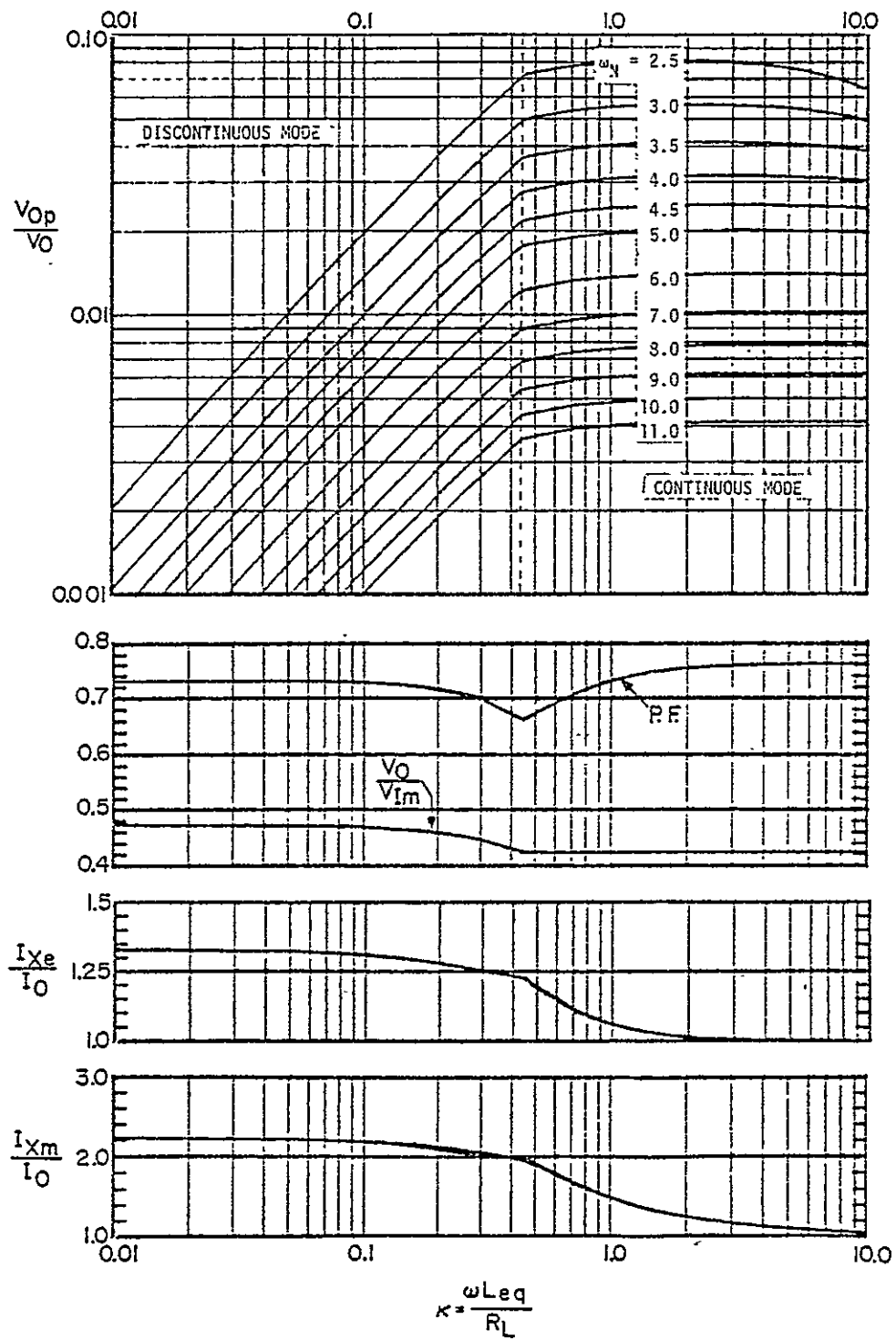


Figure 3.12 Design and performance curves for LC-filters with $\rho = 0.5$ operating both in the continuous- and discontinuous-conduction modes.

V_{Op}/V_0 calculated from the design curves for the zero source impedance case shown in Figure 2.6 is smaller than that obtained from the design curves presented in this chapter. The values for V_0/V_{Im} and P.F. read from the curves in Figure 2.6 are greater than those obtained from the design curves which take source impedance into account. Thus, the design curves presented in Chapter II give optimistic values for the ripple ratio V_{Op}/V_0 , output voltage to peak input voltage ratio V_0/V_{Im} , and power factor P.F.

For the filters with values of ρ other than those given in Figure 3.5 through Figure 3.12, the design should be accomplished using one of the design curves shown in Figure 3.5 through Figure 3.12 corresponding to the value of ρ greater than and closest to the specified ρ . To illustrate the design procedure, an example is worked out in Section 3.4.

3.3.2 Approximate Analytical Design Relationships

For filters operating in the continuous-conduction mode, the design curves for various performance parameters, shown in Figure 3.5 through Figure 3.12, can be approximated by analytical design relationships given in Table 3.1. These approximate design relationships are obtained from the exact relationships given in Appendix C under the assumption that $4\omega_N^2$ is much larger than 1 and κ . In Table 3.1, analytical expressions are given for the design relationships $V_{Op}/V_0(\kappa, \omega_N, \rho)$, $V_0/V_{Im}(\rho)$, $I_{Xe}/I_0(\kappa, \rho)$, $I_{Xm}/I_0(\kappa, \rho)$, and P.F. (κ, ρ) . In addition to the design relationships for various performance parameters, expressions for the inverse relationships $\omega_N(V_{Op}/V_0, \kappa, \rho)$, $\kappa(V_{Op}/V_0, \omega_N, \rho)$, $\kappa(I_{Xe}/I_0, \rho)$, and $\kappa(I_{Xm}/I_0, \rho)$ are also given. In the continuous mode, V_0/V_{Im} is independent of κ and hence there is no inverse

Table 3.1. Approximate design and performance relationships for LC-filters with non-zero source impedance operating in the continuous-conduction mode.

$\frac{V_{0p}}{V_0}(\kappa, \omega_N, \rho)$	$\frac{4(\rho+1)}{3\sqrt{(\rho+1-4\omega_N^2)^2 + (2\kappa+(2\rho\omega_N^2/\kappa))^2}}$
$\frac{V_0}{V_{Im}}(\rho)$	$\frac{2}{\pi(\rho+1)}$
$\frac{I_{Xe}}{I_0}(\kappa, \rho)$	$\sqrt{1 + \frac{(\rho+1)^2}{18\kappa^2}}$
$\frac{I_{Xm}}{I_0}(\kappa, \rho)$	$1 + \frac{\rho+1}{3\kappa}$
$P.F(\kappa, \rho)$	$\frac{2\sqrt{2}}{\sqrt{1 + (\rho+1)/18\kappa^2} \left[\pi(\rho+1) - 2\rho\sqrt{1 + (\rho+1)/18\kappa^2} \right]}$
$\omega_N(V_{0p}/V_0, \kappa, \rho)$	$\left[\frac{(\rho+1)^2}{9(V_{0p}/V_0)^2} - \kappa^2 \right]^{\frac{1}{4}}$
$\kappa(V_{0p}/V_0, \omega_N, \rho)$	$\sqrt{\frac{4(\rho+1)^2}{9(V_{0p}/V_0)^2} - 4\omega_N^4}$
$\kappa(I_{Xe}/I_0, \rho)$	$\frac{\rho+1}{3\sqrt{2}\sqrt{(I_{Xe}/I_0)^2 - 1}}$
$\kappa(I_{Xm}/I_0, \rho)$	$\frac{\rho+1}{3[(I_{Xm}/I_0) - 1]}$

relationship $\kappa(V_0/V_{Im}, \rho)$ given in Table 3.1. The expression for another inverse relationship $\kappa(P.F., \rho)$ is also omitted because of the complexity of the expression.

For the discontinuous case, the performance curves for each value of ρ can be approximated by the design relationships given in Table 3.2. The dependency of the various expressions on ρ is by means of coefficients a , b , a_1 , a_2 , a_3 , b_1 , b_2 , b_3 , c_1 , c_2 , c_3 , d_1 , d_2 , and d_3 . The values for these coefficients for various values of ρ are given in Table 3.3.

A good approximation to the (V_{Op}/V_0) curve shapes in Figure 3.5 through Figure 3.12 is obtained if they are considered to be straight lines parallel to each other and starting at the continuous mode point for $\kappa = (\sqrt{1+2\rho-1.25\rho^2})/3$. As seen from Figure 3.5 through Figure 3.12, the other performance parameters, V_0/V_{Im} , P.F., I_{Xe}/I_0 , and I_{Xm}/I_0 are weakly dependent on ω_N and hence are approximated by polynomials of second degree passing through the points on the curves for these latter parameters as functions of κ only. The values computed from the approximate relationship for (V_{Op}/V_0) lie within ten percent of the values read from the curves while the values computed from the approximate relationship for the other performance parameters, V_0/V_{Im} , P.F., I_{Xe}/I_0 , and I_{Xm}/I_0 , lie within five percent of the values read from the curves.

3.4 Design Example

To illustrate the usefulness of the performance curves presented in the preceding section, an example of a filter design is discussed.

Table 3.2 Approximate design and performance relationships for LC-filters with non-zero source impedance operating in the discontinuous-conduction mode.

$\frac{V_{0p}}{V_0}(\kappa, \omega_N, \rho)$	$(a_0 \kappa^{b_0})/\omega_N^2$
$\frac{V_0}{V_{Im}}(\kappa, \rho)$	$a_1 - a_2 \log \kappa + a_3 (\log \kappa)^2$
$\frac{I_{Xe}}{I_0}(\kappa, \rho)$	$b_1 - b_2 \log \kappa + b_3 (\log \kappa)^2$
$\frac{I_{Xm}}{I_0}(\kappa, \rho)$	$c_1 - c_2 \log \kappa + c_3 (\log \kappa)^2$
$P.F(\kappa, \rho)$	$d_1 - d_2 \log \kappa + d_3 (\log \kappa)^2$
$\omega_N(V_{0p}/V_0, \kappa, \rho)$	$\sqrt{\frac{a_0 \kappa^{b_0}}{(V_{0p}/V_0)}}$
$\kappa(V_{0p}/V_0, \omega_N, \rho)$	$10^{\left(\frac{\log[\omega_N^2(V_{0p}/V_0)/a_0]}{b_0}\right)}$
$\kappa(V_0/V_{Im}, \rho)$	$10^{\left(\frac{a_2 - \sqrt{a_2^2 + 4a_3[(V_0/V_{Im}) - a_1]}}{2a_3}\right)}$
$\kappa(I_{Xe}/I_0, \rho)$	$10^{\left(\frac{b_2 - \sqrt{b_2^2 + 4b_3[(I_{Xe}/I_0) - b_1]}}{2b_3}\right)}$
$\kappa(I_{Xm}/I_0, \rho)$	$10^{\left(\frac{c_2 - \sqrt{c_2^2 + 4c_3[(I_{Xm}/I_0) - c_1]}}{2c_3}\right)}$
$\kappa(P.F., \rho)$	$10^{\left(\frac{d_2 - \sqrt{d_2^2 + 4d_3[(P.F.) - d_1]}}{2d_3}\right)}$
Parameters $a_0, b_0, a_1, a_2, a_3, b_1, b_2, b_3, c_1, c_2, c_3, d_1, d_2$, and d_3 are constants which depend on $\rho = R_I/R_L$. See Table 3.3.	

Table 3.3. Values for the various coefficients which introduce the dependency on ρ in the approximate analytical relationships given in Table 3.2.

Coefficients	$\rho = R_I/R_L$							
	0.0005	0.01	0.05	0.1	0.2	0.3	0.4	0.5
a_0	0.768	0.773	0.796	0.821	0.866	0.902	0.913	0.927
b_0	0.761	0.763	0.783	0.806	0.848	0.885	0.894	0.911
a_1	0.465	0.463	0.449	0.441	0.432	0.421	0.402	0.385
a_2	0.402	0.395	0.389	0.357	0.271	0.199	0.156	-0.123
a_3	-0.086	-0.088	0.099	-0.1	-0.08	-0.06	-0.049	-0.03
b_1	1.108	1.057	1.071	1.073	1.095	1.07	1.128	1.151
b_2	0.266	0.263	0.379	0.407	0.352	0.423	0.289	0.23
b_3	0.067	0.078	-0.023	-0.066	-0.062	-0.138	-0.086	-0.06
c_1	1.553	1.518	1.538	1.458	1.532	1.603	1.759	1.836
c_2	0.729	0.872	1.056	1.336	1.234	1.095	0.723	0.506
c_3	0.398	0.309	0.043	-0.21	-0.3	-0.336	-0.217	-0.155
d_1	0.658	0.605	0.642	0.653	0.645	0.648	0.621	0.633
d_2	0.198	0.275	0.211	0.183	0.181	0.147	0.179	0.141
d_3	-0.093	-0.116	-0.085	-0.068	-0.061	-0.042	-0.059	-0.045

3.4.1 Example

The values of the inductor and capacitor elements in an LC-filter circuit with nominal output voltage $V_0 = 30$ V, nominal load current $I_0 = 10$ A, and a peak-to-peak ripple voltage to average output voltage of 4% are to be found. The supply voltage to the rectifiers is provided by the secondary windings of a center-tapped transformer, the primary of which is excited by an ac supply of 117 V rms at 400 Hz. The secondary ac supply voltage is 30 V rms. The source resistance $\left(\frac{N_p}{N_s}\right)^2 R_I$ is given as approximately 4.5 ohm and source inductance $\left(\frac{N_p}{N_s}\right)^2 L_I$ is approximately 80 μ H.

Using the specified primary and secondary supply voltages, the turns ratio N_s/N_p is computed to be 1/3.9. The value of the source resistance referred to the load side R_I , is approximately 0.3 ohm. The value of source inductance referred to the load side L_I is 5.26 μ H. Under nominal output voltage and load conditions, the ratio $V_0/V_{Im} = 0.707$ and from the set of performance curves for $\rho = R_I/R_L = 0.1$ in Figure 3.8, $\kappa = 0.09$ from the V_0/V_{Im} curve and the filter circuit operates in the discontinuous mode. To meet the nominal ripple requirement of $V_{Op}/V_0 = 0.04$, the curve corresponding to $\omega_N = 2.0$ is selected which provides a somewhat smaller value of ripple. Using the definitions of $\kappa = \omega L_{eq}/R_L$ and $\omega_N = \omega \sqrt{L_{eq}C}$, and the value of $R_L = 3$ ohms for the nominal load, the values for the L_{eq} and C are computed to be: $L_{eq} = 0.1074$ mH, $C = 5896$ μ F. The values of the filter components are computed to be: $L = L_{eq} - L_I = 0.1022$ mH; $C = 5896$ μ F.

If the filter circuit is to operate in the discontinuous-conduction mode for all loads within the range of the curves in Figure 3.8, κ can vary

from 0.01 to 0.363. Examining the characteristics of the combined transformer-rectifier-filter circuit over this range in κ yields the following results:

Ratio (Using Non-Zero Source Impedance Curves)	Load Condition		
	Minimum	Nominal	Maximum
$\kappa = \omega L_{eq}/R_L$	0.01	0.09	0.363
Average output voltage, V_0	31.8 V	30.1 V	24.6 V
Peak-to-peak ripple voltage to output voltage, V_{0p}/V_0	0.0046	0.032	0.096
Output voltage to peak input voltage, V_0/V_{Im}	0.75	0.71	0.58
Average load current, I_0	1.2 A	10.0 A	33.1 A
Peak reactor current to load current, I_{xm}/I_0	3.3	2.6	2.0
Rms reactor current to load current, I_{xe}/I_0	1.6	1.42	1.26
Rms transformer secondary current to load current, I_{Se}/I_0	1.13	1.01	0.89
Power factor of filter circuit, P.F.	0.74	0.77	0.72

Using the nominal load voltage and current values as before, additional information on the characteristics of the remainder of the power supply circuit may be obtained. Using the values $(I_{xm}/I_0) = 2.6$ and $(I_{xe}/I_0) = 1.42$ read from the performance curves for $\kappa = 0.09$, the peak reactor current I_{xm} and the peak current through the rectifier diodes is 26 A and the rms reactor current is found to be 14.2 A. The rms secondary winding current I_{Se} in a center-tapped secondary is equal to the rms reactor current I_{xe} divided by $\sqrt{2}$ and has a value of 10.0 A. The rms primary winding current, neglecting magnetizing current and using a turns

ratio of $1/3.9$ is 3.64 A. The power factor P.F. is approximately 0.77. Since the diode forward voltage drop is small compared with the output voltage in this example it will be neglected. When the output voltage is small, however, the diode forward voltage drop can be a significant fraction of the output voltage V_0 . As mentioned earlier, the diode forward voltage drop was neglected in the analysis since this factor would have added an additional parameter to the family of performance curves presented earlier. There seems to be no easy way to take diode forward voltage drop into account for the case when the filter is operating in the discontinuous-conduction mode without adding an additional normalized parameter to the design curves.

The above example is now repeated for comparison purposes, using the design curves which assume zero-source resistance which were presented in Chapter II.

Starting again with the ratio $V_0/V_{Im} = 0.707$, from the curve for this parameter in Figure 2.6, κ is approximately 0.2. To meet the minimum ripple requirements $V_{Op}/V_0 = 0.04$, the curve corresponding to $\omega_N = 3.0$ is selected. Using the value of $R_L = 3$ ohms for the nominal load, the values of the filter components are computed to be: $L = 0.238$ mH; $C = 5986$ μ F.

Examining the characteristic of the combined transformer-rectifier-filter circuit over the range of κ in the discontinuous mode yields the following results

Ratio (Using Zero-Source Impedance Curves)	Load Condition		
	Minimum	Nominal	Maximum
$\kappa = \omega L/R_L$	0.01	0.2	1/3
Average output voltage, V_0	39.1 V	30.1 V	27.2 V
Peak-to-peak ripple voltage to output voltage, V_{Op}/V_0	0.0024	0.028	0.038

Ratio (Using Zero-Source Impedance Curves)	Load Condition		
	Minimum	Nominal	Maximum
Output voltage to peak input voltage, V_0/V_{Im}	0.92	0.71	0.64
Average load current, I_0	0.65 A	10.0 A	15.1 A
Peak reactor current to load current, I_{xm}/I_0	4.6	2.3	2.0
Rms reactor current to load current, I_{xe}/I_0	1.9	1.34	1.23
Rms transformer secondary current to load current, I_{Se}/I_0	1.34	0.95	0.87
Power factor of filter circuit	0.68	0.74	0.73

The peak reactor current I_{xm} and peak reactor current through the diodes is 23 A. The rms reactor current is found to be 13.4 A. The rms secondary winding current is 9.47 A. The rms primary winding current is similarly given as 3.44 A. The value of inductor L calculated using the design curves in Chapter II is greater than that needed in the design which takes source impedance into account, although the required value of capacitance C essentially remains the same. Thus the peak and rms values of reactor current, and the ripple ratio V_{0p}/V_0 are smaller for the filter designed using zero-source impedance curves than that designed using the curves presented in this chapter. For further comparison using the values for the filter components L and C as computed using the zero-source impedance curves, i.e., $\kappa = 0.2$ and $\omega_N = 3.0$, the value for V_0/V_{Im} from the curves for $\rho = 0.1$ in Figure 3.8 is found to be 0.64. Thus the actual dc output voltage V_0 obtained using the filter designed with the curves presented in Chapter II instead of the curves for $\rho = 0.1$ is 27.1 V instead of the

desired 30 V.

An example using the approximate analytical design relationships is presented next.

3.4.2 Example Using Approximate Design Relationships

The same filter design example is repeated here using the approximate analytical design relationships given in Tables 3.1, 3.2, and 3.3.

Starting again with the ratio $V_0/V_{Im} = 0.707$, from the relationship for $\kappa(V_0/V_{Im}, \rho)$ in Table 3.2, and using the values for a_1 , a_2 , and a_3 corresponding to $\rho = 0.1$ from Table 3.3, κ is computed to be 0.087. Using the specified value of $V_{Op}/V_0 = 0.04$ in the relationship for $\omega_N(V_{Op}/V_0, \kappa, \rho)$ in Table 3.2, the value for ω_N is found to be 1.7. Using the value of $R_L = 3$ ohms for the nominal load, the values for the L_{eq} and C are computed to be: $L_{eq} = 0.1039$ mH; $C = 4404$ μ F. The values of the filter components are computed to be: $L = 0.0983$ mH; $C = 4404$ μ F.

Calculating the characteristic of the combined transformer-rectifier-filter circuit over the range of κ in the discontinuous mode yields the following results:

Ratio (Using Approximate Analytical Design Relationships)	Load Condition		
	Minimum	Nominal	Maximum
$\kappa = \omega L_{eq}/R_L$	0.01	0.087	0.363
Average output voltage, V_0	32.1 V	29.9 V	24.5 V
Peak-to-peak ripple voltage to output voltage, V_{Op}/V_0	0.0069	0.039	0.125
Output voltage to peak input voltage, V_0/V_{Im}	0.755	0.706	0.578

Ratio (Using Approximate Analytical Design Relationships)	Load Condition		
	Minimum	Nominal	Maximum
Average load current, I_0	1.22 A	9.98 A	34.1 A
Peak reactor current to load current, I_{Xm}/I_0	3.29	2.64	2.01
Rms reactor current to load current, I_{Xe}/I_0	1.62	1.43	1.25
Rms transformer secondary current to load current, I_{Se}/I_0	1.14	1.01	0.88
Power factor of filter circuit, P.F.	0.74	0.76	0.72

The results obtained for the three examples for the nominal load conditions are summarized below.

Example A: Using Zero Source Impedance Curves

Example B: Using Non-Zero Source Impedance Curves

Example C: Using Approximate Analytical Design Relationships

Ratio	Example		
	A	B	C
$\kappa = \omega L_{eq}/R_L$	0.2	0.09	0.087
Average output voltage, V_0	30.1 V	30.1 V	29.9 V
Peak-to-peak ripple voltage to output voltage, V_{Op}/V_0	0.028	0.032	0.039
Output voltage to peak input voltage, V_0/V_{Im}	0.71	0.71	0.706
Average load current, I_0	10.0 A	10.0 A	9.98 A
Peak reactor current to load current, I_{Xm}/I_0	2.3	2.6	2.64
Rms reactor current to load current, I_{Xe}/I_0	1.34	1.42	1.43

Ratio	A	Example B	C
Rms transformer secondary current to load current, I_{Se}/I_0	0.95	1.01	1.01
Power factor of filter circuit, P.F.	0.74	0.77	0.76

It is seen from the above summary that the results obtained from the approximate analytical design relationships given in Table 3.2 are in good agreement with the results obtained using design curves presented in this chapter.

3.5 Conclusions

Methods for analyzing full-wave rectifier LC-filter circuits operating in the continuous and discontinuous modes with non-zero source impedance were presented in this chapter. The inclusion of source impedance adds an additional normalized parameter $\rho = R_I/R_L$ to the set of design curves which were developed in Chapter II. Using the results of the analysis for both modes of conduction, a set of design curves for various assigned values of ρ was generated.

From the design curves, various performance factors of the filters can be calculated. The source impedance is always present in an actual physical system and its inclusion as a parameter yields a more complete design. An example was presented to illustrate the design procedures using the design curves. To illustrate the effect and importance of source impedance on the design and performance of LC-filters, the same example was repeated using the zero-source impedance design curves presented in Chapter II. Using the values of κ and ω_N obtained from the design procedure using

the curves for zero-source impedance, and working backward through the design curves which take source impedance into account, shows that with the values of κ and ω_N obtained from the design curves in Chapter II, the dc output voltage ratio V_0/V_{Im} will be smaller than the required value, although the ripple ratio V_{Op}/V_0 will be smaller than that for the filter designed using source impedance curves because of the larger inductance value used. In general, as seen from the design and performance curves for the LC-filter circuits with non-zero source impedance, for specified values for the filter components L , C , and R_L , i.e., κ and ω_N , the ripple ratio V_{Op}/V_0 is greater than that obtained from the design curves which do not take source impedance into account. The actual value of the parameter V_0/V_{Im} is also smaller than that obtained from the design curves presented in Chapter II. Thus, a filter design obtained by use of the zero source impedance curves yields a set of parameters leading to an optimistic design in terms of ripple ratio and output voltage to input voltage ratio. In other words, higher values for the filter components L and C , and supply voltage are needed than those calculated from the zero-source impedance design curves to meet the specified requirements of ripple ratio V_{Op}/V_0 and desired output voltage V_0 .

CHAPTER IV

DESIGN OF AIR-GAPPED MAGNETIC-CORE INDUCTORS FOR SUPERIMPOSED DIRECT AND ALTERNATING CURRENTS

4.1 Introduction

Various procedures have been reported in the literature for the design of air-gapped inductors carrying direct current. In most cases, a particular core with known size and shape is first selected for evaluation. The procedure then involves calculating a trial value for the number of turns and the length of the air-gap for the selected core and then analyzing the combination to determine if all the requirements, electrical and mechanical, for the inductor are met. If not met, then either the number of turns or the length of the air-gap is changed from its previous value and the calculations are repeated. The results again are checked against the requirements, thus giving rise in most cases to an iterative trial-and-error procedure applied to the selected core.

All design methods require the use of a considerable amount of magnetic core data which usually can be obtained from core manufacturers. One of the earliest design methods is that presented by Hanna [16] which removes

the trial-and-error process applied to the selected core by using specially prepared magnetic core data. This procedure, however, is limited to inductors with small ac flux excursions and also requires the use of special magnetic core curves which are not readily available for some modern core materials. Two recently developed design procedures by Ray and Sartori [18] and by Mitchell [19] make use of the computer to eliminate the tedium usually associated with the normal trial-and-error process. An important and distinguishing feature among the various methods is the way in which the core incremental permeability data are employed. The methods of [16] and [18] make use of a single incremental permeability curve which corresponds to the condition of very small ac flux excursion. The starting point in these procedures is the specification of the desired inductance L and the direct current I_{DC} in the winding. The method given in [19] and the one presented in this chapter make use of a family of incremental permeability curves and thus allow for large ac flux excursions. These procedures also start with a specified value of inductance operating at a given value of direct current in the winding. However, additional design constraints consisting of the frequency and rms value of the fundamental component of ac voltage across the winding, f and V_{AC} , respectively, are imposed on the design procedure. By making use of the known geometry of the selected air-gap type core, and the specified dc resistance and current-density specifications of the winding, the number of turns N are calculated in [18] and [19]. An optimum air gap corresponding to maximum inductance of the core with winding of turns N is computed by the design procedure in [19]. The value of air gap found in [18] is not optimum in the sense defined above. The procedure by Hanna [16] is presented in detail in the next chapter.

In this chapter two procedures for designing inductors are presented. The first, working from a stored bank of magnetic-material data and core-geometry data, uses a computer to produce a design which is optimized in the sense of minimum core volume and minimum number of winding turns to meet a required minimum inductance over a specified range of circuit operating conditions. The second procedure is somewhat simpler; it does not yield a design which is optimized as defined above, but it has the advantage that the computations may readily be carried out on an electronic pocket calculator. Both design procedures are applicable to most modern magnetic core materials including, for example, grain-oriented silicon steel, supermendur and permalloy. While type C cores are used in the examples presented in this paper, the basic procedures can be extended rather easily to other shapes such as type E cores, ring cores, and certain lamination structures.

4.2 Design Requirements

An inductor for filtering the ripple voltage in dc power supplies usually carries a direct current with an alternating current superimposed. In most cases, the requirements are that the value of the inductance over the anticipated range of circuit operating conditions be no smaller than some specified value which will provide for adequate filtering of the fundamental component of a waveform of frequency f . For such a filter reactor, the ac flux excursion usually is large and is determined by the magnitude and frequency of the fundamental component of voltage-across the reactor. In the procedures developed in this paper, the following specifications are used for the design of filter reactors:

- (1) L , the desired minimum value of inductance in henries.
- (2) I_{DC} , the maximum value of direct current in the winding in amperes.
- (3) V_{AC} , the minimum value of the effective or rms value of ac voltage at the fundamental frequency f across the winding in volts.
- (4) f , the frequency of the fundamental component of voltage appearing across the reactor in hertz.

It can be shown that a filter reactor designed to provide an inductance L at a direct current I_{DC} and a fundamental ac voltage V_{AC} increases in inductance if either the direct current in the winding decreases or the ac voltage across the winding increases. Therefore, a design procedure for minimum specified inductance at a specified maximum direct current and minimum ac voltage will yield a reactor design that satisfies the specification requirements.

4.3 Analysis

In any design problem, a necessary first step toward finding a design procedure is an analytical study of the system to be designed. In the development that follows, the subscript m stands for quantities related to the magnetic-core material and the subscript g stands for quantities related to the air-gap.

The magnetic circuit of the type C core shown in Figure 4.1 is analyzed under the following assumptions. First, the length of the air-gap ℓ_g is quite small compared to the mean magnetic path length ℓ_m of the selected core; therefore, the total mean magnetic path length made up of ℓ_m and ℓ_g is taken to be equal to ℓ_m . Second, since ℓ_g also is small compared to the core build-up and the width of the magnetic tape, fringing flux is very small

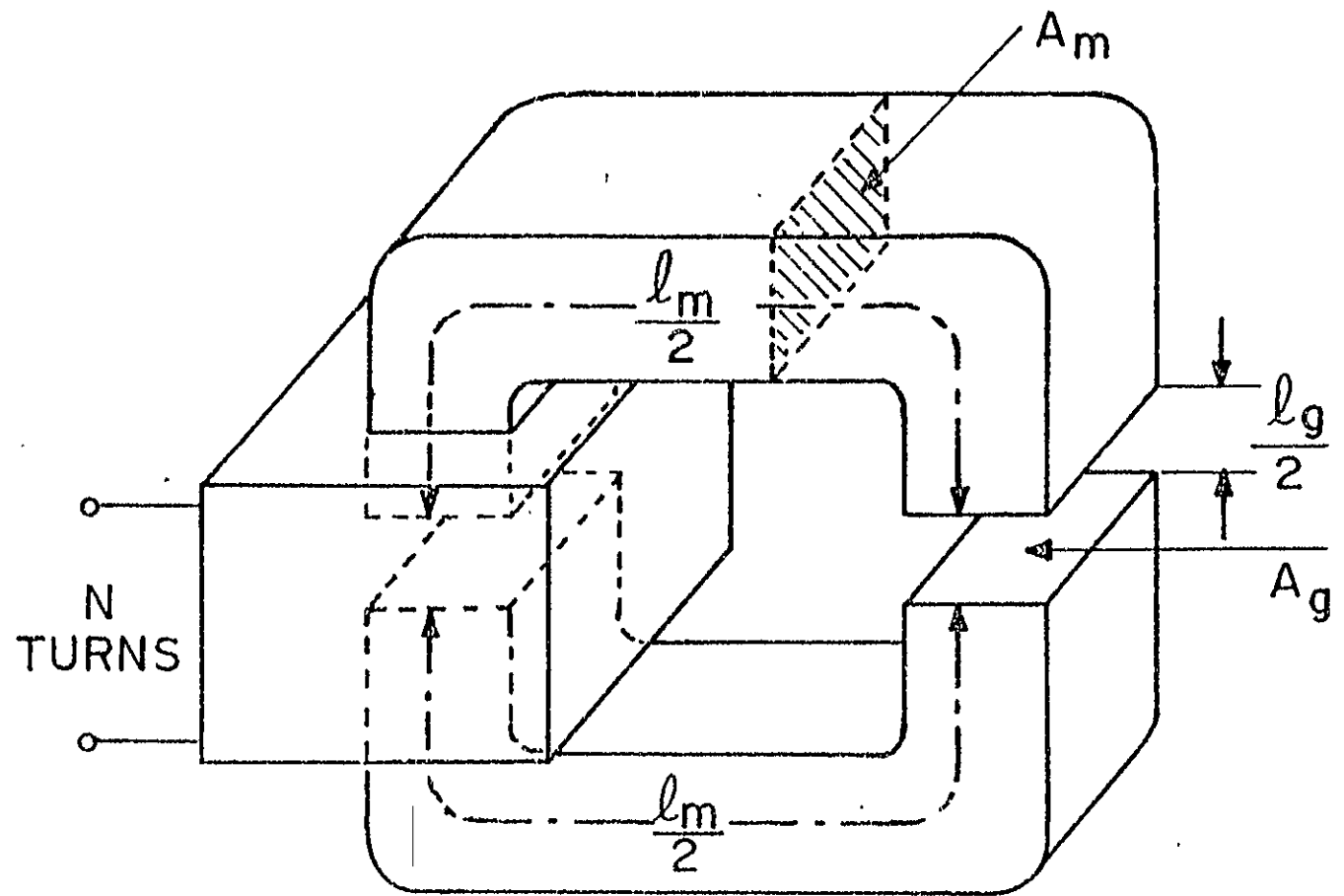


Figure 4.1. Type "C" Core with Associated Winding.

compared to the total flux in the core; therefore, the effective cross-sectional area of the gap portion of the magnetic path A_g is taken to be equal to the effective cross-sectional area of the magnetic material A_m for the selected core.

Having established the nature of the magnetic circuit, attention now is directed to the curves of Figure 4.2. Plotted in the figure are a negative air-gap line relationship between B_g and H , shown as Curve 1, and a normal magnetization curve relating B_m and H_m for a typical magnetic core material which is shown as Curve 2. The inductance of the reactor winding of N turns at a particular operating or quiescent point (H_{mQ}, B_{mQ}) is given by

$$L = \mu_0 \frac{\mu_\Delta}{1 + \mu_\Delta (\ell_g / \ell_m)} \frac{N^2 A_m}{\ell_m} \quad (4.1)$$

where μ_0 is the permeability of free space and μ_Δ is the relative incremental permeability of the magnetic material at the operating point [20]. An expression for V_{AC} , the minimum value of fundamental-component rms voltage across the reactor, is given by (4.2) in terms of the frequency of the fundamental component f , the peak value of the fundamental component of the ac flux density \hat{B}_{mAC} , the number of turns N , and the cross-sectional area of the magnetic core A_m .

$$V_{AC} = \sqrt{2} \pi N f A_m \hat{B}_{mAC} \quad (4.2)$$

These three relationships--the curves of Figure 4.2, Equation (4.1), and Equation (4.2)--can be manipulated, as shown in Appendix E, into an expression of the form

$$F_1(\hat{B}_{mAC}, \mu_\Delta, H_{mQ}, L, I_{DC}, V_{AC}, f, \ell_m, A_m) = 0 \quad (4.3a)$$

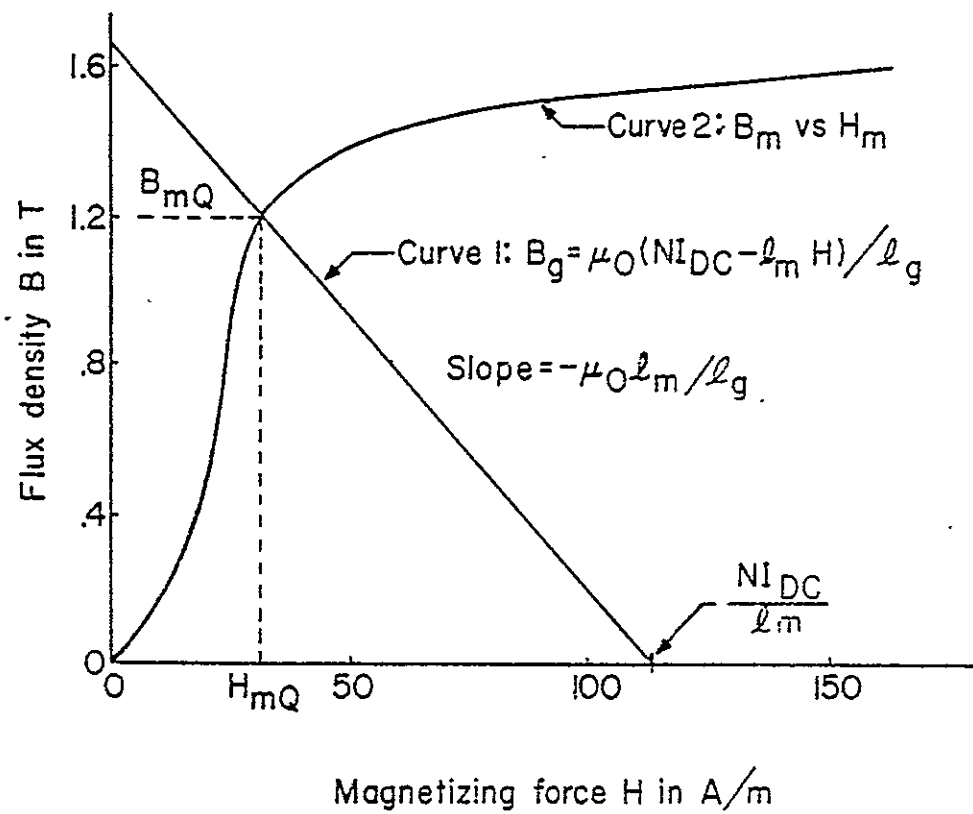


Figure 4.2. Curve 1: Negative air-gap line.

Curve 2: Normal magnetization curve.

The resulting expression derived as (E10) is

$$K_6 \left[\frac{K_5}{\mu_\Delta} - K_1 + \sqrt{K_1^2 - 4(K_2 - \frac{K_3}{\mu_\Delta})} \right] - \frac{K_4}{\hat{B}_{mAC}^2} = 0 \quad (4.3b)$$

where the constants are defined as follows:

$$K_1 \triangleq \mu_0 (2\ell_m A_m H_{mQ} B_{mQ} - I_{DC}^2 L) / A_m B_{mQ}^2 \quad (4.4)$$

$$K_2 \triangleq (\mu_0 \ell_m H_{mQ} / B_{mQ})^2 \quad (4.5)$$

$$K_3 \triangleq \mu_0 \ell_m I_{DC}^2 L / A_m B_{mQ}^2 \quad (4.6)$$

$$K_4 \triangleq (V_{AC} / \sqrt{2\pi f A_m})^2 \quad (4.7)$$

$$K_5 \triangleq 2\ell_m \quad (4.8)$$

$$K_6 \triangleq L / 2\mu_0 A_m \quad (4.9)$$

In (4.3), which is the first of two basic relationships, all but the two parameters \hat{B}_{mAC} and μ_Δ are obtained in a rather direct manner from the performance specifications, from the quiescent operating point on the normal magnetization curve, and from the geometry of the selected core.

The second basic relationship required for the design is obtained from the experimentally determined incremental permeability curves provided by the core manufacturer and is of the form $F_2(\hat{B}_{mAC}, \mu_\Delta, H_{mQ}) = 0$. The $F_2(\cdot) = 0$ relationship is graphically portrayed in Figure 4.3 where the relative incremental permeability μ_Δ is plotted versus the peak ac flux density excursion \hat{B}_{mAC} for various values of the quiescent or bias-point values of H_{mQ} from the normal magnetization curve. Figure 4.3 is a plot of data taken

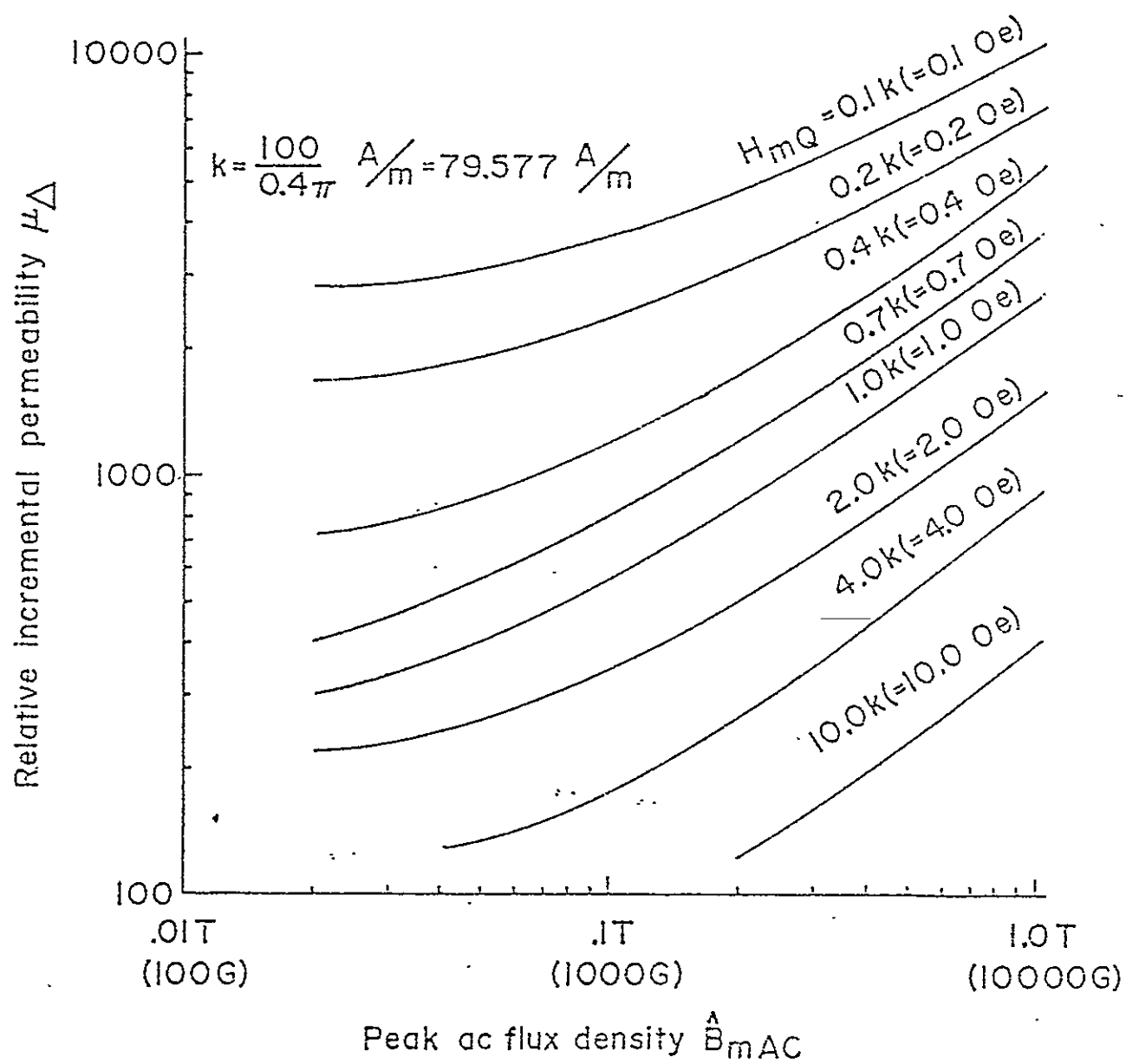


Figure 4.3 Relative incremental permeability versus peak value of sinusoidal flux density excursion for various values of H_{mQ} on normal magnetization curve for 3-percent grain-oriented silicon steel.

from [21] and [22].

Using the analytical base just discussed, the framework for the design procedures is now developed. Assuming that a quiescent point (H_{mQ}, B_{mQ}) for a chosen core material and core geometry is assigned, solution of the two relationships $F_1(\cdot) = 0$ and $F_2(\cdot) = 0$ is obtained simultaneously for \hat{B}_{mAC} and μ_Δ by iteration on a combination of curve reading and computation. Using these solution values, the number of turns N and the air-gap length ℓ_g are determined, respectively, using (4.10), which is a rearrangement of (4.2), and using (4.11), which is derived in Appendix E as (E7).

$$N = V_{AC} / (\sqrt{2} \pi f A_m \hat{B}_{mAC}) \quad (4.10)$$

$$\ell_g = 0.5 K_7 \quad (4.11)$$

where

$$K_7 \triangleq -K_1 + \sqrt{K_1^2 - 4[K_2 - (K_3/\mu_\Delta)]} \quad (4.12)$$

The values of N and ℓ_g obtained for an arbitrary assignment of H_{mQ} correspond to a design matching all of the imposed constraints except the minimum turns requirements and a check for windability. To proceed toward an optimized design for minimum turns for a given set of operating specifications, magnetic material and core geometry, an additional iterative operation is performed in which the quiescent operating point is varied until the solution for N converges to a minimum value. In a later section, two procedures for designing an inductor--one for an assigned quiescent point (H_{mQ}, B_{mQ}) and the other for minimum inductor turns--are illustrated using a common set of specification requirements for the two designs.

4.4 Design Procedures

The objective of both of the design procedures to be discussed is to determine the turns N , the air-gap length ℓ_g , and the wire size which meets the designer's current-density specification for a selected magnetic core material and geometry. The algorithms used in these procedures are explained in this section by reference to Flow Charts 1, 2, and 3 presented in Figures 4.4, 4.5 and 4.7. Individual parts of Flow Charts 1 and 3 will be identified by letters enclosed in brackets, e.g., [A], to which reference will be made in the section illustrating the design procedures by means of an example.

In Flow Chart 1, Figure 4.4, starting with the assumption that a suitable core has been chosen and that a suitable quiescent point (H_{mQ}, B_{mQ}) has been obtained in some manner, the algorithm for computing the number of turns N and the air-gap length ℓ_g is demonstrated. An integral part of this procedure is the simultaneous solution of the two relationships $F_1(\cdot) = 0$ and $F_2(\cdot) = 0$ to obtain values of \hat{B}_{mAC} and μ_Δ which are used in computing N and ℓ_g . The algorithm used to compute N and ℓ_g developed in this chart is used as a sub-algorithm in the two remaining charts.

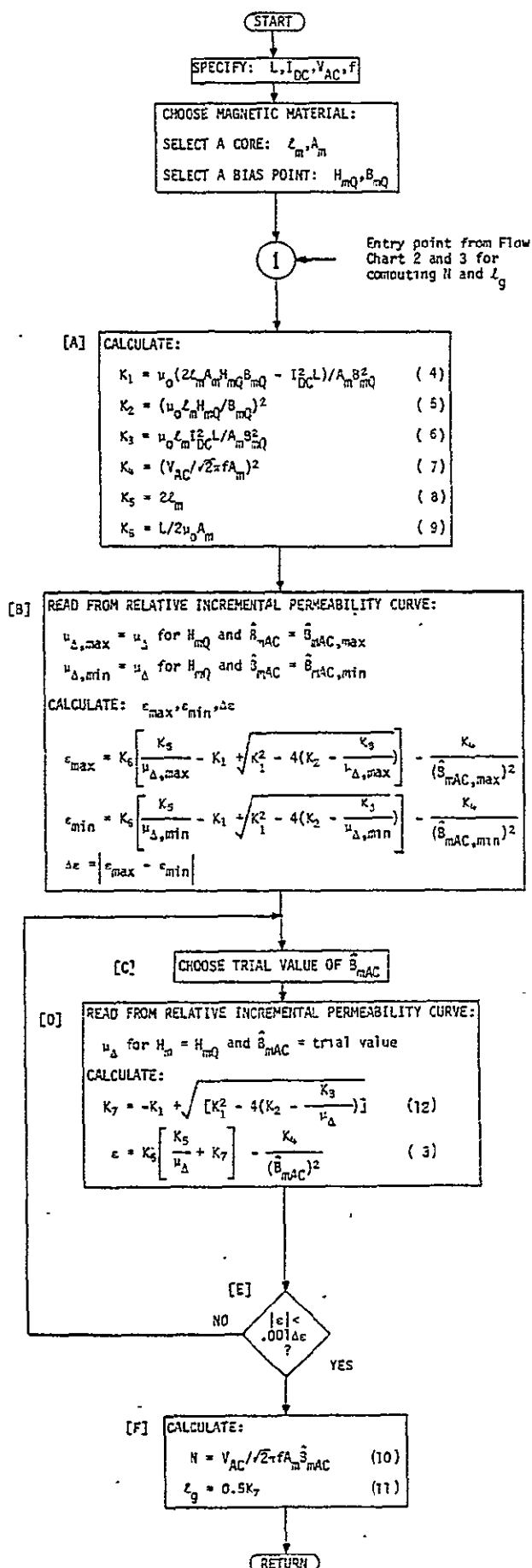
The second chart, Figure 4.5, illustrates a procedure adaptable to computer-aided design techniques, in which a stored library of magnetic and geometric data on commercially available cores is used as the primary data source. This procedure begins by using data for the smallest core in the library and an initial quiescent point (H_{mQ}, B_{mQ}) to calculate N and ℓ_g , using the algorithm in the first chart. The procedure continues by iteratively selecting additional quiescent points and re-computing N and ℓ_g , until a minimum value for the number of turns N is found, along with a

physically-realizable air-gap length. If the core under examination is incapable of functioning to provide the specified requirements, it is discarded and the next larger core is examined.

The third flow chart, Figure 4.7, is used to explain a design procedure which does not produce a minimum-turns design, but incorporates a core screening function which enables a designer to choose suitable cores and to design an inductor for a specified quiescent point, using the computational capability of an electronic pocket calculator. The screening operation involves a relatively simple computation which indicates cores for which a physically-realizable air-gap is possible.

4.4.1 Flow Chart 1.

Returning to the first flow chart in Figure 4.4, a closer study of the algorithm for determining N and ℓ_g is made. The operations in this chart begin with the assignment of the specification requirements of L , I_{DC} , V_{AC} and f and the choosing of a magnetic core material and geometry and a quiescent operating point (H_{mQ}, B_{mQ}). These steps carry the procedure to an entry point designated by the number 1 enclosed by a circle. This entry point, Node 1, is used by the design procedures illustrated by the two remaining flow charts, where the algorithm which follows Node 1 returns to these procedures values of N and ℓ_g . Since the values of H_{mQ} and B_{mQ} are assigned before entering Node 1, parameters K_1 through K_6 are calculated in Step [A] and treated as constants until another core and/or quiescent point is selected. The algorithm for finding N and ℓ_g depends on obtaining a solution set for μ_Δ and \hat{B}_{mAC} by an iterative evaluation of $F_1(\cdot)$ to produce a computed error ϵ by using trial values of \hat{B}_{mAC} and the corresponding values

Figure 4.4. Flow Chart 1: Algorithm for computing N and l_g .

of μ_{Δ} , which are read from the incremental permeability curve for the selected value of H_{mQ} .

To provide guidance on the magnitude of ϵ representing a good engineering solution, a range factor $\Delta\epsilon$ is calculated as the magnitude of the difference between extreme values, ϵ_{\max} and ϵ_{\min} in Step [B]. The defining relationships for ϵ_{\max} and ϵ_{\min} are shown in the flow chart. Using the range factor $\Delta\epsilon$ and the precision factor of 0.001, the computation of the error factor ϵ proceeds in a closed loop using Steps [C], [D], and [E] until the solutions for \hat{B}_{mAc} and μ_{Δ} converge to within the permitted error bound. Once the solution set is found, the values of N and l_g are computed in Step [F] and the design for the specified requirements of chosen core material and geometry and the selected quiescent operating point is completed.

4.4.2 Flow Chart 2.

In the procedure illustrated in the flow chart in Figure 4.5, an optimization algorithm searches for the combination of quiescent point and air-gap length which yields a minimum value for the number of turns N on the reactor. Because no general mathematical model is available which will fit the wide variety of magnetic materials in use, purely analytical optimization techniques cannot be applied. However, by the use of an iterative procedure which employs multiply-dimensioned polynomial fits to experimentally obtained data, an optimized quiescent operating point and air-gap length can be determined.

The algorithm in this flow chart operates on a base of data for commercially available air-gap cores such as the type C geometry. The data base includes core dimensions and sample points taken from the normal magnetization curve and from a family of relative incremental permeability

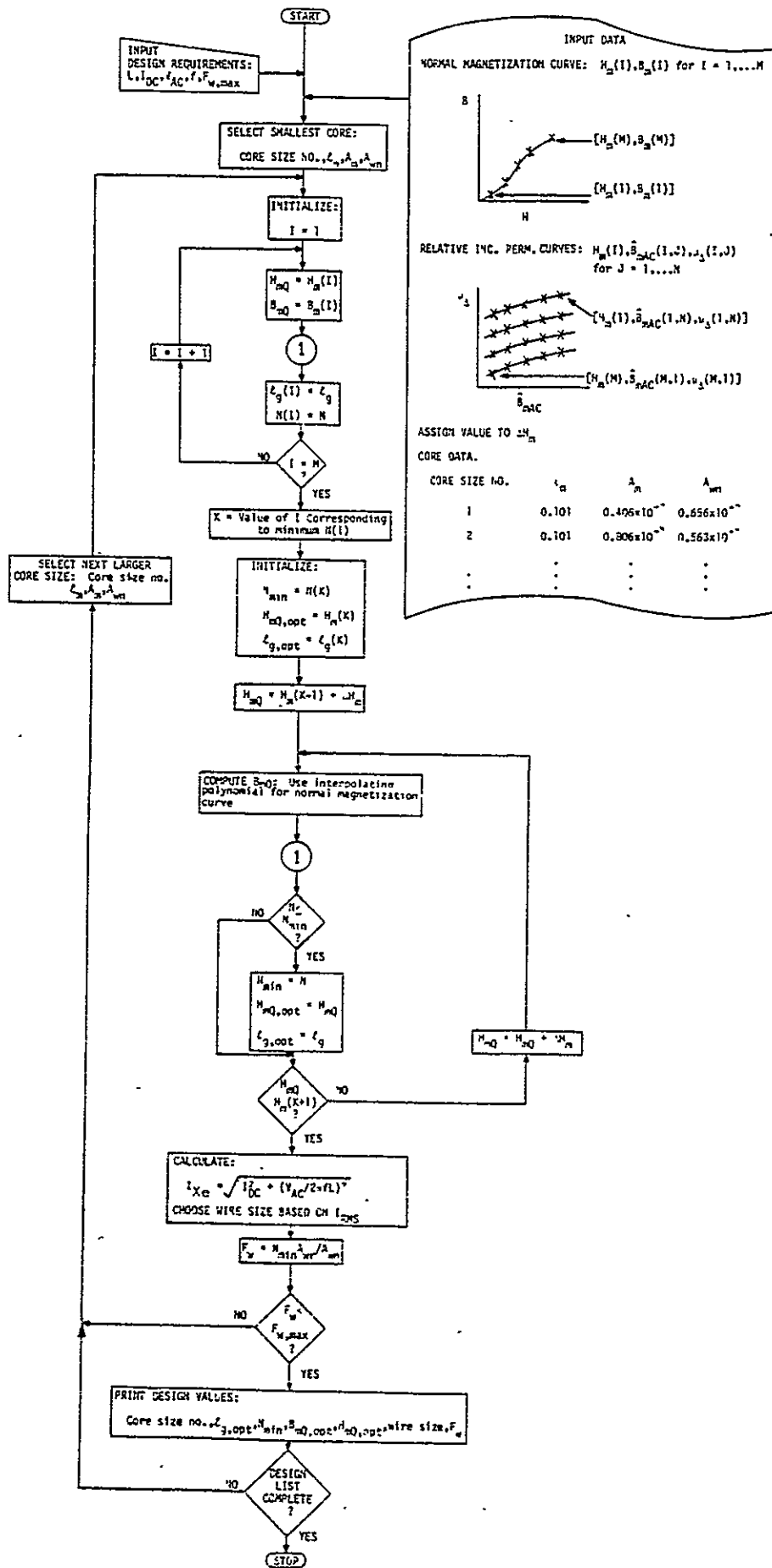


Figure 4.5. Flow Chart 2: Algorithm for optimized inductor design

curves for the designated core material. For each sample point $[H_m(I), B_m(I)]$ selected as a data-base point on the normal magnetization curve, there is a corresponding member of the family of relative incremental permeability curves which also is stored as a set of sample points $[H_m(I), \hat{B}_{mAC}(I, J), \mu_\Delta(I, J)]$.

Starting with the smallest core in the data library and the first sample point $[H_m(1), B_m(1)]$ on the normal magnetization curve, polynomial interpolation is used to approximate intermediate values of μ_Δ on the corresponding incremental permeability curve $[H_m(1), \hat{B}_{mAC}(1, J), \mu_\Delta(1, J)]$ when seeking the solution value \hat{B}_{mAC} in steps [C]-[D]-[E] of Flow Chart 1 the first time that this sub-program, marked by the circled number 1, is encountered near the top of Flow Chart 2 in Figure 4.5. The value of turns N and air-gap length l_g are thus determined for this first sample point. This procedure is repeated for each of the M sample points on the normal magnetization curve.

The particular sample-value quiescent point $[H_m(K), B_m(K)]$ corresponding to the smallest calculated value for turns N is used as the starting point for another interpolation routine. This interpolation procedure is used in a search for that particular intermediate value of quiescent point on the normal magnetization curve which produces the minimum number of turns N . The interval searched spans the range covered by this starting sample point and the two adjacent sample points. For each intermediate trial value of quiescent point H_{mQ} , polynomial interpolation is used to approximate the corresponding value of B_{mQ} on the normal magnetization curve when preparing to compute the design constants K_1 to K_6 in Step [A] of Flow Chart 1 when the sub-algorithm marked Node 1 is encountered near the center of the flow chart in Figure 4.5. The interpolating scheme for obtaining

the values of $\mu_{\Delta, \max}$ and $\mu_{\Delta, \min}$ and the value of μ_{Δ} corresponding to the trial \hat{B}_{mAC} , which are used in Steps [B]-[C]-[D]-[E] in Flow Chart 1, is described with reference to Figure 4.5. The interpolation routine makes use of Lagrange's interpolating polynomial of sixth degree [23]. The data points used in establishing the required polynomials correspond in all cases to the six points closest to the most recently established trial point. Points marked by crosses on the relative incremental permeability curves shown in Figure 4.6 represent the sample points stored as a part of the data base. The six relative incremental permeability curves corresponding to the six sample points on the normal magnetization curve which are closest to the trial quiescent point magnetizing force H_{mQ} are used for interpolation. The values of $\mu_{\Delta, \max}$ and $\mu_{\Delta, \min}$ for intermediate trial values of H_{mQ} are approximated by interpolation using, respectively, the six data points, illustrated in Figure 4.6 by circles surrounding the crosses, which correspond to the sample point values of μ_{Δ} for $\hat{B}_{mAC, \max}$ and $\hat{B}_{mAC, \min}$ on the six closest relative incremental permeability curves. To obtain a value of μ_{Δ} corresponding to the trial value of \hat{B}_{mAC} , indicated in Figure 4.6 as $\hat{B}_{mAC, \text{trial}}$ and needed in Step [D] of Flow Chart 1, two interpolations are used. The first interpolation provides values of μ_{Δ} corresponding to $\hat{B}_{mAC, \text{trial}}$ for each of these six closest incremental permeability curves. The location of the points corresponding to these six values of μ_{Δ} are shown as circles in Figure 4.6. These μ_{Δ} values are then used as six data points in a second interpolation to find an approximate value of μ_{Δ} corresponding to the trial quiescent point H_{mQ} and $\hat{B}_{mAC, \text{trial}}$. This procedure of two interpolations is repeated until a solution value of \hat{B}_{mAC} is obtained in Steps [C]-[D]-[E] in Flow Chart 1. The values N and ϵ_g corresponding to this trial quiescent

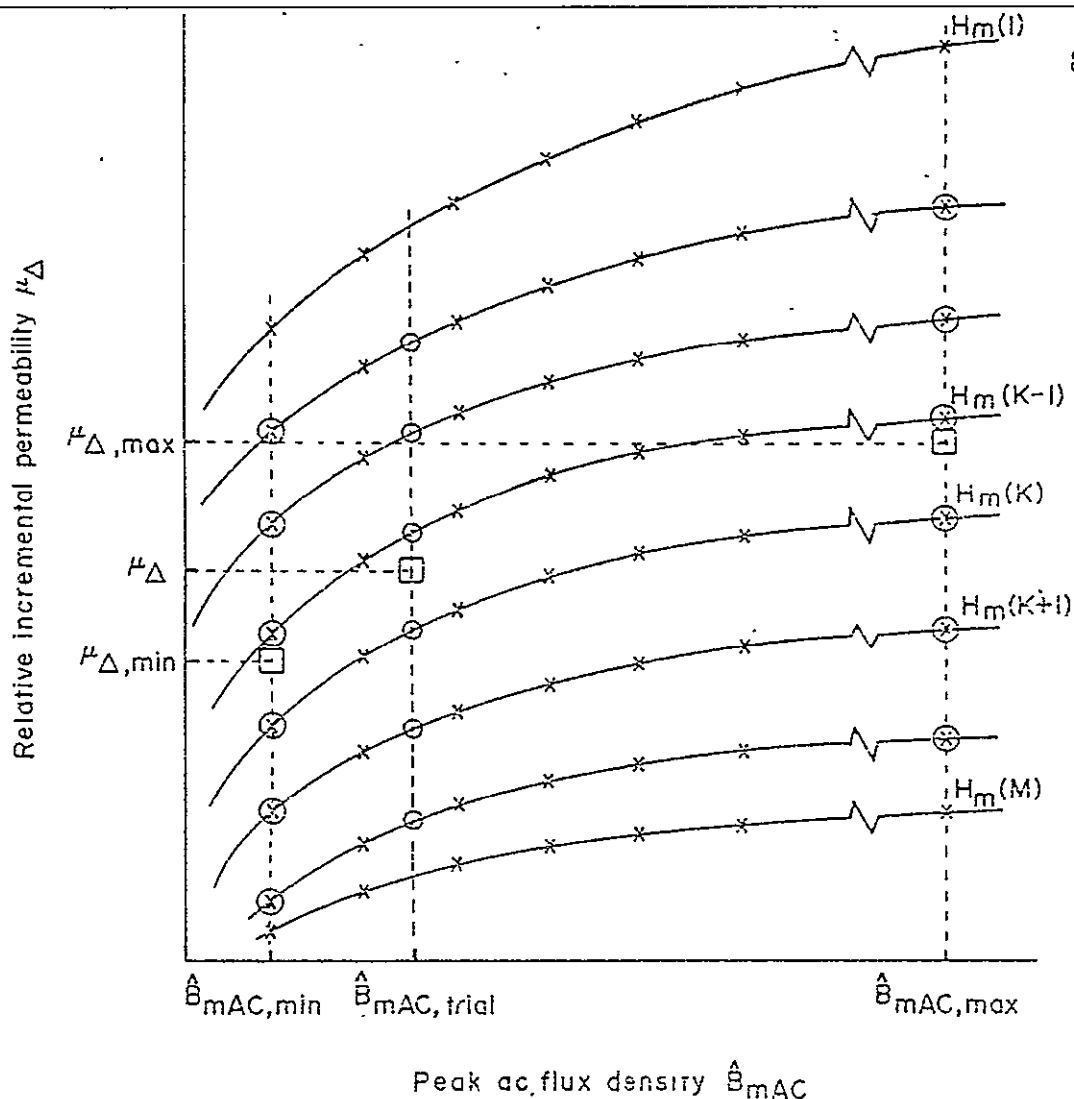


Figure 4.6 Illustration of use of data-base points to calculate $\mu_{\Delta,\min}$ and $\mu_{\Delta,\max}$ for a trial value of H_{m0} lying between $H_m(K-1)$ and $H_m(K)$. Also, illustration of the two iterations used to obtain a value of μ_{Δ} for an arbitrary trial H_{m0} and $\hat{B}_{mAC,trial}$.

x Experimentally-determined incremental-permeability data points stored as a part of the data base.

○ Values of μ_{Δ} for $\hat{B}_{mAC,trial}$ obtained by interpolation for the six values of H_m in the data base closest to the trial value of H_{m0} .

⊗ Six data-base points nearest to the trial value of H_{m0} used to calculate $\mu_{\Delta,\min}$ corresponding to $\hat{B}_{mAC,min}$, and six points used to calculate $\mu_{\Delta,\max}$ corresponding to $\hat{B}_{mAC,max}$.

□ Values of $\mu_{\Delta,\min}$, $\mu_{\Delta,\max}$, and the trial value of μ_{Δ} obtained by interpolation using the ⊗ and ○ values.

ORIGINAL PAGE IS
OF POOR QUALITY

point are computed and N is compared with the lowest previously calculated number of turns. This trial quiescent value H_{mQ} is then incremented by a prescribed amount ΔH_m and the procedure described above is repeated.

After the minimum value for N and its associated air-gap are found for a selected core, the maximum rms winding current is computed, a wire size is chosen, and the winding factor is computed. If the core is windable, the pertinent information on core size number, minimum turns N_{min} , air-gap for the optimum design $\ell_{g,opt}$, quiescent operating point $(H_{mQ,opt}, B_{mQ,opt})$, wire size and winding factor F_w are printed. If the core is not windable, or if it is desired to obtain a design for a larger core, the next larger core size is selected and the procedure performs another set of computations to obtain a possible design.

4.4.3 Flow Chart 3.

The third flow chart, presented in Figure 4.7, shows a procedure which may be employed to design an air-gapped magnetic-core inductor, using the computational capability of an electronic pocket calculator. This procedure does not produce an optimized design with minimum turns for a given core and set of specifications. However, by means of a relatively simple screening process, the procedure does permit a designer to determine which cores among those available to him are capable of yielding designs with physically realizable air-gaps. Cores which pass this screening process then may be considered further by using the algorithm for determining N and ℓ_g flow charted in Figure 4.4.

The design procedure begins with the specification of the design requirements in Step [G] and the selection of a candidate magnetic core

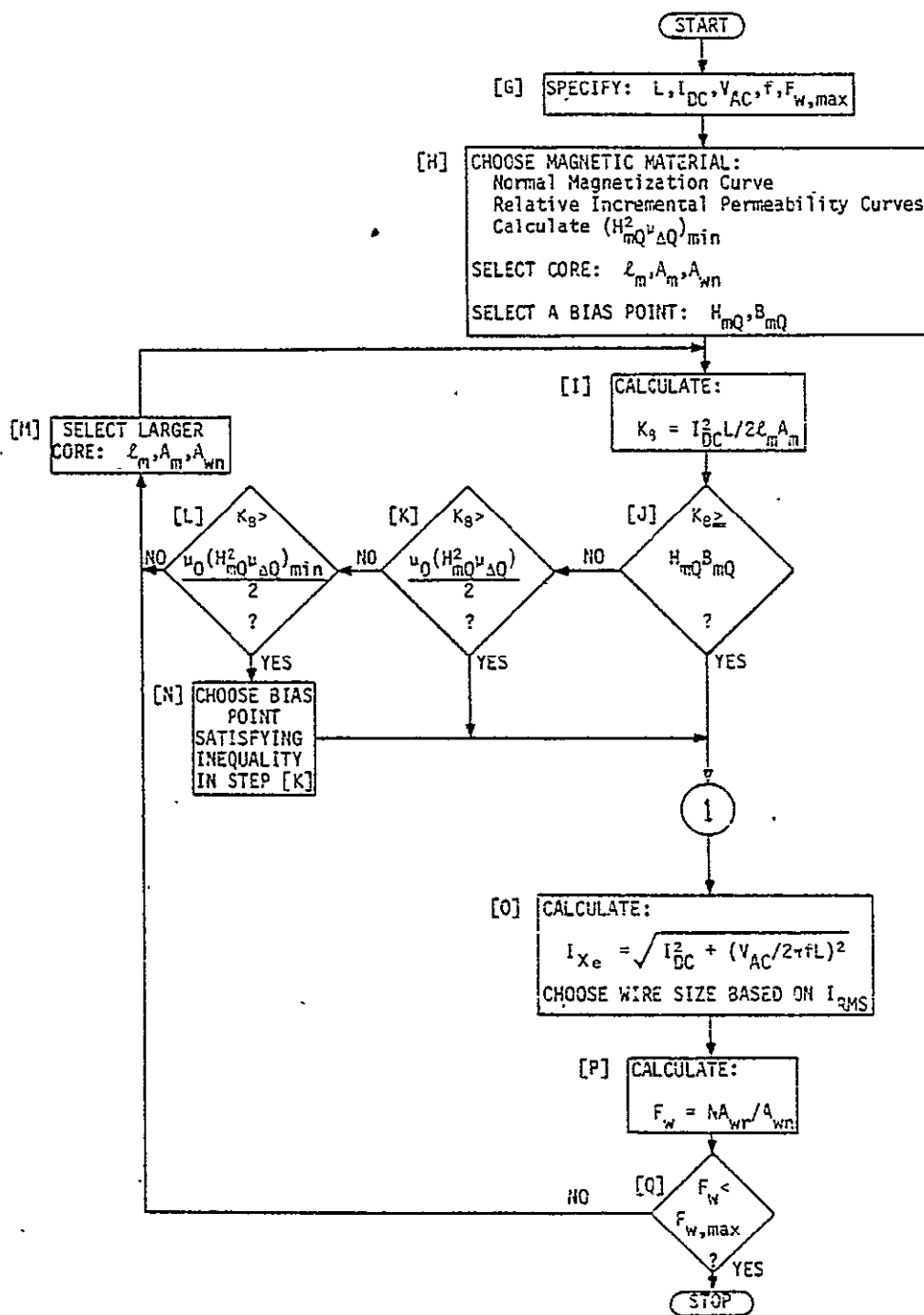


Figure 4.7. Flow Chart 3: Algorithm for Screening Cores for Physically Realizable Air-Gap.

material, calculation of a parameter $(H_{mQ}^2 \mu_{\Delta Q})_{\min}$, the selection of a core geometry and choice of quiescent operating point (H_{mQ}, B_{mQ}) as indicated in Step [H]. The screening rule, which is developed in Appendix F, depends on decisions made on inequality expressions involving a constant K_8 which is a function of certain of the design specifications and of the core geometry. In Step [J], if K_8 is greater than $H_{mQ} B_{mQ}$, the design equations will yield a workable core and N and ℓ_g are computed as indicated by the branching to Node 1, which represents the entry point to the N and ℓ_g algorithm of Flow Chart 1. If this K_8 inequality relation proves to be false, then K_8 is tested in Step [K] to determine if it is greater than $\mu_0(H_{mQ}^2 \mu_{\Delta Q})/2$, where $\mu_{\Delta Q}$ is the maximum value of μ_{Δ} on the relative incremental permeability curve corresponding to the selected quiescent point. A true condition of this inequality again leads to the computation of N and ℓ_g . The false condition leads to a final check on the value of K_8 in Step [L] where it is compared to the parameter $\mu_0(H_{mQ}^2 \mu_{\Delta Q})_{\min}/2$. The latter parameter is unique to the particular magnetic material chosen and is the minimum value of $\mu_0(H_{mQ}^2 \mu_{\Delta Q})/2$ over the range of H_{mQ} and $\mu_{\Delta Q}$ for which data are available. If the value of K_8 is greater than the value of parameter $\mu_0(H_{mQ}^2 \mu_{\Delta Q})_{\min}/2$, the core will permit a design with a physically realizable air-gap if a new quiescent or bias point is chosen in Step [N] which satisfies the inequality in Step [K]. If the inequality in the third decision inequality is not satisfied, then a larger core must be selected in Step [M] and the process repeated.

When a combination of core geometry and quiescent operating point is found which leads to values of N and ℓ_g , the rms winding current is determined in Step [O] and a wire size is chosen according to the current density

constraint imposed by the designer. The winding factor then is computed in Step [P] and if the winding factor is acceptable, Step [Q], the design is completed. If the core is not windable, a larger core is selected and the screening process is re-entered.

4.5 Example to Illustrate Design Procedures

To illustrate the design procedures previously described, a sample design for a filter inductor is presented in outline form. The procedure which is illustrated in some detail is that shown in Flow Charts 1 and 3, Figures 4.4 and 4.7, and is suited to the use of an electronic pocket calculator on which the computations shown were made.

Flow Chart 3.

[G] Specifications: $L = 0.5 \text{ H}$; $I_{DC} = 0.15 \text{ A}$; $V_{AC} = 1.0 \text{ V}$; $f = 60 \text{ Hz}$;
 $F_{w,max} = 0.4$

[H](i) Choose magnetic material:

Grain-oriented 3 percent silicon steel

Normal magnetization curve (Figure 4.2, Curve 2)

Relative incremental permeability curves (Figure 4.3)

Calculate $(H_{mQ}^2 \mu_{\Delta Q})_{min}$: From extreme left end of upper curve
 in Figure 4.3, $(0.1 \times 79.577)^2 (2800) = 1.77 \times 10^5 (\text{A/m})$

(ii) Select Core:

$$\ell_m = 0.120015 \text{ m}; A_m = 1.613 \times 10^{-4} \text{ m}^2; A_{wn} = 4.838 \times 10^{-4} \text{ m}^2$$

(iii) Select a bias point:

A bias point is arbitrarily assigned by the designer. Choice of a bias point in the knee region of the normal magnetization curve usually has been found to lead to workable designs. Choose

$$H_{mQ} = 31.83 \text{ A/m (0.4 oersted)}; B_{mQ} = 1.2 \text{ T (12.0 kilogausses)}$$

$$H_{mQ} B_{mQ} = 38.196.$$

[I] Calculate K_8 : $K_8 = 2.9072 \times 10^2$

[J] $K_8 > H_{mQ} B_{mQ}$; go to Node 1, the entry point for the algorithm for calculating N and ϵ_g . Since $K_8 > H_{mQ} B_{mQ}$, steps [K] and [L] are not used.

Flow Chart 1

[A] Calculate $K_1, K_2, K_3, K_4, K_5, K_6$:

$$K_1 = -5.2863 \times 10^{-5}$$

$$K_2 = 1.6003 \times 10^{-11}$$

$$K_3 = 7.3047 \times 10^{-6}$$

$$K_4 = 5.409 \times 10^2$$

$$K_5 = 0.24003$$

$$K_6 = 1.2334 \times 10^9$$

[B] Read from relative incremental permeability curve.

For $H_{mQ} = 31.83 \text{ A/m}$ (0.4 oersteds)

$$\mu_{\Delta, \max} = 6200$$

$$\text{at } \hat{B}_{mAC, \max} = 1.4 \text{ T}$$

$$\mu_{\Delta, \min} = 700$$

$$\text{at } \hat{B}_{mAC, \min} = -0.02 \text{ T}$$

Calculate: $\epsilon_{\max}, \epsilon_{\min}, \Delta\epsilon$

$$\epsilon_{\max} = 2.1908 \times 10^5$$

$$\epsilon_{\min} = -6.039 \times 10^5$$

$$\Delta\epsilon = 8.2305 \times 10^5$$

[C] Choose trial value of \hat{B}_{mAC} :

Trial No.	\hat{B}_{mAC} in T	Next Step
1	0.04	Go to [D], trial no. 1
2	0.03	Go to [D], trial no. 2
3	0.0279	Go to [D], trial no. 3
4	0.02807	Go to [D], trial no. 4

- [D] Read value of μ_{Δ} from relative incremental permeability curve corresponding to $H_{mQ} = 31.83$ A/m and value of \hat{B}_{mAC} from [C]; calculate K_7 and ϵ :

Trial No.	μ_{Δ}	K_7	ϵ	Next Step
1	880	2.4242×10^{-4}	2.9737×10^5	Go to [E], trial no. 1
2	800	2.5098×10^{-4}	7.8649×10^4	Go to [E], trial no. 2
3	785	2.5275×10^{-4}	-5.9982×10^3	Go to [E], trial no. 3
4	790	2.5215×10^{-4}	-7.3500×10^2	Go to [E], trial no. 4

- [E] Test value of $|\epsilon|$ against precision range-factor
 $0.001\Delta\epsilon = 8.2305 \times 10^2$:

Trial No.		Next Step
1	$ \epsilon = 2.9737 \times 10^5 > 8.2305 \times 10^2$	Go to [C], trial no. 2
2	$ \epsilon = 7.8649 \times 10^4 > 8.2305 \times 10^2$	Go to [C], trial no. 3
3	$ \epsilon = 5.9982 \times 10^3 > 8.2305 \times 10^2$	Go to [C], trial no. 4
4	$ \epsilon = 7.3500 \times 10^2 < 8.2305 \times 10^2$	Go to [F]

- [F] Calculate N and ℓ_g :

$$N = 828 \text{ turns}$$

$$\ell_g = 1.261 \times 10^{-4} \text{ m}$$

Return to Flow Chart 3, step [0]

Flow Chart 3

- [0] Calculate $I_{\chi e}$ and choose wire size:

$$I_{\chi e} = 0.150211 \text{ A}$$

Using a current density of $5.0671 \times 10^{-7} \text{ m}^2/\text{A}$ (1000 circular mils/A), wire size AWG 28 is satisfactory.

[P] Calculate windability:

For AWG 28 with heavy Formvar insulation, the total area of the wire and insulation $A_{wr} = 1.051 \times 10^{-7} \text{ m}^2$ (207 circular mils); $F_w = 0.18$.
Selected core is windable and design is completed.

The design example illustrated is not an optimized design, in the sense of minimization of turns. Using the same magnetic core material data and core dimensions, the following results were obtained from a computer program which implements the optimization algorithm described earlier in Flow Chart 2 of Figure 4.5. The results of the nonoptimized design results are recapitulated for comparison.

	<u>Optimized Design</u>	<u>Nonoptimized Design</u>
N	738	828
ℓ_g	$1.156 \times 10^{-4} \text{ m}$	$1.261 \times 10^{-4} \text{ m}$
H_{mQ}	30.24 A/m (0.38 oersted)	31.83 A/m (0.4 oersted)

4.6 Conclusions

The design procedures presented in this chapter are particularly useful in the case of filter inductors for electronic power supplies where the winding usually must carry a large direct current in addition to presenting a high reactance to the fundamental component of the alternating current. By incorporating into the procedures experimentally determined relative incremental permeability curves, the large ac flux excursions normally encountered in such applications can be taken into account. In the computer-aided design procedure, an important feature is the optimization algorithm for determining the quiescent operating point and air-gap length yielding the minimum number of turns. An easily used screening process which permits a designer

to identify candidate cores for which a physically realizable air-gap is possible and a relatively simple procedure for solving for the incremental permeability and ac flux density excursion using an electronic pocket calculator are provided in the second procedure.

CHAPTER V

DESIGN OF AIR-GAPPED INDUCTORS USING SPECIALLY PREPARED MAGNETIC CORE DATA

5.1 Introduction

In Chapter IV it was mentioned that Hanna's method provides a direct and easily used procedure for the design of air-gapped inductors by using specially prepared magnetic core data [16]. Hanna's method, however, is limited to the design of inductors with small ac flux excursions. The method uses specially prepared magnetic core curves which unfortunately are not available for some of the modern core materials.

This chapter presents a direct calculation procedure for the design of air-gapped inductors with large ac flux excursions. The heart of the new design procedure depends on the development of specially prepared magnetic core data calculated from core material data which are available from core manufacturers. Using the results of the analysis in Chapter IV, and following the pattern of Hanna's development, a set of design curves is generated. These curves make use of a family of relative incremental permeability curves and thus allow large ac flux excursions to be taken into account. For a selected core, by using these curves a designer can find the length of the air gap ℓ_g and the number of turns N for the winding to meet the design requirements given in Chapter IV.

Using the results of the analysis of a magnetic circuit with an air gap presented in Chapter IV, the design relationships are developed. Following a discussion of the generation of design curves with the help of a digital computer, an example is given to illustrate the design procedure. The procedure for generating the design curves is presented in detail in flow chart form in Appendix H. Toward the end of the chapter a comparison is made between Hanna's curves and the design curves presented in this chapter for corresponding cases of small values of ac flux excursions.

5.2 Design Relationships Used in Generating Hanna's Curves

The design relationships used in Hanna's method, given by (5) and (6) in Ref. [16], are repeated here as (5.1) and (5.2)

$$\frac{LI_{DC}^2}{v} = \frac{B_{mQ}^2 \left[\frac{1}{\mu_{DC}} + \frac{\ell_g}{\ell_m} \right]^2 \times 10^{-8}}{0.4\pi \left(\frac{1}{\mu_{\Delta}} + \frac{\ell_g}{\ell_m} \right)} \quad (5.1)$$

$$\frac{NI_{DC}}{\ell_m} = \frac{B_{mQ}}{0.4\pi \left[\frac{1}{\mu_{DC}} + \frac{\ell_g}{\ell_m} \right]} \quad (5.2)$$

where $v = \ell_m A_m$ is defined as the magnetic core volume. When these equations are written in SI units, using $B_{mQ} = \mu_0 \mu_{DC} H_{mQ}$, they take on the form:

$$\frac{LI_{DC}^2}{v} = \frac{[\mu_0 H_{mQ} + \frac{\ell_g}{\ell_m} B_{mQ}]^2}{\mu_0 \left[\frac{1}{\mu_{\Delta}} + \frac{\ell_g}{\ell_m} \right]} \quad (5.3)$$

$$\frac{NI_{DC}}{\ell_m} = \frac{[\mu_0 H_{mQ} + \frac{\ell_g}{\ell_m} B_{mQ}]}{\mu_0} \quad (5.4)$$

Rearranging (5.3) and (5.4) leads to

$$\frac{LI_{DC}^2}{v} = \mu_0 \frac{\mu_\Delta}{1 + \mu_\Delta \frac{\ell_g}{\ell_m}} \left(\frac{\ell_g}{\ell_m} \frac{B_{mQ}}{\mu_0} + H_{mQ} \right)^2 \quad (5.5)$$

$$\frac{NI_{DC}}{\ell_m} = \frac{\ell_g}{\ell_m} \frac{B_{mQ}}{\mu_0} + H_{mQ} \quad (5.6)$$

The values for the relative incremental permeability μ_Δ used in (5.5) by Hanna are for very small values of ac flux excursions and thus depend only on the dc operating point H_{mQ} on the normal magnetization curve. A typical curve of μ_Δ versus H_{mQ} for 3-percent grain-oriented silicon steel for very small ac flux excursions, obtained from References [21] and [22], is shown in Figure 5.1. Using data from such a curve and from the associated normal magnetization curve, such as shown in Figure 4.2, Chapter IV, for an assigned value of air-gap ratio ℓ_g/ℓ_m , equations (5.5) and (5.6) are treated as parametric equations with H_{mQ} as the parameter, to obtain a curve of LI_{DC}^2/v versus NI_{DC}/ℓ_m . For a given value of air-gap ratio, several values of H_{mQ} are assigned and the corresponding values of μ_Δ and B_{mQ} are used in (5.5) and (5.6) to determine the associated values of LI_{DC}^2/v and NI_{DC}/ℓ_m . A plot of these two quantities for various values of air-gap ratio is known as a set of Hanna's curves, and is illustrated for 3-percent grain-oriented steel, Permalloy 80, and Supermendur in Figures 5.2, 5.3, and 5.4, respectively.

Using Hanna's curves, an inductor can be designed to meet the requirements of specified inductance L , and dc current I_{DC} in the winding. For the selected core, the value of LI_{DC}^2/v is determined using the specified values of L and I_{DC} , and the known volume v of the chosen core. The corresponding value of air-gap ratio ℓ_g/ℓ_m and NI_{DC}/ℓ_m are determined from the

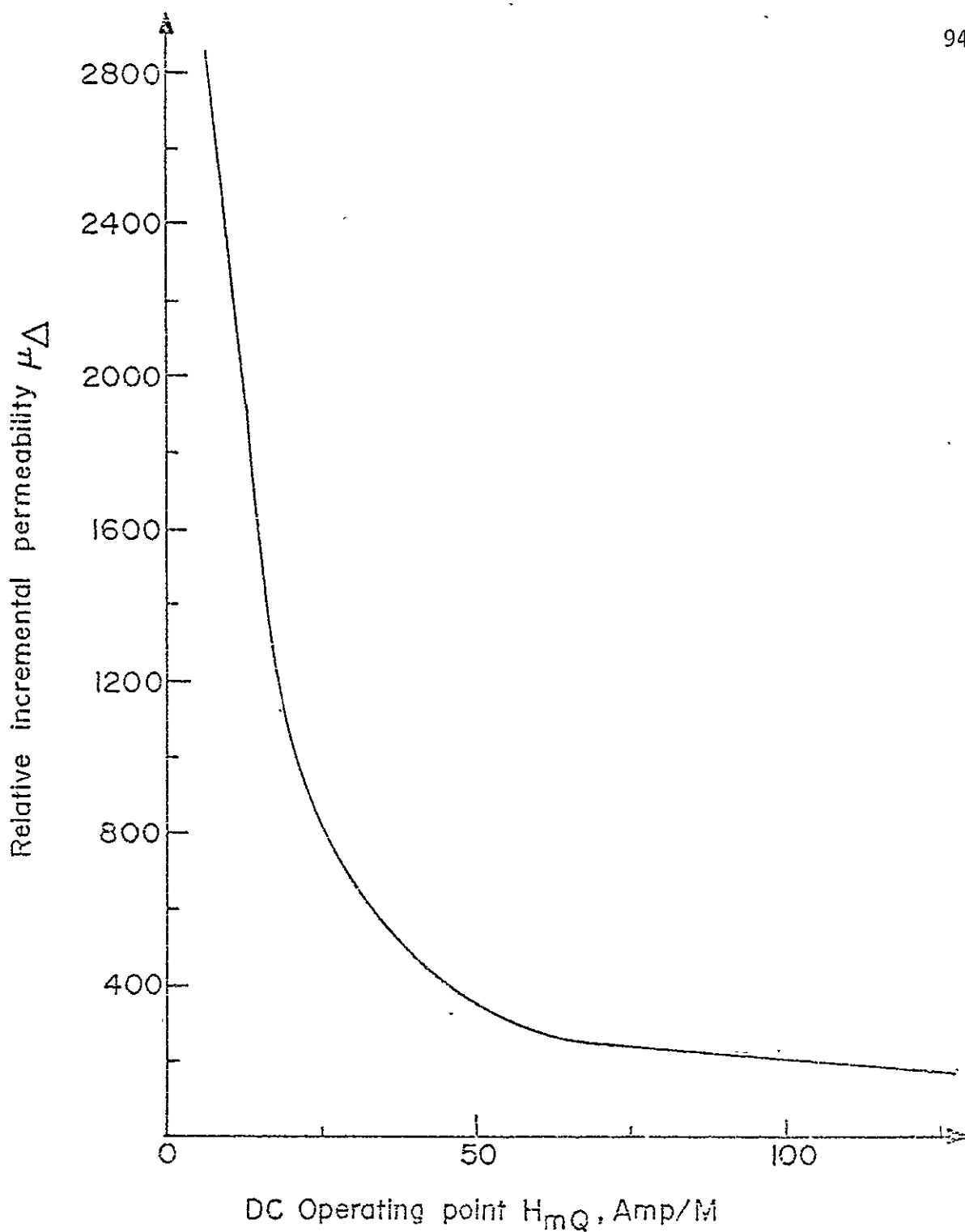


Figure 5.1. Relative incremental permeability versus dc operating point H_{mQ} on normal magnetization curve for small values of ac flux excursions for 3-percent grain-oriented silicon steel.

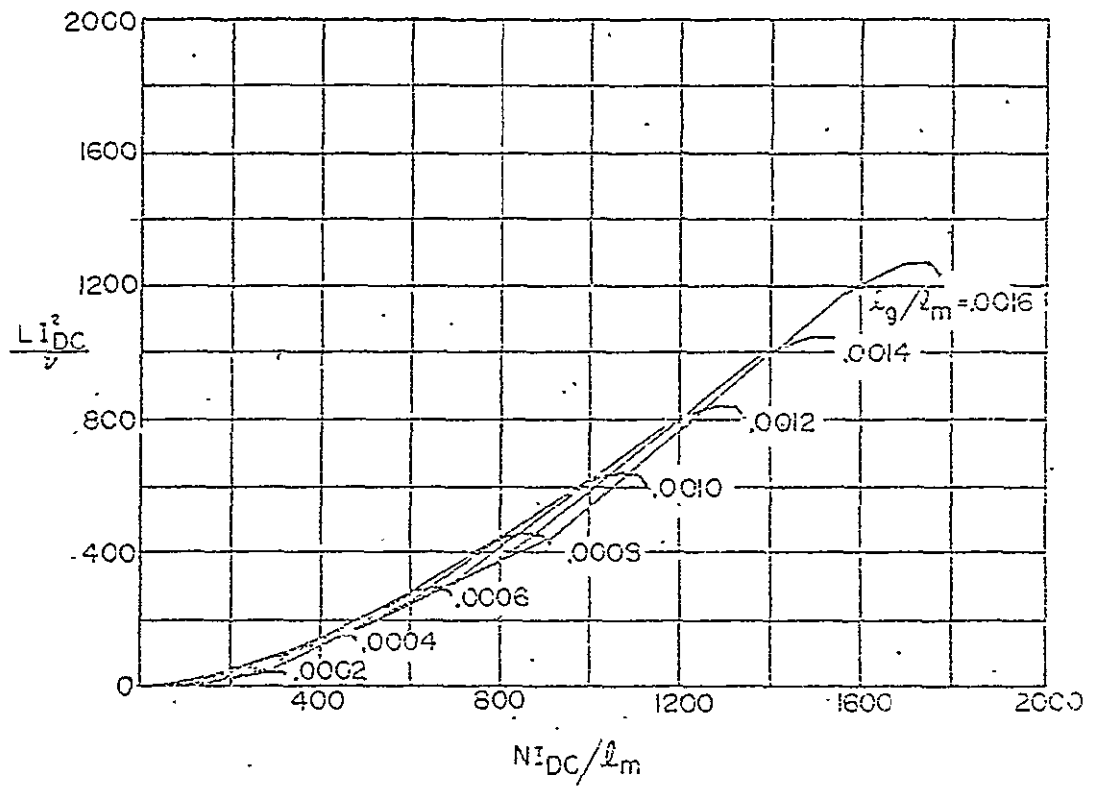


Figure 5.2. Example of Hanna's curves generated by computer program for 3-percent grain-oriented silicon steel.

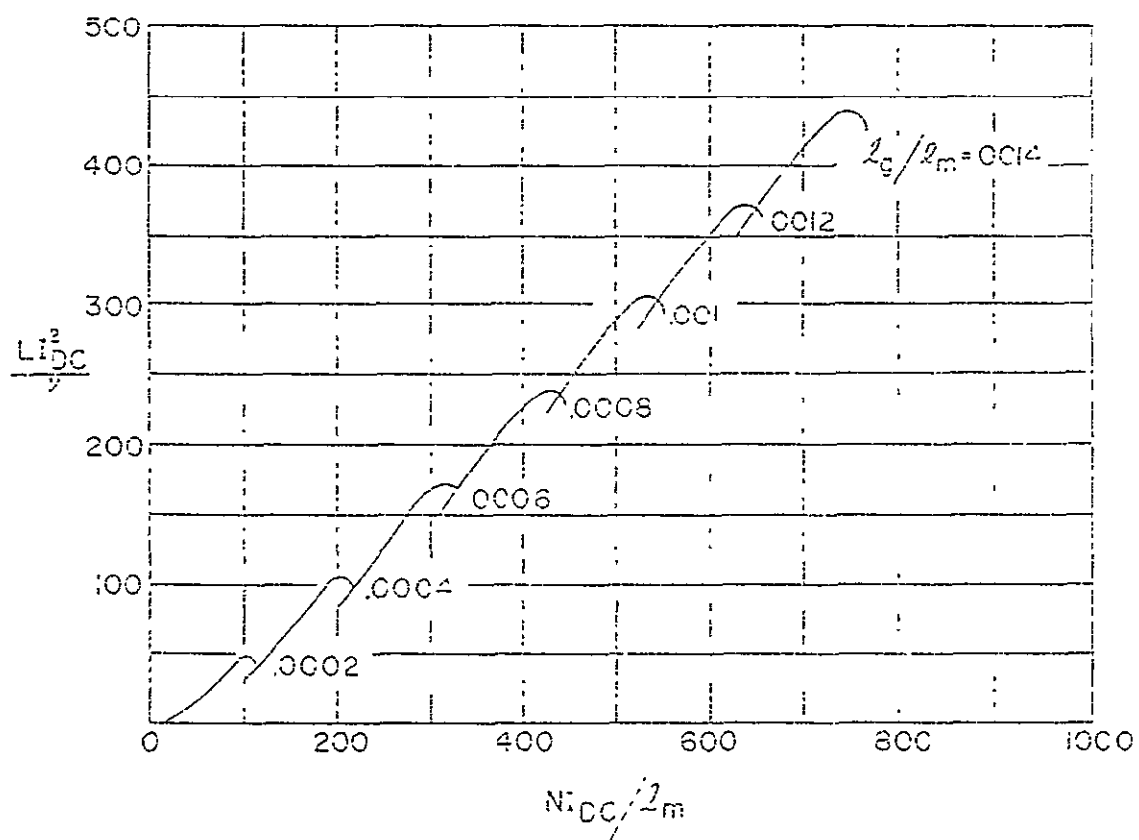


Figure 5.3. Example of Hanna's curves generated by computer program for Permalloy 80.

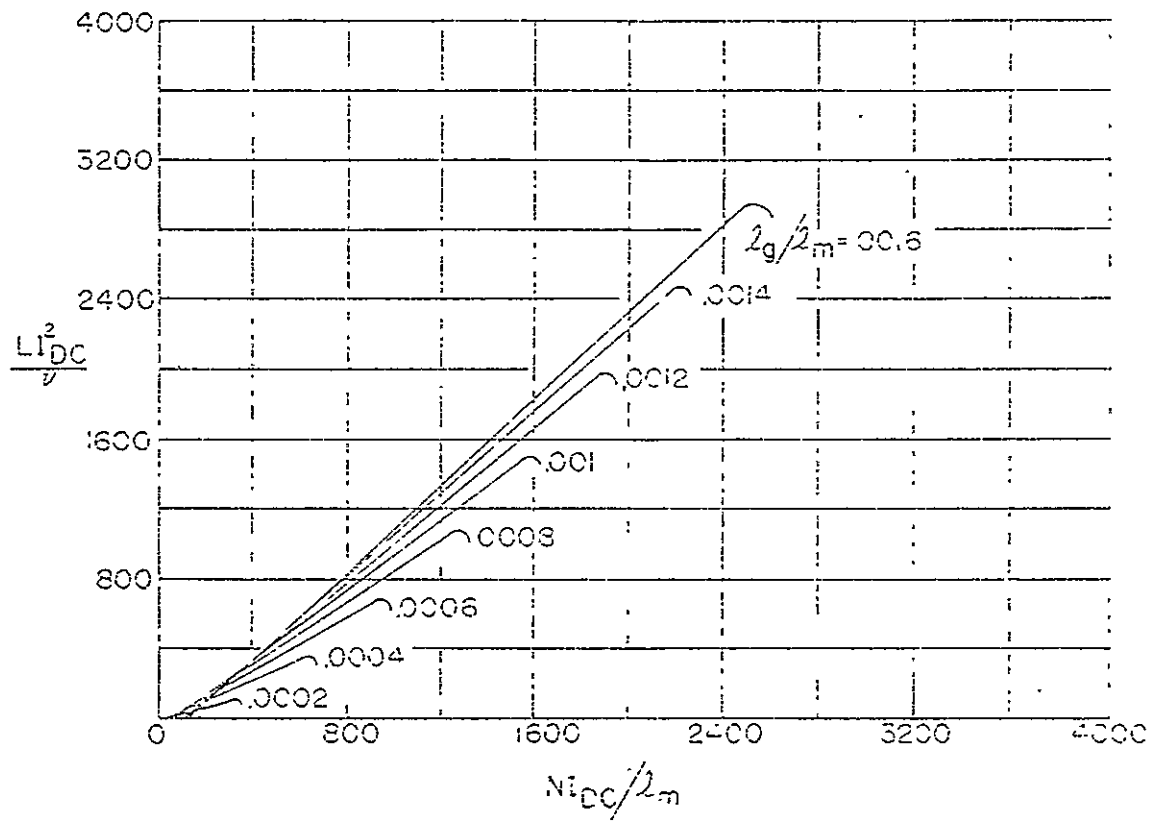


Figure 5.4. Example of Hanna's curves generated by computer program for Supermendur

set of Hanna's curves. The required value of air-gap ℓ_g and turns N are thus determined from the known path length ℓ_m of the selected core, and the specified value of I_{DC} .

In the next section, Hanna's method is extended and design relationships which take large finite ac flux excursions into account are developed.

5.3 Design Relationships when AC Flux Excursions are Large

In this section, a set of design relationships for use in generating design curves is developed. From the analysis of a magnetic circuit with an air gap presented in Chapter IV, the expression for N is given by (E-2) in Appendix E and is repeated here for convenience.

$$N = \frac{\ell_g B_{mQ} + \ell_m \mu_0 H_{mQ}}{\mu_0 I_{DC}} \quad (5.7)$$

Substituting the value of N given by (5.7) into the expression for L given by (4.1) in Chapter IV, the resulting expression becomes

$$L = \mu_0 \frac{\mu_\Delta}{1 + \mu_\Delta \frac{\ell_g}{\ell_m}} \left(\frac{\ell_g B_{mQ} + \ell_m \mu_0 H_{mQ}}{\mu_0 I_{DC}} \right)^2 \frac{A_m}{\ell_m} \quad (5.8)$$

Rearranging (5.8) leads to

$$L = \mu_0 \frac{\mu_\Delta}{1 + \mu_\Delta \frac{\ell_g}{\ell_m}} \left(\frac{\ell_g}{\ell_m} \frac{B_{mQ}}{\mu_0} + H_{mQ} \right)^2 \frac{\ell_m A_m}{I_{DC}^2} \quad (5.9)$$

Recalling the definition of the magnetic core volume $v = \ell_m A_m$ in (5.9) and rearranging leads to the first basic relationship given by (5.10).

$$\frac{L I_{DC}^2}{v} = \mu_0 \frac{\mu_\Delta}{1 + \mu_\Delta \frac{\ell_g}{\ell_m}} \left(\frac{\ell_g}{\ell_m} \frac{B_{mQ}}{\mu_0} + H_{mQ} \right)^2 \quad (5.10)$$

The second basic relationship is obtained from the expression for the alternating voltage across the inductor given by (4.2) in Chapter IV,

$$V_{AC} = \sqrt{2}\pi N f A_m \hat{B}_{mAC} \quad (5.11)$$

Rearranging (5.11) leads to

$$\hat{B}_{mAC} = \frac{V_{AC}}{\sqrt{2}\pi N f A_m} \quad (5.12)$$

The other basic relationships required for the design are obtained from the experimentally determined normal magnetization curve and incremental permeability curves as illustrated, for example, for 3-percent grain-oriented silicon steel in Figure 4.2 and Figure 4.3, respectively. These four relationships, which include equations (5.10) and (5.12) and curves typified by Figures 4.2 and 4.3, contain seven variables $\frac{LI_{DC}^2}{v}$, $\frac{\ell_g}{\ell_m}$, B_{mQ} , H_{mQ} , $\frac{V_{AC}}{\sqrt{2}\pi N f A_m}$, \hat{B}_{mAC} , and μ_Δ . These can be manipulated into a single relationship in terms of the four variables $\frac{LI_{DC}^2}{v}$, $\frac{\ell_g}{\ell_m}$, \hat{B}_{mAC} , and H_{mQ} , which can be symbolically represented by the functional notation

$$\frac{LI_{DC}^2}{v} = g\left(\frac{\ell_g}{\ell_m}, \hat{B}_{mAC}, H_{mQ}\right) \quad (5.13)$$

More particularly, using symbolic functional notation, the value of μ_Δ used in (5.10) is obtained from the family of relative incremental permeability curves where the dependence of μ_Δ upon both the dc operating point H_{mQ} on the normal magnetization curve and upon the peak ac flux excursion \hat{B}_{mAC} can be indicated by use of the symbol $\mu_\Delta(H_{mQ}, \hat{B}_{mAC})$. Similarly, the value of B_{mQ} obtained from the normal magnetization curve as a function of H_{mQ} only can be expressed functionally as $B_{mQ}(H_{mQ})$. Thus, the expression for LI_{DC}^2/v given by (5.10) can be written in a form useful as a design relationship

similar to the one given by (5.13) as

$$\frac{LI_{DC}^2}{v} = \mu_0 \frac{\mu_{\Delta}(H_{mQ}, \hat{B}_{mAC})}{1 + \mu_{\Delta}(H_{mQ}, \hat{B}_{mAC}) \frac{\ell_g}{\ell_m}} \left(\frac{\ell_g}{\ell_m} \frac{B_{mQ}(H_{mQ})}{\mu_0} + H_{mQ} \right)^2 \quad (5.14)$$

which relates the four parameters $\frac{LI_{DC}^2}{v}$, $\frac{\ell_g}{\ell_m}$, \hat{B}_{mAC} , and H_{mQ} .

A second relationship used in the design procedure to be discussed in the next section is obtained by rearranging (5.7) in the form

$$\frac{NI_{DC}}{\ell_m} = \frac{\ell_g}{\ell_m} \frac{B_{mQ}}{\mu_0} + H_{mQ} \quad (5.15)$$

This relationship given by (5.15) is used in computing a design parameter $(\frac{NI_{DC}}{\ell_m})_{opt}$ for the design curves.

For very small values of peak ac flux excursions \hat{B}_{mAC} , the design relationship (5.14) used in the present development reduces to (5.5) used in Hanna's method and the second relationship given by (5.15) is identical to the corresponding (5.6). The design curves which make use of design relationships (5.14) and (5.15) and which take large finite ac flux excursions into account are presented next.

5.4 Design Curves

Families of curves for three different materials, 3-percent grain-oriented silicon steel, Permalloy 80, and Supermendur, which relate design parameters LI_{DC}^2/v and \hat{B}_{mAC} for various values of air-gap ratio ℓ_g/ℓ_m , were generated with the help of a digital computer and are shown in Figures 5.5, 5.6, and 5.7. These families of curves were obtained using magnetic material data in the form of the normal magnetization curve and the family of

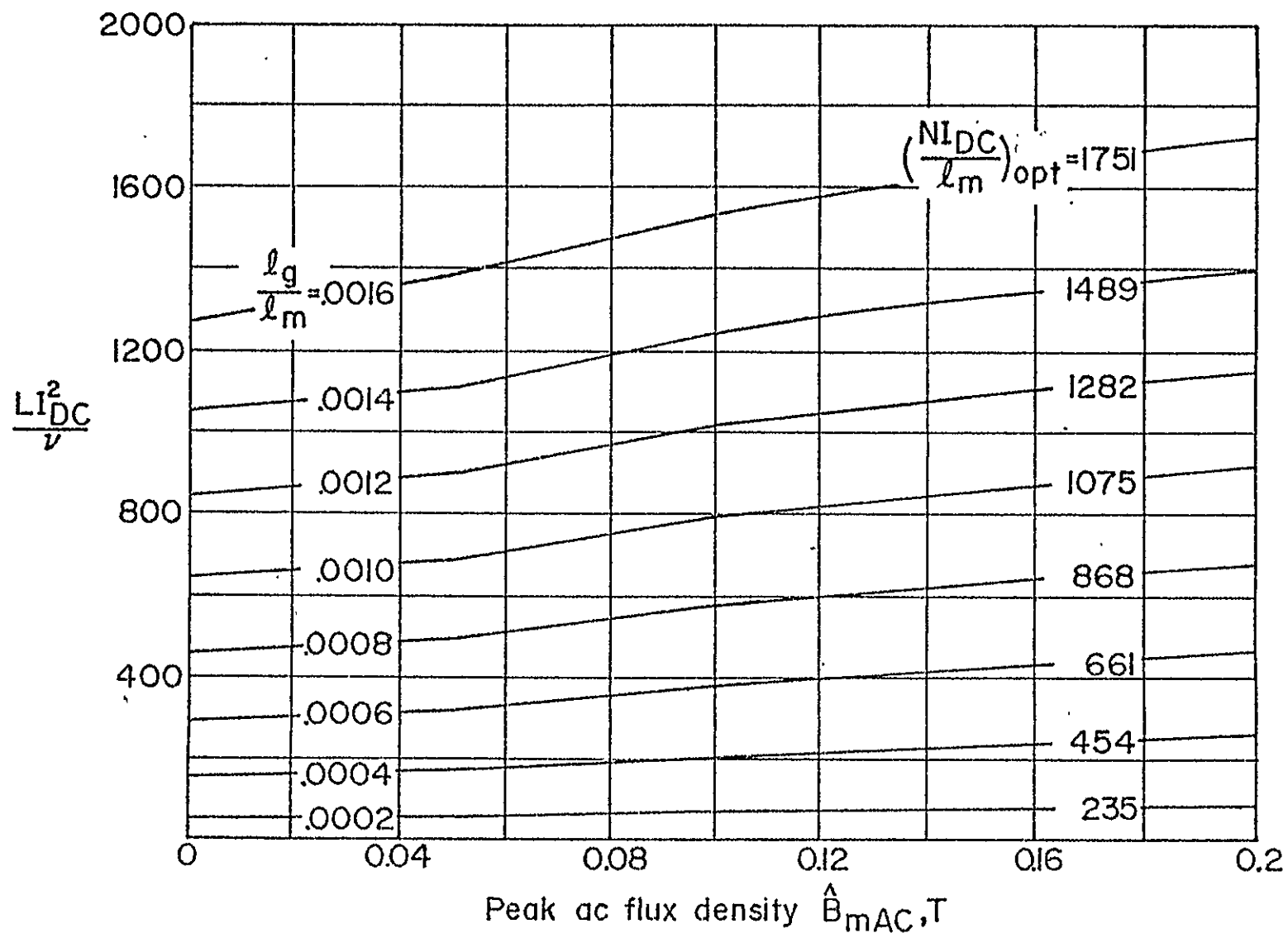


Figure 5.5. Design curves for 3-percent grain-oriented silicon steel which take finite ac flux excursions into account.

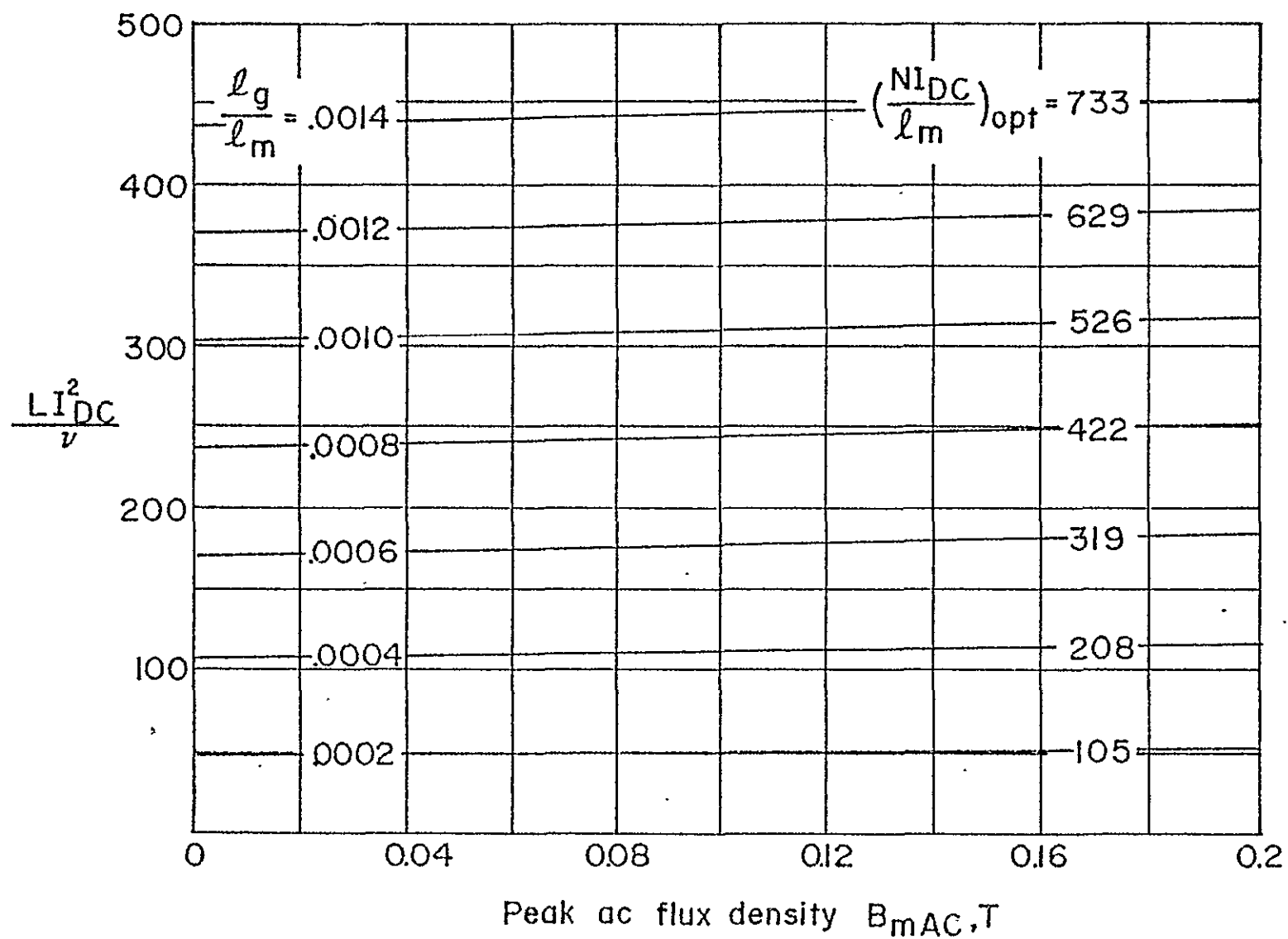


Figure 5.6. Design curves for Permalloy 80 which take finite ac flux excursions into account.

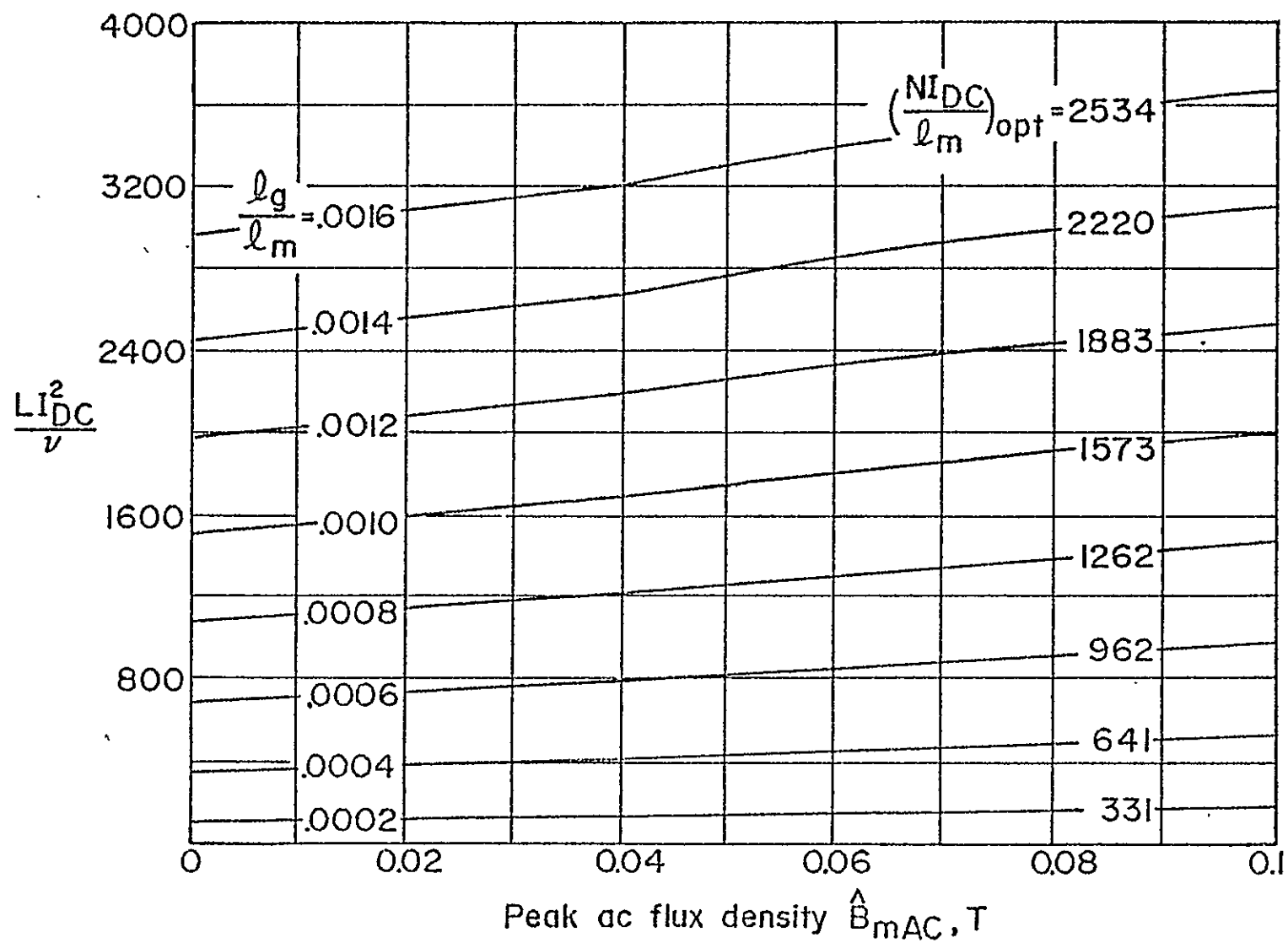


Figure 5.7. Design curves for Supermendur which take finite ac flux excursions into account.

relative incremental permeability curves in conjunction with the design relationships (5.14) and (5.15). The algorithms used in generating these design curves are explained in detail in Appendix H. For any assigned value of air-gap ratio ℓ_g/ℓ_m , the right-hand side of (5.14) can be considered to be a function of H_{mQ} and \hat{B}_{mAC} only, and a curve of LI_{DC}^2/ν versus \hat{B}_{mAC} for some value of H_{mQ} can be produced. To do this, for a specified H_{mQ} , a value of $\hat{B}_{mAC} = \hat{B}_{mAC,min}$ is assigned, and the values of B_{mQ} and μ_Δ corresponding to H_{mQ} and $\hat{B}_{mAC,min}$ are obtained from curves such as those of Figure 4.2 and Figure 4.3, respectively. These values are substituted in equation (5.14) to determine the corresponding value of LI_{DC}^2/ν . Similarly, the values for LI_{DC}^2/ν corresponding to $\hat{B}_{mAC,min}$ for various values of H_{mQ} are obtained in this manner. The optimum value of $H_{mQ} = H_{mQ,opt}$ for a specified value of ℓ_g/ℓ_m which yields the maximum value of LI_{DC}^2/ν is used in generating the design curve for a given ℓ_g/ℓ_m . The value of $NI_{DC}/\ell_m = (NI_{DC}/\ell_m)_{opt}$ corresponding to $H_{mQ,opt}$ is calculated from (5.15). Using $H_{mQ,opt}$ for H_{mQ} in (5.14) and varying \hat{B}_{mAC} from the specified minimum $\hat{B}_{mAC,min}$ to the maximum $\hat{B}_{mAC,max}$, a curve of LI_{DC}^2/ν versus \hat{B}_{mAC} is obtained as illustrated in Figure 5.5 for silicon steel. In a similar manner, design curves for other air-gap ratios are obtained.

Using these design curves, an inductor can be designed to meet the requirements of specified inductance L , dc winding current I_{DC} , rms value of the sinusoidal inductor voltage V_{AC} , and frequency f of the ac voltage. Both the ordinate LI_{DC}^2/ν and the parameter $(NI_{DC}/\ell_m)_{opt}$ increase as the air-gap ratio is increased, as seen from the design curves. For a selected air-gap ratio, the value for parameter LI_{DC}^2/ν also increases with increase in value of peak ac flux excursion \hat{B}_{mAC} . For a selected core, the value of

LI_{DC}^2/v is determined using the specified values of L and I_{DC} , and the known volume v of the chosen core. The corresponding values of ℓ_g/ℓ_m , $(NI_{DC}/\ell_m)_{opt}$, and \hat{B}_{mAC} are determined from the curves in Figures 5.5, 5.6 or 5.7. The required values of air gap ℓ_g and turns N are thus determined from the specified values of I_{DC} and the known mean path length ℓ_m of the selected core. The actual value for the \hat{B}_{mAC} is calculated from (5.12). To meet the design requirements under all operating conditions, the value of \hat{B}_{mAC} calculated from (5.12) should be greater than the value obtained from the design curves; in other words, the designer should insure operation on the selected ℓ_g/ℓ_m curve at a point corresponding to a value always higher than the calculated LI_{DC}^2/v .

In the following section, the complete procedure for designing an air-gapped inductor using these design curves is developed and an example is presented.

5.5 Design Procedure

Using the design curves developed in the preceeding section, a step-by-step procedure for designing air-gapped inductors is now presented.

- [A] The specifications for the inductor are: desired minimum inductance L ; maximum dc winding current I_{DC} ; minimum rms value of ac inductor voltage V_{AC} ; frequency f of ac voltage; maximum winding factor $F_{w,max}$.
- [B] 1) Choose magnetic material
2) Select core: ℓ_m , A_m , v , window area A_{wn} .
- [C] Calculate LI_{DC}^2/v : Using the specified value of L and I_{DC} in [A] and

known ν of the selected core in [B], the value of LI_{DC}^2/ν is calculated.

- [D] Choose a design curve corresponding to the smallest air-gap ratio that intersects the line parallel to the abscissa and passing through the ordinate point corresponding to LI_{DC}^2/ν calculated in [C].
- [E] Read from the design curve: Read the values of corresponding $(NI_{DC}/\ell_m)_{opt}$, and \hat{B}_{mAC} at the intersection.
- [F] Calculate ℓ_g , N , and \hat{B}_{mAC} : From the known specifications and core dimensions in [A] and [B] and from [E], the air-gap length ℓ_g , turns N , and \hat{B}_{mAC} are calculated using the equations

$$\ell_g = (\ell_g/\ell_m)\ell_m$$

$$N = \frac{(NI_{DC}/\ell_m)_{opt} \ell_m}{I_{DC}}$$

$$\hat{B}_{mAC} = \frac{V_{AC}}{\sqrt{2}\pi N f A_m}$$

- [G] If \hat{B}_{mAC} calculated in step [F] is greater than that obtained in step [E], continue to step [H]. If not, choose a curve corresponding to a larger air-gap ratio and return to step [E].
- [H] Determine wire size and check windability: Calculate the rms winding current I_{Xe} using step [0] in flow chart 3, Figure 4.7 in Chapter IV and select wire size based on this from a wire table. Compute the winding factor F_w . If $F_w \leq F_{w,max}$, the design is complete. If not, select a larger core and return to step [B].

To illustrate the design procedure, an example is now presented using these design curves. To provide a comprehensive comparison of all

three methods, the same example is repeated using Hanna's curves, and using the computer program for optimum design presented in Chapter IV.

5.5.1 Example Using New Design Curves

- [A] Specifications: desired minimum inductance $L = 0.55$ H; maximum dc winding current $I_{DC} = 0.2$ A; minimum rms value of ac inductor voltage $V_{AC} = 5.0$ V; frequency of ac voltage $f = 120$ Hz; maximum winding factor $F_{w,max} = 0.4$.
- [B] 1) Choose magnetic material: 3-percent grain-oriented silicon steel
- 2) Select core: $\ell_m = 0.12$ m; $A_m = 1.613 \times 10^{-4}$ m²; $\nu = 1.936 \times 10^{-5}$ m³; $A_{wn} = 4.838 \times 10^{-4}$ m².
- [C] Calculate LI_{DC}^2/ν : $LI_{DC}^2/\nu = 1137$
- [D] The design curve corresponding to $\ell_g/\ell_m = 0.0014$ is chosen in Figure 5.5.
- [E] Read from design curves for the chosen magnetic material: read the values for $(NI_{DC}/\ell_m)_{opt}$, and \hat{B}_{mAC} from Figure 5.5 corresponding to the value of $LI_{DC}^2/\nu = 1137$ calculated in step [C].

$$\frac{\ell_g}{\ell_m} = 0.0014$$

$$\left(\frac{NI_{DC}}{\ell_m}\right)_{opt} = 1489 \text{ ampere-turns/meter}$$

$$\hat{B}_{mAC} = 0.058 \text{ T}$$

- [F] Calculate ℓ_g , N , and \hat{B}_{mAC} :

From the known specifications and core dimensions in [A] and [B] and from [E]

$$\ell_g = 1.68 \times 10^{-4} \text{ m}$$

$$N = 894$$

$$\hat{B}_{mAC} = 0.065 \text{ T}$$

[G] \hat{B}_{mAC} calculated in step [F] is greater than that obtained in step [E], continue to step [H].

[H] Calculate I_{Xe} and choose wire size: From step [O] in flow chart 3 in Chapter IV

$$I_{Xe} = 0.2007 \text{ A}$$

Using a current density of $5.0671 \times 10^{-7} \text{ m}^2/\text{A}$ (1000 circular mils/A), wire size AWG 27 is satisfactory. For AWG 27, the total area of the wire and insulation $A_{wr} = 1.312 \times 10^{-7} \text{ m}^2$ (259 circular mils); $F_w = 0.24$; selected core is windable and design is completed.

5.5.2 Example Using Hanna's Curves

The example in Section 5.5.1 using the same core size and magnetic material is now repeated using Hanna's Curves. Corresponding to the value of $LI_{DC}^2/v = 1137$ calculated in step [C], the values for ℓ_g/ℓ_m and NI_{DC}/ℓ_m are read from Hanna's curves in Figure 5.2.

$$\frac{\ell_g}{\ell_m} = 0.0016$$

$$\frac{NI_{DC}}{\ell_m} = 1550 \text{ ampere-turns/meter}$$

The values for the air gap ℓ_g and N are calculated from the known core dimensions and specified I_{DC} .

$$N = 930$$

$$\ell_g = 1.92 \times 10^{-4} \text{ m}$$

Based on the dc current in the winding $I_{DC} = 0.2 \text{ A}$ and from step [F] and [G], the wire size AWG 27 chosen and winding factor F_w is calculated as 0.25.

Thus it is seen that designs obtained using Hanna's curves require a larger air gap and larger number of turns N for the winding to meet the same design requirements.

The above example was repeated using the computer program presented in Chapter IV. Using the same magnetic core material data and core dimensions, the following results were obtained from a computer program which implements the optimization algorithm described earlier in Flow Chart 2 of Figure 4.5. The results of the designs using Hanna's curves and the design curves presented in this chapter are recapitulated for comparison

	N	ℓ_g
Hanna's Curves	930	$1.92 \times 10^{-4} \text{ m}$
New Design Curves	894	$1.68 \times 10^{-4} \text{ m}$
Optimized Design, Chapter IV	861	$1.60 \times 10^{-4} \text{ m}$

From the above table it is seen that the design obtained using Hanna's curves yields the largest number of turns N and air gap ℓ_g and the design obtained using the computer-implemented optimization algorithm yields the smallest number of turns N and air gap ℓ_g to meet the same design requirements. The design obtained using curves presented in this chapter requires a larger air gap and larger number of turns N than the optimized design but smaller than the design using Hanna's curves.

5.6 Comparison with Hanna's Method

The design relationships used in generating Hanna's curves and the design curves presented in this chapter, are given by (5.5) and (5.6), and (5.14) and (5.15), respectively. As mentioned earlier, the value of relative incremental permeability μ_{Δ} in (5.5) is for very small values of peak ac flux excursion \hat{B}_{mAC} and depends only on the dc operating point H_{mQ} on the normal magnetization curve. The values of μ_{Δ} used in (5.14) are taken from a family of relative incremental permeability curves shown in Figure 4.3, and depend on both the \hat{B}_{mAC} and H_{mQ} . Thus for a selected air-gap ratio, a curve of LI_{DC}^2/ν versus NI_{DC}/ℓ_m is obtained when the dc operating point H_{mQ} on the normal magnetization curve is varied from some minimum value to some maximum value. As seen from Hanna's curves in Figure 5.2, for a given air-gap ratio the curve of LI_{DC}^2/ν approaches a maximum value for some H_{mQ} . In the case of the design relationship given by (5.14), as explained in Appendix H, for a given air-gap ratio a curve of LI_{DC}^2/ν versus \hat{B}_{mAC} can be obtained for each dc operating point H_{mQ} on the normal magnetization curve as the peak ac flux excursion \hat{B}_{mAC} is varied from some minimum to maximum value. For a given H_{mQ} , the minimum value of LI_{DC}^2/ν occurs at the point where \hat{B}_{mAC} is minimum. Hanna's curves are for very small values of ac flux excursions, and thus for a given air-gap ratio, Hanna's curves can be considered as loci of these minimum values of LI_{DC}^2/ν . As discussed in Appendix H, only the curve corresponding to the maximum value of LI_{DC}^2/ν is used as one of the design curves presented in Fig. 5.5 in this chapter. For a given air-gap ratio, the minimum value of LI_{DC}^2/ν that is obtained from the design curves in this chapter corresponds to the maximum value of

LI_{DC}^2/ν obtained from Hanna's curves. Thus, for very small values of ac flux excursions, the design curves presented here approach the maximum values of Hanna's curves. By taking larger ac flux excursions into account, advantage is taken of higher values of relative incremental permeability in calculating the design parameter LI_{DC}^2/ν . Therefore, for the same value of desired inductance, a smaller number of turns is always required when using the design curves presented in this chapter than that determined using Hanna's curves.

5.7 Experimental Verification

A number of type "C" cores made of grain-oriented 3-percent silicon steel, have been designed and assembled according to the results from the design procedure. The measured values of inductance and ac flux-density excursion agreed with values obtained from the design procedure within five percent. Because it is impractical to adjust the air-gap length to the exact design value specified by the design results, a part of the difference between the measured and predicted performance can be attributed to this effect.

5.8 Conclusions

Specially prepared magnetic core data in the form of curves useful for designing air-gapped inductors were presented. These curves make use of core data available from manufacturers of air-gapped cores. Making use of these curves, a straightforward method of determining the length of the

air gap and the number of turns for the winding is presented. As opposed to Hanna's curves, by incorporating into the design curves relative incremental permeability data, the large ac flux excursions encountered in filter inductors are taken into account. Advantage is taken of the larger values of relative incremental permeability for finite ac flux excursions. For a specified air-gap ratio, these design curves yield the maximum value for LI_{DC}^2/v . The design obtained from Hanna's curves is more conservative as it yields a larger number of turns N for the winding than needed to operate under finite ac flux excursions. The design obtained from the design curves presented in this chapter is not optimized in the sense defined in Chapter IV but always yields a smaller number of turns than that obtained from Hanna's curves.

CHAPTER VI

DESIGN OF ENERGY-STORAGE REACTORS FOR DC-TO-DC CONVERTERS USING AIR-GAPPED MAGNETIC-CORE STRUCTURES

6.1 Introduction

This chapter develops the procedure for designing the energy-storage reactor for dc-to-dc converters using an air-gapped core. The development here follows closely the material presented in Ref. [15].

Methods for designing the energy-storage reactor for dc-to-dc converters using computer-aided and table-aided techniques have been developed which use energy balance relationships and a designer-selected maximum flux density in the magnetic core as the major design constraints [9, 12]. These procedures cover the reactor design for the twelve converter configurations which result from the combination of the three single-winding power stages (voltage stepup, current stepup, voltage stepup/current stepup), and the two-winding voltage stepup/current stepup power stage, and the three controllers (constant frequency, constant on-time and constant off-time). Simplified circuit diagrams of the four power stages are illustrated in Figure 6.1. Developed particularly with gapless powdered permalloy and ferrite

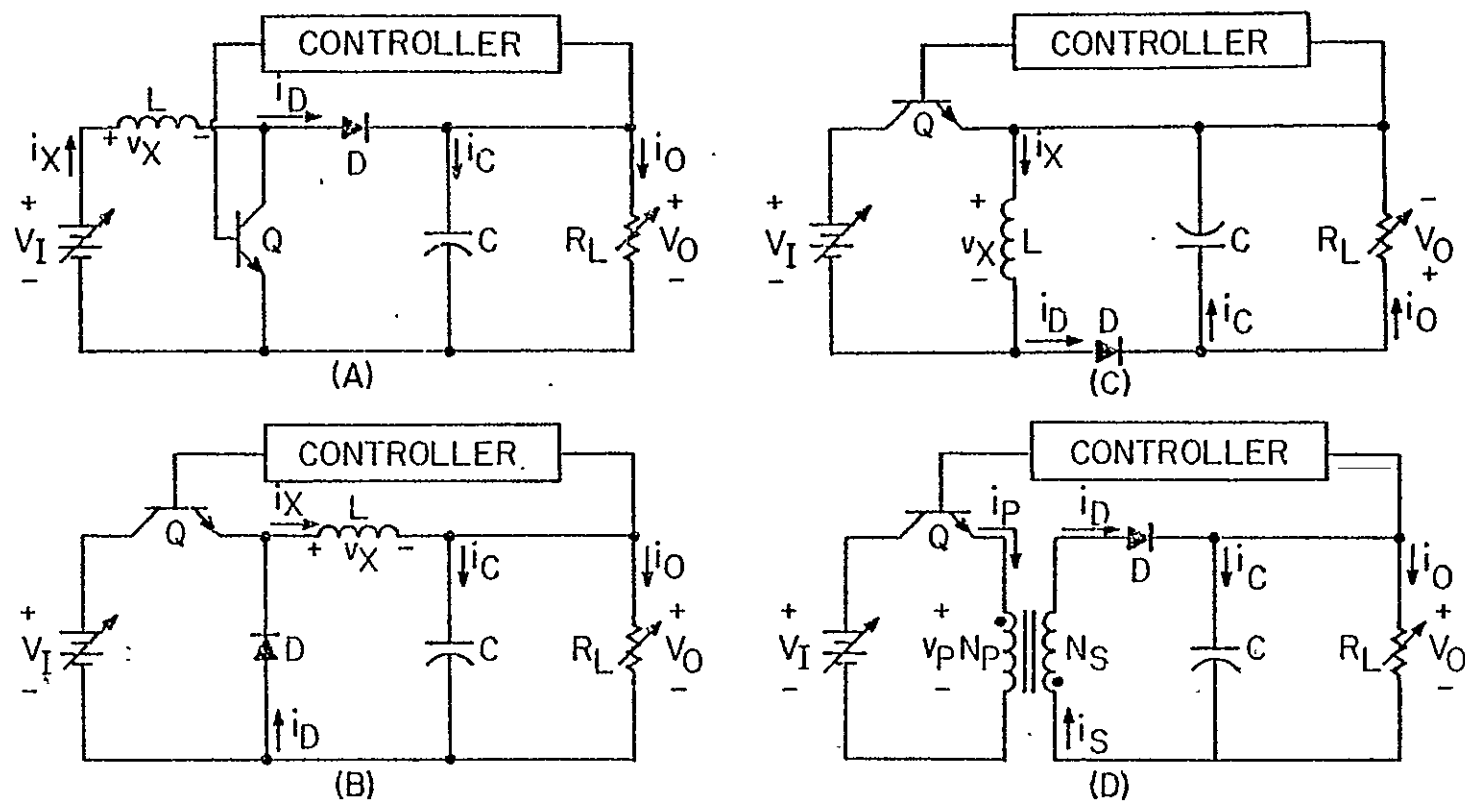


Figure 6.1. Four Energy-Storage DC-to-DC Converters. (A) Single-Winding Voltage Stepup. (B) Single-Winding Current Stepup. (C) Single-Winding Voltage Stepup/Current Stepup. (D) Two-Winding Voltage Stepup/Current Stepup.

toroidal cores in mind, past procedures make use of a collection of data from a finite population of core sizes and permeabilities. This paper builds upon the analytically derived design equations presented in these references and develops new procedures which permit the design of the energy-storage reactor using a magnetic core with an air gap. The use of such cores permits the selection to be made from an innumerable population of core size-permeability combinations and makes available a wider range of magnetic core sizes, particularly in the larger volume sizes.

6.2 Analysis of the Magnetic Circuit

The introduction of an air gap of length ℓ_g into a magnetic circuit with mean magnetic path length ℓ_m causes the permeability parameters usually associated only with the non-air-gapped circuit to change rather considerably. The composite-circuit permeability parameters, usually referred to as effective permeabilities, may be obtained from approximations given below, provided that the length of the air gap is small enough so that the total path length of the air-gapped circuit, $\ell_m + \ell_g$, may be approximated by the quantity ℓ_m , and that the cross-sectional areas of the magnetic material A_m and the air gap A_g are taken to be equal, thus implying negligible fringing in the gap region. Under these circumstances, the air gap modifies the effect of the relative normal permeability of the magnetic material, designated by the symbol μ_{DC} , to produce an effective relative normal permeability for the composite magnetic circuit defined by

$$\mu_{DC,eff} = \mu_{DC} / [1 + (\mu_{DC} \ell_g / \ell_m)] \quad (6.1)$$

and the effective relative incremental permeability defined by

$$\mu_{\Delta, \text{eff}} = \mu_{\Delta} / [1 + (\mu_{\Delta} \ell_g / \ell_m)] \quad (6.2)$$

where μ_{Δ} is the relative incremental permeability of the magnetic material alone at the dc bias point of the core. If the quantities $(\mu_{DC} \ell_g / \ell_m)$ and $(\mu_{\Delta} \ell_g / \ell_m)$ are both large with respect to unity, then these two effective relative permeabilities are equal and can be represented by the single symbol μ_{eff} , where

$$\mu_{\text{eff}} = \mu_{DC, \text{eff}} = \mu_{\Delta, \text{eff}} = \ell_m / \ell_g \quad (6.3)$$

Since at any bias point the incremental permeability of the magnetic material is less than the permeability obtained from its normal magnetization curve at the same point, the condition necessary for (6.3) to hold is that $(\mu_{\Delta} \ell_g / \ell_m)$ be large with respect to unity, or

$$\mu_{\Delta} \gg \ell_m / \ell_g \quad (6.4)$$

This condition is one that normally is met without difficulty for most air-gapped magnetic circuits when the magnetic material operates below the knee of its saturation curve and the air-gap ratio (ℓ_g / ℓ_m) is moderately large. An important implication of this condition is that essentially all of the energy stored in the magnetic core is concentrated in the air gap and very little in the magnetic material. The air-gapped reactor appears as a linear element and thus permits use of the analytic relationships of Ref. [12], which are based on an energy-balance analysis of dc-to-dc converters, to be applied directly to the design of air-gapped reactors.

In Ref. [12], Eq. (19), a fundamental relationship between the required minimum volume of a homogeneous powdered permalloy or ferrite magnetic core is established. This relationship, rewritten as

$$v_{\min} = \mu_0 \mu_{\text{eff}} \delta \quad (6.5)$$

is in terms of μ_0 , the permeability of free space, the effective relative permeability, and a factor δ which is defined as

$$\delta = 2\Delta W_{m,\max} / (B_{\max} - B_R)^2 \quad (6.6)$$

The quantity $\Delta W_{m,\max}$ is the amount of energy in joules which must be transferred by the reactor over one switching cycle under the operating condition corresponding to maximum power flow through the converter. This quantity is a function of the power stage specifications and a time parameter which depends on the type of controller. Parameter B_{\max} is a designer-specified maximum value of flux density which is reached but is never exceeded. The choice of a value for B_{\max} depends on the type of magnetic material selected for the reactor. B_R is the residual flux density of the magnetic material.

Using the expression given in (6.3) for effective relative permeability in an air-gapped core subject to the restriction set by (6.4), the minimum volume for meeting the energy transfer requirement for a converter is

$$v_{\min} = \mu_0 \delta \ell_m / \ell_g \quad (6.7)$$

Since the volume of an air-gapped core is equal to the actual cross-sectional area A_m of the magnetic material (gross core area times stacking factor) times the mean magnetic path length, i.e., $v_m = A_m \ell_m$, in order to meet the require-

ments of (6.7), the inequality

$$A_m \ell_g \geq \mu_0 \delta \quad (6.8)$$

must be satisfied. This relationship is of fundamental importance in the present development. The left hand side, under the assumption $A_m = A_g$, represents the volume of the air gap portion of the composite magnetic structure. Thus, (6.8) establishes a minimum value for the volume of the air gap in terms of the permeability of free space and the parameter δ which is a function only of the power stage and controller specifications and the maximum allowable flux density in the core.

From the air-gap volume inequality of (6.8), it is seen that the designer has the choice either of picking a value for A_m , using magnetic core catalog data, then computing the required minimum value of air gap ℓ_g , or picking a value for ℓ_g , then obtaining an appropriate core with A_m greater than the minimum value for core cross-sectional area $A_{m,min}$. These two choices are expressed in (6.9) and (6.10), where the use of minimum values allows an equality relationship.

$$\ell_{g,min} = \mu_0 \delta / A_m \quad (6.9)$$

$$A_{m,min} = \mu_0 \delta / \ell_g \quad (6.10)$$

In summary, in this section the conditions required of an air-gapped core to function as the energy-storage reactor in a dc-to-dc converter have been established which provide a simple relationship between the effective relative permeability of the composite structure and the mean magnetic path length and the air gap length. Using the results of previous procedures based on maximum energy transfer requirements, a relationship between the

volume of the air gap portion of the core and converter specifications and maximum allowable flux density was developed. This relationship may be interpreted to yield minimum values for either the core cross-sectional area or the air gap length. In the following section, the complete procedure for designing an energy-storage reactor for this application is developed and an example is presented.

6.3 Design Procedure

Given the specifications of the power stage and controller, the essential elements of the design procedure involve the selection of the geometrical form for the magnetic circuit, the type of magnetic material, and the determination of the core size, the air gap length, and the number of turns. In this section, the detailed steps are outlined and an example is presented to illustrate the design procedure. The power stages included in the design procedures are the three frequently encountered single-winding configurations for voltage stepup (VU), for current stepup (CU), and for voltage stepup/current stepup (UD), and the two-winding configuration for voltage stepup/current stepup (2UD). For each power stage, three controllers--constant-frequency (FQ), constant on-time (TN), and constant off-time (TF)--are considered. In Ref. [12], equations are identified, where appropriate, by equation numbers with suffix letters which identify the power stage type. The same form of identification is used when needed in the step-by-step procedure which follows.

A. The specifications for the converters considered in this paper are: desired output voltage V_0 ; expected minimum and maximum input voltages $V_{I,min}$ and $V_{I,max}$; transistor saturation voltage V_Q ; diode voltage drop V_D ; expected maximum value of output power $P_{0,max}$;

and a time parameter which depends on the type of controller employed--the switching period $T = 1/f$ for (FQ), transistor on-time t_{on} for (TN), or transistor off-time t_{off} for (TF). In the two-winding configuration, the presence of the additional winding, as pointed out in [10], provides an additional degree of freedom in the design procedure. By utilizing the extra degree of freedom, any one of various design constraint options can be incorporated into the procedure. These design constraints are: A, duty cycle centered at a specified value; B, specified minimum duty cycle; C, specified range of duty-cycle variation; D, specified maximum transistor collector-to-emitter voltage; E, specified maximum diode reverse voltage; H, specified maximum duty cycle; and J, specified turns ratio. Table II in Ref. [12] presents the option constraint equations for the turns ratio $\gamma = \gamma_y = N_p/N_s$, where the subscript y represents one of the constraints A, B, C, D, E, H or J.

B. Choices that are to be made which are associated with the magnetic circuit are: type of magnetic structure and material, and maximum allowable flux density B_{max} . Compute the values of ζ and δ , which are functions of the converter specifications and B_{max} using from Ref. [12], Eq. (1), (3), or (5), depending on the controller type (VU), (CU), (UD), or (2UD).

C. Specify either the air gap length ℓ_g or the cross-sectional area A_m of a selected magnetic core. If the air gap is specified, continue to step D. If A_m is chosen, then additionally selecting the core with the smallest value of ℓ_m results in the smallest core volume and gives the greatest assurance that the inequality in (6.4) is satisfied. Proceed to step E.

D. Compute the value of $A_{m,min}$ using the value of ℓ_g chosen, select a core with A_m greater than or equal to $A_{m,min}$ and a value of ℓ_m as discussed in step C, and compute the value of K_g using the equations

$$A_{m,min} = \mu_0 \delta / \ell_g$$

$$K_g = 1 + [1 - (\zeta/\delta)(A_{m,min}/A_m)]^{1/2}$$

E. Compute the value of $\ell_{g,min}$ using the value of A_m chosen, select an air gap ℓ_g which is greater than or equal to $\ell_{g,min}$, and compute the value of K_g using the equations

$$\ell_{g,min} = \mu_0 \delta / A_m$$

$$K_g = 1 + [1 - (\zeta/\delta)(\ell_{g,min}/\ell_g)]^{1/2}$$

Continue to step F.

F. Using the value of ℓ_g obtained in step C or E, and the value of ℓ_m for the core selected in step C or D, compute the effective relative permeability, using the approximation given by (6.3)

$$\mu_{eff} = \ell_m / \ell_g$$

As a caution, at this point the designer should be aware that too large a value for μ_{eff} might indicate that the inequality in (6.4) is not satisfied. In such a case, choice of a larger value for ℓ_g or a smaller value for A_m in step C will result in a smaller μ_{eff} . Continue to step G.

G. Compute K_{10} using the appropriate expression, according to type of power stage.

$$K_{10} = \begin{cases} (V_0/2P_{0,\max})(V_{I,\min}-V_Q)(B_{\max}-B_R)/(V_0+V_D-V_Q) & \text{(VU)} \\ (V_0/2P_{0,\max})(B_{\max}-B_R) & \text{(CU)} \\ (V_0/2P_{0,\max})(V_{I,\min}-V_Q)(B_{\max}-B_R)/(V_{I,\min}+V_0+V_D-V_Q) & \text{(UD)} \\ (V_0/2P_{0,\max})(V_{I,\min}-V_Q)(B_{\max}-B_R)/(\gamma(V_{I,\min}-V_Q)+V_0+V_D) & \text{(2UD)} \end{cases}$$

Using the value of ℓ_g obtained in step C or E, and the values of K_{10} and K_9 just obtained, compute the turns N (for single-winding reactors) or N_p and N_s (for a two-winding reactor) and inductance L or L_p and L_s .

$$N \text{ or } N_p = K_9 K_{10} \ell_g / \mu_0$$

$$N_s = \gamma N_p$$

$$L = \mu_0 N^2 A_m / \ell_g$$

$$L_p = \mu_0 N_p^2 A_m / \ell_g$$

$$L_s = L_p (N_s / N_p)^2$$

Compute the maximum rms winding current $I_{Xe,\max}$ using Ref. [12], Eq. (2), (4), (6), depending on controller type, for (VU), (CU), (UD), or (2UD). Select the wire size and compute the windability of the reactor. If the winding factor is too large, return to step C and choose a smaller air gap or choose another core of same A_m with larger value of ℓ_m .

To illustrate the design procedure outlined above, an example design is now presented using the International System of Units (SI). The power stage is a single-winding voltage stepup configuration and is controlled by a constant-frequency controller.

A. The specifications are:

$$V_{I,\min} = 18 \text{ V}$$

$$V_Q = 0.5 \text{ V}$$

$$V_{I,\max} = 24 \text{ V}$$

$$V_D = 0.8 \text{ V}$$

$$V_O = 28 \text{ V}$$

$$f = 2 \text{ kHz}$$

$$P_{O,\max} = 400 \text{ W}$$

$$T = 500 \text{ } \mu\text{s}$$

B. Choose a C-core structure with magnetic material of grain-oriented 3% silicon steel with tape thickness of $1.016 \times 10^{-4} \text{ m}$ (4 mils). Choose $B_{\max} = 1.0 \text{ T}$. Using Eq. (1,VU), Ref. [12], assuming the residual flux density $B_R = 0$,

$$\begin{aligned} \delta = \zeta &= (2TP_{O,\max}/V_O)(V_O + V_D - V_{I,\min})/(B_{\max} - B_R)^2 \\ &= 0.1543 \end{aligned}$$

C. Choose the air gap length ℓ_g to be $6.096 \times 10^{-4} \text{ m}$ (24 mils).

D. Compute $A_{m,\min}$, select core, and compute K_2 .

$$A_{m,\min} = \mu_0 \delta / \ell_g = 3.181 \times 10^{-4} \text{ m}^2$$

Choose a core with gross core area of $3.632 \times 10^{-4} \text{ m}^2$. Using a stacking factor of 0.9, $A_m = 3.269 \times 10^{-4} \text{ m}^2$. Choose the smallest available value of $\ell_m = 0.1832 \text{ m}$ and window area $A_{wn} = 1.116 \times 10^{-3} \text{ m}^2$.

$$K_g = 1 + [1 - (\zeta/\delta)(A_{m,\min}/A_m)]^{1/2} = 1.164$$

F. Compute μ_{eff}

$$\mu_{\text{eff}} = \ell_m / \ell_g = 300$$

G. Compute K_{10} , N , L , and $I_{X_{e,\text{max}}}$. For the voltage stepup configuration,

$$\begin{aligned} K_{10} &= (V_0 / 2P_{0,\text{max}})(V_{I,\text{min}} - V_Q)(B_{\text{max}} - B_R) / (V_0 + V_D - V_Q) \\ &= 2.164 \times 10^{-2} \end{aligned}$$

$$N = K_9 K_{10} \ell_g / \mu_0 = 13 \text{ turns}$$

$$L = \mu_0 N^2 A_m / \ell_g = 114 \text{ } \mu\text{H}$$

Using Eq. (2,VU), Ref. [2],

$$\begin{aligned} I_{X_{e,\text{max}}} &= \\ \frac{P_{0,\text{max}}(V_0 + V_D - V_Q)}{V_0(V_{I,\text{min}} - V_Q)} &\left[1 + \frac{1}{12} \left[\frac{TV_0(V_{I,\text{min}} - V_Q)^2(V_0 + V_D - V_{I,\text{min}})}{LP_{0,\text{max}}(V_0 + V_D - V_Q)^2} \right]^2 \right]^{1/2} = 24.6 \text{ A} \end{aligned}$$

Using a current carrying capacity of $5.067 \times 10^{-7} \text{ m}^2/\text{A}$ (1000 circular mils/A), a wire size of AWG 6 is selected. For double-coated insulation, the winding factor is 0.167, which is satisfactory, and the design is complete.

6.4 Conclusions

The procedure for designing the energy-storage reactor for dc-to-dc converters which is reported in this chapter is applicable to a variety of types of magnetic structures in which an air gap is inserted. The analysis which leads to the fundamental relationship for the required minimum volume of the air gap region depends upon the principal assumption that the product of the incremental permeability at the core operating point and the air gap

ratio be large with respect to unity. This condition usually can be met with most common structures and materials. Since the required minimum air gap volume is the product of the gap length and cross-sectional area, the designer has the choice of specifying either one and computing the minimum value of the other. The quantity determining the minimum required volume is a function of the power stage and controller specifications and the specified maximum flux density in the core.

Previously reported research results provide the basic expressions which permit calculation of the minimum air gap volume for twelve combinations of power stages and controllers. Once the air gap volume is determined, either by initially specifying the air gap and choosing a core with given cross-sectional area or by specifying a core at the outset with a given cross-sectional area and then determining the air gap, the remaining important design parameters can be obtained. Using the values for the physical dimensions of the chosen core, including air gap, the effective relative permeability, turns, inductance, and maximum rms winding current can be determined, a wire size selected, and windability checked. If the chosen core is not windable, the design procedure leads back to a point where another choice may be made which will lead to a windable design.

Since the procedure is independent of the type of air-gapped structure and magnetic material and depends only on the physical dimensions of the chosen core and air gap, it should be useful in many applications where powdered permalloy or ferrite cores may not be applicable or available because of costs or size requirements.

CHAPTER VII

CONCLUSIONS AND SUGGESTIONS FOR FUTURE RESEARCH

7.1 Conclusions

The research reported in this dissertation provides the power electronics system designer with useful analytical guidance and practical usable procedures for designing LC-filters for use with full-wave rectifiers, and air-gapped inductors for filters and for a group of widely used dc-to-dc converters. The design procedures presented in this dissertation eliminate most of the conventional trial-and-error procedures which are frequently followed in designing these power subsystems. Methods for analysis of full-wave rectifier LC-filter circuits operating both in the continuous-conduction mode and discontinuous-conduction mode are also presented. The design procedures presented here are well suited to computer-aided design techniques, but calculations required in most of the procedures are easily made on an electronic pocket calculator.

Chapters II and III present the steady-state analyses of rectifier LC-filters operating both in the continuous- and discontinuous-conduction

modes. In Chapter II analyses are presented for the case when the impedance of the sinusoidal supply source is assumed to be zero. In Chapter III a finite value for the source impedance is assumed. In the continuous-conduction mode, linear circuit analysis techniques are employed, while in the case of the discontinuous mode, the method of analysis requires computer solution of the piecewise-linear differential equations. An algorithm is presented which permits rapid determination of the periodic steady-state in the discontinuous mode using digital computation. From these methods of analysis sets of curves and approximate relationships useful for designing filters are generated. Using these curves or relationships, a designer can select the inductor, the capacitor, the diodes, and the transformer to meet a set of specified requirements.

In Chapter IV, two design procedures are presented for the design of inductors using air-gapped magnetic cores. The first uses a computer to produce a design which is optimized in the sense of minimum core volume and minimum number of turns to meet a required minimum inductance over a specified range of circuit operating conditions. The second procedure does not yield a design which is optimized in the above sense, but it has the advantage that it may readily be followed by hand calculations or with a calculator. An easily used screening process which permits a designer to identify candidate cores for which a physically realizable air gap is possible, is also provided in the second procedure.

Using the analysis of a magnetic circuit with air gap which was presented in Chapter IV, specially prepared magnetic core data in form of design curves are generated and presented in Chapter V. The most important feature

of this approach is the straight-forward method for computing the number of turns and the length of the air gap for the selected core for meeting a set of design requirements. This approach does not yield as much information as the methods in Chapter IV do, but it does provide the designer with an easy method to quickly reach a workable design.

In Chapter VI, a procedure for designing energy-storage reactors for dc-to-dc converters using air-gapped cores is presented. The analysis, based on the energy-transfer requirement of the reactor, leads to a simple relationship for the required minimum volume of the air gap. Determination of this minimum air gap volume then permits the selection of either an air gap or a cross-sectional area. Having picked one parameter, the minimum value of the other immediately leads to selection of the physical magnetic structure. Although the magnetic cores used in the examples throughout the dissertation are type C cores, the design equations and procedures presented are independent of core geometry and magnetic material used and can be extended rather easily to other shapes such as type E cores, ring cores, and certain lamination structures. It is believed that the design procedures presented in this dissertation can significantly reduce the time and the effort required to design LC-filters for full-wave rectifier supplies, filter inductors, and energy-storage reactors in dc-to-dc converters.

7.2 Suggestions for Future Research

Three particular areas for future research have suggested themselves during the course of this research effort. The first area is concerned with the analysis of the LC-filter when it is a part of the regulator system

in which the source waveform is a square wave with a certain duty ratio. It is suggested that the analysis methods presented here be investigated for applicability to the complete filter-regulator system.

Secondly, in the dissertation, in the design procedure for inductors with air-gapped cores a uniform air-gap was assumed. It is suggested that analysis of the magnetic circuit with non-uniform air-gap be attempted and advantages and disadvantages of inductors with non-uniform air-gap be investigated. Thirdly, in the design procedure for air-gapped inductors, fringing flux was assumed to be negligibly small. It is suggested that design of air-gapped inductors be attempted for the case when fringing flux is a significant portion of total flux in the core.

APPENDICES

130

Appendix A
DERIVATION OF EXPRESSIONS FOR THE LC FILTER OPERATING
IN THE CONTINUOUS-CONDUCTION MODE, CHAPTER II

The principle of superposition is used to compute steady-state voltages and currents in an LC-filter operating in the continuous-conduction mode. The equivalent circuit of the filter operating in the continuous-conduction mode is shown in Figure 2.2. First, reducing the sinusoidal component of the voltage source v_I' to zero, the dc currents and voltages in the filter due to the application of a dc voltage source of value $2V_{Im}/\pi$ are given as below:

$$I_X = \frac{2V_{Im}}{\pi R_L} \quad (A1)$$

$$V_0 = \frac{2V_{Im}}{\pi} \quad (A2)$$

The response of the filter to the second harmonic component of the voltage source v_I' is computed by the sinusoidal steady-state method. The filter impedance $Z(j2\omega)$ as seen by the sinusoidal source of frequency 2ω in radians/sec is given by

$$Z(j2\omega) = j2\omega L + \frac{\frac{R_L}{j2\omega C}}{R_L + \frac{1}{j2\omega C}} \quad (A3)$$

Eq. (A3) is simplified to

$$Z(j2\omega) = \frac{(R_L - 4\omega^2 L C R_L) + j2\omega L}{1 + j2\omega C R_L} \quad (A4)$$

The magnitude $|Z(j2\omega)|$ and phase ψ of filter impedance $Z(j2\omega)$ may be obtained from (A4) in terms of ω_N , κ , and R_L

$$|Z(j2\omega)| = R_L \frac{\sqrt{1 - 8\omega_N^2 + 16\omega_N^4 + 4\kappa^2}}{\sqrt{1 + (4\omega_N^4/\kappa^2)}} \quad (A5)$$

$$\psi = \arctan [2\kappa/(1 - 4\omega_N^2)] - \arctan (2\omega_N^2/\kappa) \quad (A6)$$

From Figure 2.2, the value of i_X due to second harmonic component is given by

$$i_X = -\frac{4V_{Im}}{3\pi} \frac{\cos 2\omega t}{Z(j2\omega)} \quad (A7)$$

Substituting $|Z(j2\omega)|$ and ψ from (A5) and (A6) for $Z(j2\omega)$ in (A7) leads to

$$i_X = -\frac{4V_{Im} \sqrt{1 + (4\omega_N^4/\kappa^2)}}{3\pi R_L \sqrt{1 - 8\omega_N^2 + 16\omega_N^4 + 4\kappa^2}} \cos(2\omega t - \psi) \quad (A8)$$

Defining $Z_1(j2\omega)$ as the parallel combination of R_L and $1/j2\omega C$

$$|Z_1(j2\omega)| = \frac{R_L}{\sqrt{1 + (4\omega_N^4/\kappa^2)}} \quad (A9)$$

$$\phi = -\arctan (2\omega_N^2/\kappa) \quad (A10)$$

Thus, the output voltage v_0 is given by

$$v_0 = i_X Z_1(j2\omega) \quad (A11)$$

Substituting for i_X and $Z_1(j2\omega)$ from (A8), (A9), and (A10) in (A11) and simplifying leads to

$$v_0 = - \frac{4V_{Im}}{3\pi \sqrt{1-8\omega_N^2+16\omega_N^4+4\kappa^2}} \cos(2\omega t - \psi + \phi) \quad (A12)$$

The total inductor current i_X is obtained by summing the dc and ac components given by (A1) and (A8), respectively

$$i_X = \frac{2V_{Im}}{\pi R_L} - \frac{4V_{Im} \sqrt{1+(4\omega_N^4/\kappa^2)}}{3\pi R_L \sqrt{1-8\omega_N^2+16\omega_N^4+4\kappa^2}} \cos(2\omega t - \psi) \quad (A13)$$

Using the same approach, the total output voltage v_0 is obtained by summing components given by (A2) and (A12),

$$v_0 = \frac{2V_{Im}}{\pi} - \frac{4V_{Im}}{3\pi \sqrt{1-8\omega_N^2+16\omega_N^4+4\kappa^2}} \cos(2\omega t - \psi + \phi) \quad (A14)$$

From the alternating component in (A14), the peak-to-peak ripple voltage V_{Op} is

$$V_{Op} = \frac{8V_{Im}}{3\pi \sqrt{1-8\omega_N^2+16\omega_N^4+4\kappa^2}} \quad (A15)$$

and the average output voltage V_0 from (A14) is

$$V_0 = \frac{2V_{Im}}{\pi} \quad (A16)$$

from (A13), the peak and rms values of inductor current, I_{xm} and I_{xe} , are

$$I_{xm} = \frac{4V_{Im}}{\pi R_L} \left[\frac{1}{2} + \frac{\sqrt{1+(4\omega_N^4/\kappa^2)}}{3\sqrt{1-8\omega_N^2+16\omega_N^4+4\kappa^2}} \right] \quad (A17)$$

$$I_{xe} = \frac{4V_{Im}}{\pi R_L} \left[\sqrt{\frac{1}{4} + \frac{(1+4\omega_N^4/\kappa^2)}{18(1-8\omega_N^2+16\omega_N^4+4\kappa^2)}} \right] \quad (A18)$$

In the case of a center-tapped transformer, current in the two secondary windings flows during alternate half cycles and is equal to i_x . Thus, the rms value of current in each secondary winding I_{Se} is

$$I_{Se} = \sqrt{\frac{1}{2\pi} \int_0^\pi i_x^2 d\theta} \quad (A19)$$

or

$$I_{Se} = \frac{I_{xe}}{\sqrt{2}} \quad (A20)$$

Appendix B

DERIVATION OF EXPRESSIONS FOR THE LC FILTER OPERATING IN THE DISCONTINUOUS-CONDUCTION MODE, CHAPTER II

In this Appendix, the expression for v_0 and i_x given by (2.11) and (2.12), respectively, are derived. The derivations of the expressions for v_0 and i_x when the diodes are conducting in the discontinuous-conduction mode are given in Section B.1. The expressions for the case when the diodes stop conducting are derived in Section B.2.

B.1 Diodes Conducting

The equivalent circuit when a diode is conducting is shown in Figure 2.3A. The state equations for the circuit are

$$L \frac{di_{x1}}{dt} = v_I' - v_{01} \quad (B1)$$

$$C \frac{dv_{01}}{dt} = i_{x1} - \frac{v_{01}}{R_L} \quad (B2)$$

Differentiating (B2) and multiplying by L leads to

$$LC \frac{d^2v_{01}}{dt^2} = L \frac{di_{x1}}{dt} - \frac{L}{R_L} \frac{dv_{01}}{dt} \quad (B3)$$

Substituting for $L \frac{di_{x1}}{dt}$ in (B3) from (B1) and rearranging

$$LC \frac{d^2 v_{01}}{dt^2} + \frac{L}{R_L} \frac{dv_{01}}{dt} + v_{01} = v_I \quad (B4)$$

Let $\theta = \omega t$

$$\frac{dv_{01}}{dt} = \frac{dv_{01}}{d\theta} \frac{d\theta}{dt} = \omega \frac{dv_{01}}{d\theta} \quad (B5)$$

$$\frac{d^2 v_{01}}{dt^2} = \omega^2 \frac{d^2 v_{01}}{d\theta^2} \quad (B6)$$

Substituting for $\frac{dv_{01}}{dt}$ and $\frac{d^2 v_{01}}{dt^2}$ in (B4) from (B5) and (B6) leads to

$$\omega^2 LC \frac{d^2 v_{01}}{d\theta^2} + \frac{\omega L}{R_L} \frac{dv_{01}}{d\theta} + v_{01} = V_{Im} \sin(\theta - \theta_0) \quad (B7)$$

Writing this last equation in terms of ω_N and κ

$$\omega_N^2 \frac{d^2 v_{01}}{d\theta^2} + \kappa \frac{dv_{01}}{d\theta} + v_{01} = V_{Im} \sin(\theta - \theta_0) \quad (B8)$$

B.1.1 Solution for v_{01}

The particular solution of v_{01} due to the forcing function $V_{Im} \sin(\theta - \theta_0)$ is obtained first. Assuming the particular solution for v_{01} to be of the form

$$v_p = A_V \sin \theta + B_V \cos \theta \quad (B9)$$

and substituting the value of v_p and its derivative from (B9) in (B8) and equating the co-efficients for $\sin \theta$ and $\cos \theta$ from both sides of the resulting expression leads to the following set of simultaneous equations for unknowns A_V and B_V

$$A_V(1-\omega_N^2) - B_V \kappa = V_{Im} \cos \theta_0 \quad (B10)$$

$$A_V \kappa + B_V(1-\omega_N^2) = -V_{Im} \sin \theta_0 \quad (B11)$$

Simultaneous solution of (B10) and (B11) yields the following values for A_V and B_V

$$A_V = \frac{V_{Im} [\cos \theta_0 (1-\omega_N^2) - \kappa \sin \theta_0]}{(1-\omega_N^2)^2 + \kappa^2} \quad (B12)$$

$$B_V = \frac{V_{Im} [-\sin \theta_0 (1-\omega_N^2) - \kappa \cos \theta_0]}{(1-\omega_N^2)^2 + \kappa^2} \quad (B13)$$

The homogeneous part of solution is obtained next. The homogeneous part of the equation (B8) is

$$\omega_N^2 \frac{d^2 v_{01}}{d\theta^2} + \kappa \frac{dv_{01}}{d\theta} + v_{01} = 0 \quad (B14)$$

Let the solution be of the form

$$v_h = D e^{\lambda \theta} \quad (B15)$$

Substituting v_h in (B14), the corresponding characteristic equation is

$$\omega_N^2 \lambda^2 + \kappa \lambda + 1 = 0 \quad (B16)$$

For the discontinuous-conduction case

$$4\omega_N^2 > \kappa^2 \quad (B17)$$

Thus, the roots of (B16) are given below

$$\lambda_{1,2} = \beta \pm j\alpha \quad (B18)$$

where

$$\beta = -\kappa/2\omega_N^2 \quad (B19)$$

$$\alpha = (\sqrt{4\omega_N^2 - \kappa^2})/(2\omega_N^2) \quad (B20)$$

The homogeneous part of the solution for v_{01} can be written as

$$v_h = \exp(\beta\theta)\{C_V \sin\alpha\theta + D_V \cos\alpha\theta\} \quad (B21)$$

The complete solution for v_{01} is obtained by adding the particular solution v_p and the homogeneous solution v_h given by (B9) and (B21), respectively

$$v_{01}(\theta) = A_V \sin\theta + B_V \cos\theta + \exp(\beta\theta)\{C_V \sin\alpha\theta + D_V \cos\alpha\theta\} \quad (B22)$$

From (B21),

$$i_{X1} = C \frac{dv_{01}}{dt} + \frac{v_{01}}{R_L} \quad (B23)$$

or

$$i_{X1}(\theta) = \omega C \frac{dv_{01}}{d\theta} + \frac{v_{01}}{R_L} \quad (B24)$$

Substituting the expressions for v_{01} , and its derivative from (B22) into (B24) leads to

$$i_{X1}(\theta) = \frac{1}{R_L} \left[A_i \sin\theta + B_i \cos\theta + \exp(\beta\theta) \{ C_i \sin\alpha\theta + D_i \cos\alpha\theta \} \right] \quad (B25)$$

where

$$A_i = A_V - (B_V \omega_N^2) / \kappa \quad (B26)$$

$$B_i = B_V + (A_V \omega_N^2) / \kappa \quad (B27)$$

$$C_i = C_V + (\omega_N^2 (\beta C_V - \alpha D_V)) / \kappa \quad (B28)$$

$$D_i = D_V + (\omega_N^2 (\beta D_V + \alpha C_V)) / \kappa \quad (B29)$$

B.2 Diodes Not Conducting

The equivalent circuit when diodes are not conducting is shown in Figure 2.3B. The state equations are

$$C \frac{dv_{02}}{dt} + \frac{v_{02}}{R_L} = 0 \quad (B30)$$

$$i_{X2} = 0 \quad (B31)$$

(B30) can be written as

$$\omega C \frac{dv_{02}}{d\theta} + \frac{v_{02}}{R_L} = 0 \quad (\text{B32})$$

Let the solution for (B32) be

$$v_{02} = a e^{\lambda(\theta-\theta_1)} \quad (\text{B33})$$

Substituting for v_{02} in (B32) from (B33), the root of the characteristic equation is found to be

$$\lambda = -\frac{1}{\omega C R_L} = -\frac{\kappa}{\omega_N^2} \quad (\text{B34})$$

Thus

$$v_{02}(\theta) = a [\exp\{-(\theta-\theta_1)\kappa/\omega_N^2\}] \quad (\text{B35})$$

at $\theta = \theta_1$,

$$v_{02} = v_{02}(\theta_1) \quad (\text{B36})$$

From (B35) and (B36)

$$a = v_{02}(\theta_1) \quad (\text{B37})$$

Thus,

$$v_{02}(\theta) = v_{02}(\theta_1) [\exp\{-(\theta-\theta_1)\kappa/\omega_N^2\}] \quad (\text{B38})$$

Appendix C

DERIVATION OF EXPRESSIONS FOR THE LC FILTER WITH NON-ZERO SOURCE IMPEDANCE OPERATING IN THE CONTINUOUS-CONDUCTION MODE, CHAPTER III

In this appendix, the expressions for voltages and currents in the filter circuit with source impedance included, are derived for the case when the filter operates in the continuous-conduction mode.

From the equivalent circuit in Figure 3.2A and following the method in Appendix A, the dc output voltage V_0 and inductor current I_X are given by

$$I_X = \frac{2V_{Im}}{\pi R_L (\rho+1)} \quad (C1)$$

$$V_0 = \frac{2V_{Im}}{\pi(\rho+1)} \quad (C2)$$

For computing response to the second harmonic, the filter impedance $Z(j2\omega)$ seen by the harmonic is

$$Z(j2\omega) = R_I + j2\omega L_{eq} + \frac{\frac{R_L}{j2\omega C}}{R_L + \frac{1}{j2\omega C}} \quad (C3)$$

From (C3), the magnitude $|Z(j2\omega)|$ and phase ψ of the impedance $Z(j2\omega)$ in terms of ω_N , κ , ρ , and R_L is

$$|Z(j2\omega)| = R_L \sqrt{\frac{(\rho+1-4\omega_N^2)^2 + (2\kappa + (2\rho\omega_N^2)/\kappa)^2}{1 + (4\omega_N^4/\kappa^2)}} \quad (C4)$$

$$\begin{aligned} \psi = & \arctan \left[(2\kappa + (2\rho\omega_N^2)/\kappa) / (\rho+1-4\omega_N^2) \right] \\ & - \arctan \left[(2\omega_N^2)/\kappa \right] \end{aligned} \quad (C5)$$

Following the method in Appendix A, i_X and v_0 are given by

$$i_X = - \frac{4V_{Im} \sqrt{1 + (4\omega_N^4)/\kappa^2}}{3\pi R_L \sqrt{(\rho+1-4\omega_N^2)^2 + (2\kappa + (2\rho\omega_N^2)/\kappa)^2}} \cos(2\omega t - \psi) \quad (C6)$$

$$v_0 = - \frac{4V_{Im}}{3\pi \sqrt{(\rho+1-4\omega_N^2)^2 + (2\kappa + 2\rho\omega_N^2/\kappa)^2}} \cos(2\omega t - \psi + \phi) \quad (C7)$$

Adding the two responses, the total inductor current and output voltage is obtained as

$$i_X = \frac{4V_{Im}}{\pi R_L} \left[\frac{1}{2(\rho+1)} - \frac{\sqrt{1 + (4\omega_N^4)/\kappa^2}}{3 \sqrt{(\rho+1-4\omega_N^2)^2 + (2\kappa + 2\rho\omega_N^2/\kappa)^2}} \cos(2\omega t - \psi) \right] \quad (C8)$$

$$v_0 = \frac{4V_{Im}}{\pi} \left[\frac{1}{2(\rho+1)} - \frac{1}{3 \sqrt{(\rho+1-4\omega_N^2)^2 + (2\kappa+2\rho\omega_N^2/\kappa)^2}} \cos(2\omega t - \psi + \phi) \right] \quad (C9)$$

From (C8), the dc output voltage V_0 and peak-to-peak ripple V_{Op} are given by

$$V_0 = \frac{2V_{Im}}{\pi(\rho+1)} \quad (C10)$$

$$V_{Op} = \frac{8V_{Im}}{3\pi \sqrt{(\rho+1-4\omega_N^2)^2 + (2\kappa+(2\rho\omega_N^2)/\kappa)^2}} \quad (C11)$$

From (C7), the rms and peak values of inductor current I_{Xe} and I_{Xm} are obtained from the expressions

$$I_{Xe} = \frac{4V_{Im}}{\pi R_L} \left[\sqrt{\frac{1}{4(\rho+1)^2} + \frac{(1+(4\omega_N^4)/\kappa^2)}{18((\rho+1-4\omega_N^2)^2 + (2\kappa+(2\rho\omega_N^2)/\kappa)^2)}} \right] \quad (C12)$$

$$I_{Xm} = \frac{4V_{Im}}{\pi R_L} \left[\frac{1}{2(\rho+1)} + \frac{\sqrt{(1+(4\omega_N^4)/\kappa^2)}}{3 \sqrt{(\rho+1-4\omega_N^2)^2 + (2\kappa+(2\rho\omega_N^2)/\kappa)^2}} \right] \quad (C13)$$

Appendix D

DERIVATION OF EXPRESSIONS FOR THE LC FILTER WITH NON-ZERO SOURCE IMPEDANCE OPERATING IN THE DISCONTINUOUS-CONDUCTION MODE, CHAPTER III

In this appendix, the derivations of the expressions for v_0 and i_x when the diodes are conducting in the discontinuous-conduction mode are presented. The derivations for the case when the diodes are not conducting is the same as given in Section B.2 of Appendix B, and will not be repeated here.

For the equivalent circuit shown in Figure 3.2A, the differential equation for v_{01} can be written following the procedure in Appendix B, Section B.1

$$\omega^2 LC \frac{d^2 v_{01}}{d\theta^2} + \left(\frac{\omega L}{R_L} + \omega R_I C \right) \frac{dv_{01}}{d\theta} + \left(\frac{R_I}{R_L} + 1 \right) v_{01} = V_{Im} \sin(\theta - \theta_0) \quad (D1)$$

Writing (D1) in terms of ω_N , κ , and ρ

$$\omega_N^2 \frac{d^2 v_{01}}{d\theta^2} + \kappa \rho \frac{dv_{01}}{d\theta} + (\rho + 1) v_{01} = V_{Im} \sin(\theta - \theta_0) \quad (D2)$$

where

$$\kappa_r = \kappa + (\rho\omega_N^2)/\kappa \quad (D3)$$

Solution for v_{01} :

As described in Appendix B, Section B.1, the particular solution for v_{01} can be obtained as

$$v_p = A_{vr} \sin\theta + B_{vr} \cos\theta \quad (D4)$$

where

$$A_{vr} = \frac{V_{Im} [\cos\theta_0(\rho+1-\omega_N^2) - \kappa_r \sin\theta_0]}{(\rho+1-\omega_N^2)^2 + \kappa_r^2} \quad (D5)$$

$$B_{vr} = \frac{V_{Im} [-\sin\theta_0(\rho+1-\omega_N^2) - \kappa_r \cos\theta_0]}{(\rho+1-\omega_N^2)^2 + \kappa_r^2} \quad (D6)$$

For the homogeneous part of the solution, the roots of the characteristic equation of (D2) are for the case $4\omega_N^2(\rho+1) > \kappa_r^2$

$$\lambda_{1,2} = \beta_r \pm j\alpha_r \quad (D7)$$

where

$$\beta_r = -\kappa_r/(2\omega_N^2) \quad (D8)$$

$$\alpha_r = (\sqrt{4\omega_N^2(\rho+1) - \kappa_r^2})/(2\omega_N^2) \quad (D9)$$

As in Appendix B-2, the solution for v_{01} and i_{X1} is found to be

$$v_{01}(\theta) = A_{vr} \sin \theta + B_{vr} \cos \theta + \exp(\beta_r \theta) [C_{vr} \sin \alpha_r \theta + D_{vr} \cos \alpha_r \theta] \quad (D10)$$

$$i_{X1}(\theta) = \frac{1}{R_L} [A_{ir} \sin \theta + B_{ir} \cos \theta + \exp(\beta_r \theta) \{C_{ir} \sin \alpha_r \theta + D_{ir} \cos \alpha_r \theta\}] \quad (D11)$$

For the case $\kappa_r^2 > 4\omega_N^2(\rho+1)$, the roots of the characteristic equation are

$$\alpha_1 = \beta_r + \alpha' \quad (D12)$$

$$\alpha_2 = \beta_r - \alpha' \quad (D13)$$

where

$$\alpha' = \frac{\sqrt{\kappa_r^2 - 4\omega_N^2(\rho+1)}}{2\omega_N^2} \quad (D14)$$

The solution for v_{01} and i_{X1} is obtained as

$$v_{01}(\theta) = A_{vr} \sin \theta + B_{vr} \cos \theta + C'_{vr} \exp(\alpha_1 \theta) + D'_{vr} \exp(\alpha_2 \theta) \quad (D15)$$

$$i_{X1}(\theta) = \frac{1}{R_L} [A_{ir} \sin \theta + B_{ir} \cos \theta + C'_{ir} \exp(\alpha_1 \theta) + D'_{ir} \exp(\alpha_2 \theta)] \quad (D16)$$

where

$$A_{ir} = A_{vr} - \frac{\omega_N^2 B_{vr}}{\kappa} \quad (D17)$$

$$B_{ir} = B_{vr} + \frac{\omega_N^2 A_{vr}}{\kappa} \quad (D18)$$

$$C'_{ir} = C'_{vr}(1+(\omega_N^2\alpha_1)/\kappa^2) \quad (D19)$$

$$D'_{ir} = D'_{vr}(1+(\omega_N^2\alpha_2)/\kappa^2) \quad (D20)$$

Where C_{vr} , D_{vr} , C'_{vr} , and D'_{vr} are given as follows:

$$C_{vr} = [(-\kappa V_{Im} \sin \theta_0 / \omega_N^2) - A_{vr} - \beta_r (V_{Im} \sin \theta_0 - B_{vr})] / \alpha_r \quad (D21)$$

$$D_{vr} = V_{Im} \sin \theta_0 - B_{vr} \quad (D22)$$

$$C'_{vr} = [\alpha_2 (V_{Im} \sin \theta_0 - B_{vr}) + (\kappa V_{Im} \sin \theta_0 / \omega_N^2) + A_{vr}] / (\alpha_2 - \alpha_1) \quad (D23)$$

$$D'_{vr} = [(\kappa V_{Im} \sin \theta_0 / \omega_N^2) + A_{vr} + \alpha_1 (V_{Im} \sin \theta_0 - B_{vr})] / (\alpha_2 - \alpha_1) \quad (D24)$$

Appendix E

DERIVATION OF $F_1(\hat{B}_{mAC}, \mu_\Delta, H_{mQ}, L, I_{DC}, V_{AC}, f, \ell_m, A_m) = 0$, CHAPTER IV

Referring to Figure 4.2, it can be seen that the negative air-gap line passes through the point $(NI_{DC}/\ell_m, 0)$ with a slope equal to $-\mu_0 \ell_m/\ell_g$ and intersects the normal magnetization curve at the point (H_{mQ}, B_{mQ}) . The negative air-gap line equation can be written:

$$B_g = \mu_0(NI_{DC} - \ell_m H)/\ell_g \quad (E1)$$

where N is the number of winding turns and μ_0 is the permeability of free space. Substituting H_{mQ} and B_{mQ} for H and B_g and rearranging (E1) leads to an expression for N .

$$N = (\ell_g B_{mQ} + \ell_m \mu_0 H_{mQ})/\mu_0 I_{DC} \quad (E2)$$

Inductance L for the winding is given by the expression

$$L = \mu_0 \left(\frac{\mu_\Delta}{1 + \mu_\Delta (\ell_g/\ell_m)} \right) \left(\frac{N^2 A_m}{\ell_m} \right) \quad (E3)$$

where μ_Δ is the relative incremental permeability for the core material at a given operating point [20]. Substituting (E2) into (E3) and multiplying the result by $\ell_m [\mu + \mu_\Delta (\ell_g/\ell_m)]$ yields

$$L\ell_m[1+\mu_\Delta(\ell_g/\ell_m)] = \mu_\Delta A_m(\ell_g B_{mQ} + \ell_m \mu_0 H_{mQ})^2 / \mu_0 I_{DC}^2 \quad (E4)$$

which can be rearranged and simplified to

$$\begin{aligned} \ell_g^2 + [2\ell_m \mu_0 H_{mQ} B_{mQ} A_m - \mu_0 I_{DC}^2 L] / A_m B_{mQ}^2 \ell_g \\ + [(\ell_m^2 \mu_0^2 H_{mQ}^2 / B_{mQ}^2) - (\mu_0 I_{DC}^2 L \ell_m / A_m B_{mQ}^2 \mu_\Delta)] = 0 \end{aligned} \quad (E5)$$

Equation (E5) can be written in terms of ℓ_g, μ_Δ and constants as

$$\ell_g^2 + K_1 \ell_g + K_2 - K_3 / \mu_\Delta = 0 \quad (E6)$$

where K_1, K_2 , and K_3 are defined in (4.4), (4.5), and (4.6) respectively.

Roots of ℓ_g for the quadratic equation (E6) in ℓ_g are given by (E7) in which only the positive sign for the square root term can lead to a meaningful physical value for ℓ_g and therefore is shown in the expression. This is shown in Appendix G.

$$\ell_g = 0.5[-K_1 + \sqrt{K_1^2 - 4[K_2 - (K_3/\mu_\Delta)]}] \quad (E7)$$

To determine the remaining unknown quantity μ_Δ in (E7), the peak ac flux density \hat{B}_{mAC} must be found. \hat{B}_{mAC} is related to the rms ac voltage across the winding for the assumed sinusoidal fundamental frequency component as follows:

$$V_{AC} = \sqrt{2} \pi N f A_m \hat{B}_{mAC} \quad (E8)$$

Rearranging (E8) to obtain an expression for N and then squaring leads to

$$N^2 = K_4 / \hat{B}_{mAC}^2 \quad (E9)$$

where K_4 is given by (4.7).

Substituting the expression for N^2 in (E9) and the expression for x_g from (E7) into the equation for L given by (E3) leads to the relationship (E10) which is the desired form $F_1(\cdot) = 0$.

$$F_1(\cdot) = K_6 \left[\frac{K_5}{\mu_\Delta} - K_1 + \sqrt{K_1^2 - 4\left(K_2 - \frac{K_3}{\mu_\Delta}\right)} \right] - \frac{K_4}{\hat{B}_{mAC}^2} = 0 \quad (E10)$$

where K_5 and K_6 are defined by (4.8) and (4.9).

Appendix F
DERIVATION OF THE SCREENING RULE FOR A PHYSICALLY
REALIZABLE AIR GAP, CHAPTER IV

The screening process included in Flow Chart 3, Figure 4.7, is based on the consideration that, for the air gap to be physically realizable, the expression for ℓ_g given by (E7) in Appendix E and in the text as (4.11) must yield a real positive quantity. Two sets of conditions will be considered by examining the value of the expression for K_1 given by (4.4) and repeated here as (F1)

$$K_1 = \mu_0 (2\ell_m A_m H_{mQ} B_{mQ} - I_{DC}^2 L) / A_m B_{mQ}^2 \quad (F1)$$

The parameter K_1 can also be expressed in terms of K_2 and K_3 , which are defined by (4.5) and (4.6), and is given by (F2)

$$K_1 = 2\sqrt{K_2} - (K_3/\ell_m) \quad (F2)$$

Case I: $K_1 \leq 0$

Using the definition of K_1 in (F1), the inequality $K_1 \leq 0$ is equivalent to the inequality (F3)

$$I_{DC}^2 L / 2\ell_m A_m \geq H_{mQ} B_{mQ} \quad (F3)$$

and using (F2), it is equivalent to the inequality

$$(K_3/\ell_m) \geq 2\sqrt{K_2} \quad (F4)$$

The specification-dependent parameter K_8 used in the screening process and calculated in Step [I] of Flow Chart 3 is defined as

$$K_8 \triangleq I_{DC}^2 L / 2\ell_m A_m \quad (F5)$$

Thus, for K_1 to be equal to or less than zero, (F6) must be satisfied

$$K_8 \geq H_{mQ} B_{mQ} \quad (F6)$$

Under this condition, ℓ_g will be a real number if the discriminant in (E7) is equal to or greater than zero or if

$$K_1^2 + (4K_3/\mu_\Delta) \geq 4K_2 \quad (F7)$$

Using the value of K_1 from (F2), the inequality in (F7) reduces to

$$(K_3/\ell_m) + (4\ell_m/\mu_\Delta) \geq 4\sqrt{K_2} \quad (F8)$$

Since (F4) holds for the case under consideration, the smallest value for the left side of (F8) occurs with the equality sign in (F4). From (F8), for ℓ_g always to be a real number with any combination of ℓ_m , μ_Δ , K_2 , and K_3 , then

$$(4\ell_m/\mu_\Delta) > 2\sqrt{K_2} \quad (F9)$$

Using the value for K_2 from (4.5) in this expression leads to the inequality (F10)

$$2B_{mQ}/\mu_0\mu_{\Delta}H_{mQ} > 1 \quad (F10)$$

For essentially all quiescent or bias points and all magnetic materials (F10) is satisfied. Therefore, when the inequality expressed by (F6) and shown in Step [J] in Flow Chart 3 is satisfied, the selected core and quiescent point are satisfactory for continuation of the design procedure.

Case II: $K_1 > 0$

For this condition, which corresponds to $K_8 < H_{mQ}B_{mQ}$, in order for ℓ_g to be a real positive number,

$$K_3/\mu_{\Delta} > K_2 \quad (F11)$$

Using the expressions for K_2 and K_3 from (4.5) and (4.6) and rearranging terms leads to inequality (F12) which must be satisfied for a core to be considered further.

$$K_8 > \mu_0(H_{mQ}^2\mu_{\Delta Q})/2 \quad (F12)$$

When the inequality expressed in (F12) and shown in Step [K] in Flow Chart 3 is satisfied, the selected core and quiescent point are satisfactory and the design procedure may be continued.

If (F12) is not satisfied, a final test is made which compares K_8 with the value of $\mu_0(H_{mQ}^2\mu_{\Delta Q})_{\min}/2$. The parameter $\mu_0(H_{mQ}^2\mu_{\Delta Q})_{\min}/2$ is the

minimum value that the product $\mu_0(H_{mQ}^2\mu_{\Delta Q})/2$ can take on over the range of the magnetic core material data available. If inequality (F13), shown as Step [L] in Flow Chart 3, is satisfied,

$$K_8 \geq \mu_0(H_{mQ}^2\mu_{\Delta Q})_{\min}/2 \quad (F13)$$

Then choosing a new value of H_{mQ} in Step [N], which will satisfy the inequality (F12) in Step [K], will allow the continuation of the design procedure. If (F13) is not satisfied, a larger core must be selected and the screening procedure re-entered.

Appendix G

DISCUSSION ON THE QUADRATIC ROOTS FOR ℓ_g , CHAPTER IV

As mentioned in Appendix E, only the positive sign in front of the square root term is considered in the expression for ℓ_g given by (E7). With the negative sign, the expression for ℓ_g becomes

$$\ell_g = 0.5[-K_1 - \sqrt{K_1^2 - 4[K_2 - (K_3/\mu_\Delta)]}] \quad (G1)$$

Case I: $K_1 \leq 0$

Using the definition of K_1 in (F1), the inequality $K_1 \leq 0$ is equivalent to the inequality (G2)

$$I_{DC}^2 L \geq 2\ell_m A_m H_{mQ} B_{mQ} \quad (G2)$$

Inequality (F10) given in Appendix F, which is easily satisfied for essentially all magnetic materials and bias points, is rearranged as follows

$$\mu_0 \mu_\Delta H_{mQ} / B_{mQ} < 2 \quad (G3)$$

Substituting for 2 in (G2) from (G3) leads to inequality (G4)

$$I_{DC}^2 L > \mu_0 \mu_\Delta \ell_m A_m H_{mQ}^2 \quad (G4)$$

Let

$$K_{11} = K_2 - (K_3/\mu_\Delta) \quad (G5)$$

From (4.5) and (4.6)

$$\begin{aligned} K_{11} &= (\mu_0^2 \ell_m^2 H_m^2 / B_{mQ}^2) - (\mu_0 \ell_m I_{DC}^2 L / A_m B_{mQ}^2 \mu_\Delta) \\ &= \frac{\mu_0 \ell_m}{A_m B_{mQ}^2 \mu_\Delta} [\mu_0 \mu_\Delta \ell_m A_m H_m^2 - I_{DC}^2 L] \end{aligned} \quad (G6)$$

From (G4) and (G5)

$$K_{11} < 0 \quad (G7)$$

Expression for ℓ_g in terms of K_1 and K_{11} is

$$\ell_g = 0.5[K_1 - \sqrt{K_1^2 - 4K_{11}}] \quad (G8)$$

From (G7) and (G8) it is seen that gap ℓ_g is a negative quantity which is not physically realizable.

Case II: $K_1 > 0$

From (G1), ℓ_g is either a negative real number or a complex number neither of which is physically realizable.

APPENDIX H

ALGORITHMS FOR GENERATING DESIGN CURVES FOR AIR- GAPPED INDUCTORS, CHAPTER V

The algorithms used in generating design curves are explained in this appendix by reference to the flow chart presented in Figure H.1. In the flow chart, starting with an assigned value of air gap ratio ℓ_g/ℓ_m and an initial quiescent point (H_{mQ}, B_{mQ}) on the normal magnetization curve, a value for design parameter LI_{DC}^2/ν is computed for an initial value of $\hat{B}_{mAC, \min}$ using relationship (5.14). The procedure continues by iteratively selecting additional quiescent points until values for LI_{DC}^2/ν corresponding to $\hat{B}_{mAC, \min}$ for all the quiescent points are obtained. The value of $H_{mQ} = H_{mQ, \text{opt}}$ at the quiescent point (H_{mQ}, B_{mQ}) which corresponds to the maximum value of LI_{DC}^2/ν , is used to generate design curves of LI_{DC}^2/ν versus \hat{B}_{mAC} for various values of air-gap ratios using the corresponding $H_{mQ, \text{opt}}$ for H_{mQ} in (5.14).

H.1 Flow Chart

In the procedure illustrated in the flow chart in Figure H.1, a search is made for the optimum quiescent point $H_{mQ, \text{opt}}$ for a specified air-gap ratio which yields the maximum value of LI_{DC}^2/ν . The value for the

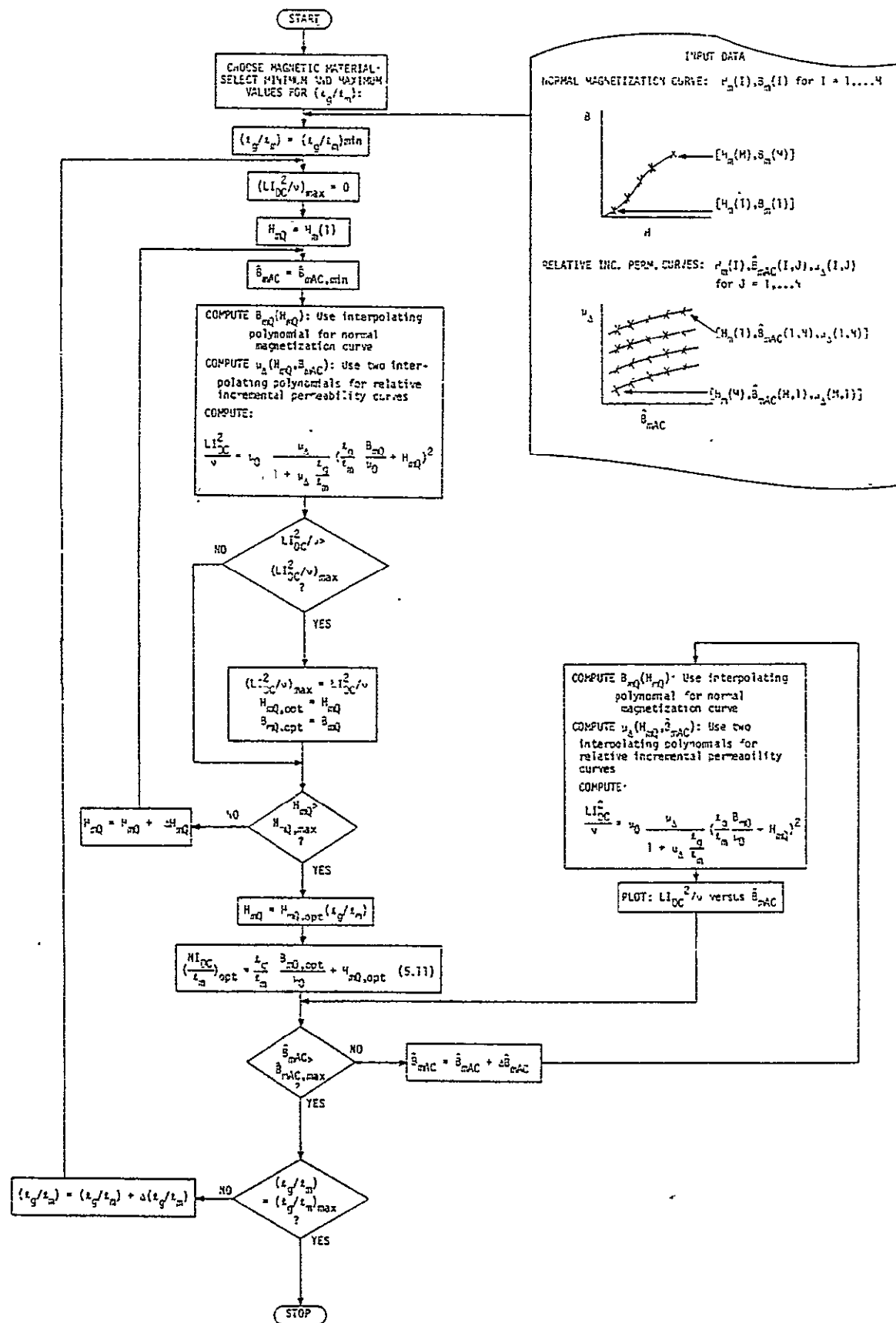


Figure H.1. Flow chart illustrating the algorithm for calculating the optimum quiescent point $H_{mQ, \text{opt}}$, and generating design curves for various air-gap ratios.

corresponding $H_{mQ,opt}(\ell_g/\ell_m)$ is used for the dc operating point H_{mQ} in (5.14) to generate design curves of LI_{DC}^2/ν versus \hat{B}_{mAC} , shown in Figures 5.5, 5.6, and 5.7. The operation begins with the assignment of minimum and maximum values for the air-gap ratio and the choosing of the magnetic material. The data base for the designated core material includes sample points taken from the normal magnetization curve and from a family of relative incremental permeability curves for the chosen material, as described in Flow Chart 2, Figure 4.5, in Chapter IV.

Starting with the first sample point $[H_m(1), B_m(1)]$ on the normal magnetization curve, and using an interpolating polynomial method to approximate the values of B_{mQ} , and μ_Δ for $\hat{B}_{mAC,min}$, as described in Chapter IV, the value for LI_{DC}^2/ν is calculated from (5.14) and stored. This quiescent value H_{mQ} is then incremented by a prescribed amount ΔH_m and the above procedure is repeated until the specified maximum value for the quiescent point $H_{mQ,max}$ is exceeded. The value of $H_{mQ} = H_{mQ,opt}$ corresponding to the maximum value of LI_{DC}^2/ν is used now in generating design curve for the specified air-gap ratio.

Using the method of an interpolating polynomial to approximate values of B_{mQ} and μ_Δ corresponding to $H_{mQ,opt}$ and various values of \hat{B}_{mAC} , LI_{DC}^2/ν is computed from (5.14). A curve of LI_{DC}^2/ν versus \hat{B}_{mAC} is obtained for the specified air-gap ratio. The value for $(NI_{DC}/\ell_m)_{opt}$ corresponding to $H_{mQ,opt}$ for the specified air-gap ratio is calculated from (5.15). The air-gap ratio is then incremented by a prescribed amount $\Delta(\ell_g/\ell_m)$ and the above procedure is repeated. A family of design curves for grain-oriented 3-percent silicon steel, obtained in this manner are shown in Figure 5.3.

LIST OF REFERENCES

160

LIST OF REFERENCES

- [1] M. B. Stout, "Analysis of Rectifier Filter Circuits," Electrical Engineering, September 1935, Vol. 54, pp. 977-984.
- [2] O. H. Schade, "Analysis of Rectifier Operations," Proceedings of the IRE, July 1943, pp. 341-361.
- [3] Reuben Lee, Electronic Transformers and Circuits, Book, John Wiley and Sons, Inc., 1947, pp. 111-139.
- [4] Solid-State Power Circuits Designer's Handbook, RCA Technical Series, SP-52, 1971, pp. 253-261.
- [5] J. R. Nowicki, Power Supplies for Electronic Equipment, Book, CRC Press, pp. 64-184, 1971.
- [6] F. C. Schwarz, "A Time-Domain Analysis of the Power Factor for a Rectifier Filter System with Over- and Subcritical-Inductance," IEEE Transactions on Industrial Electronics and Control, Vol. IECI-20, May 1973, pp. 61-68.
- [7] T. T. Nishizaki, R. G. Aiken, and G. J. R. St. Amand, "Computer-Aided Design and Weight Estimation of High-Power High-Voltage Power Conditioners," IEEE Trans. Aerospace and Electronic Systems, Vol. AES-7, pp. 1179-1194, November 1971.
- [8] H. A. Owen, Jr., T. G. Wilson, S. Y. Feng, and F. C. Y. Lee, "A Computer-Aided Design Procedure for Flyback Step-up DC-to-DC Converters," IEEE Trans. Magnetics, Vol. MAG-8, pp. 289-291, September 1972.
- [9] D. Y. Chen, H. A. Owen, Jr. and T. G. Wilson, "Computer-Aided Design and Graphics Applied to the Study of Inductor-Energy-Storage DC-to-DC Electronic Power Converters," IEEE Trans. on Aerospace and Electronic Systems, Vol. AES-9, No. 4, July 1973, pp. 585-597.
- [10] D. Y. Chen, H. A. Owen, Jr. and T. G. Wilson, "Design of Two-Winding Voltage Step-up/Current Step-up Constant-Frequency DC-to-DC Converters," IEEE Trans. on Magnetics, Vol. MAG-9, No. 3, September 1973, pp. 252-256.

- [11] D. Y. Chen, H. A. Owen, Jr. and T. G. Wilson, "Design of Energy-Storage Transformers for Two-Winding Voltage Step-up/Current Step-up Converters With Constant On-Time and Constant Off-Time Controllers," Digest of the 1975 IEEE INTERMAG Conference, April 14-17, 1975, London, England.
- [12] D. Y. Chen, H. A. Owen, Jr., T. G. Wilson, "Table-Aided Design of the Energy-Storage Reactor in DC-to-DC Converters," IEEE Transactions on Aerospace and Electronic Systems, Vol. AES-12, No. 3, May 1976, pp. 374-386.
- [13] A. K. Ohri, T. G. Wilson, H. A. Owen, Jr., "Design of Air-Gapped Magnetic-Core Inductors for Superimposed Direct and Alternating Currents," IEEE Transactions on Magnetics, Vol. MAG-12, No. 5, September, 1976, pp. 564-574.
- [14] A. K. Ohri, T. G. Wilson, H. A. Owen, Jr., "Analysis and Design of a Rectifier LC-Filter Circuit for Continuous- and Discontinuous-Conduction Modes," 1975 Proceedings of Applied Magnetics Workshop, IEEE Publication 75 CHO 964-7 MAG, pp. 3B4.1-3B4.22 (June 1975).
- [15] A. K. Ohri, T. G. Wilson, H. A. Owen, Jr., "Design of Single-Winding Energy-Storage Reactors for DC-to-DC Converters Using Air-Gapped Magnetic-Core Structures," to be presented at the 1977 INTERMAG, Los Angeles, June 6-9, 1977.
- [16] C. R. Hanna, "Design of Reactances and Transformers Which Carry Direct Current," Transactions AIEE, Vol. 46, February 1927, pp. 155-160.
- [17] W. P. Kornrumpf and J. P. Walden, "Power Factor of Active Filtering Systems," IEEE Power Electronics Specialists Conference Record, June 1976, pp. 318-325.
- [18] R. C. Ray, E. F. Sartori, "Computer Design of an Inductor Carrying Direct Current," IEEE Transactions on Magnetics, Vol. MAG-7, No. 3, September 1971, pp. 453-455.
- [19] W. T. Mitchell, "Computer Aided Design of AC Inductors with Superimposed DC Using Ferromagnetic Cores," Proceedings of the Workshop on Applied Magnetics, May 1972, pp. 98-101.
- [20] N. R. Grossner, Transformers for Electronic Circuits. New York: McGraw-Hill, 1967, p. 132.
- [21] Hypersil Core Design Engineer's Handbook, Westinghouse Electric Corp., Catalog, 1965, p. F-12.

- [22] Tape Wound Cores, Arnold Engineering Co., Catalog TC0101B, 1972, p. 54.
- [23] B. Carnahan, H. A. Luther, and J. O. Wilkes, Applied Numerical Methods. New York: Wiley, 1964, pp. 27-34.

GLOSSARY OF SYMBOLS

164

GLOSSARY OF SYMBOLS

a_0 to a_3	=	numerical coefficients used in approximate relationships given in Table 3.2 and in Table 3.3, numeric
A_g	=	cross-sectional area of air gap, m^2
A_i	=	$(-B_v \omega_N^2 / \kappa) + A_v$, V
A_{ir}	=	$(-B_{vr} \omega_N^2 / \kappa) + A_{vr}$, V
A_m	=	cross-sectional area of magnetic core material, m^2
$A_{m,min}$	=	minimum value of cross-sectional area of magnetic core as determined from minimum air-gap volume requirement, m^2
A_v	=	$[V_{Im}(\cos \theta_0(1 - \omega_N^2) - \kappa \sin \theta_0)] / [(1 - \omega_N^2)^2 + \kappa^2]$, V
A_{vr}	=	$[V_{Im}(\cos \theta_0(\rho + 1 - \omega_N^2) - \kappa_r \sin \theta_0)] / [(\rho + 1 - \omega_N^2)^2 + \kappa_r^2]$, V
A_{wn}	=	area of magnetic core window, m^2
A_{wr}	=	cross-sectional area of wire, including insulation, m^2
b_0 to b_3	=	numerical coefficients used in approximate relationships given in Table 3.2 and in Table 3.3, numeric
B	=	flux density in a magnetic circuit, T
B_g	=	flux density in air gap, T
B_i	=	$(A_v \omega_N^2 / \kappa) + B_v$, V
B_{ir}	=	$(A_{vr} \omega_N^2 / \kappa) + B_{vr}$, V
B_m	=	flux density in magnetic material, T; corresponds to values on the normal magnetization curve
B_{max}	=	maximum allowable core flux density, T

\hat{B}_{mAC}	=	peak value of the fundamental component of the ac flux density in magnetic material, T
$\hat{B}_{mAC,max}$	=	maximum value of \hat{B}_{mAC} for a particular value of H_{mQ} as determined from incremental permeability data, T
$\hat{B}_{mAC,min}$	=	minimum value of \hat{B}_{mAC} for a particular value of H_{mQ} as determined from incremental permeability data, T
B_{mDC}	=	average or direct component of B_m , T
B_{mQ}	=	selected quiescent or bias-point value of B_m , T
$B_{mQ,opt}$	=	value of B_{mQ} corresponding to optimum (minimum) turns for a specified value of inductance, T
B_R	=	residual core flux density, T
B_V	=	$-[V_{Im}(\sin\theta_0(1-\omega_N^2) + \kappa\cos\theta_0)]/[(1-\omega_N^2)^2 + \kappa^2]$, V
B_{vr}	=	$-[V_{Im}(\sin\theta_0(\rho+1-\omega_N^2) - \kappa_r\cos\theta_0)]/[(\rho+1-\omega_N^2)^2 + \kappa_r^2]$, V
c_1 to c_3	=	numerical coefficients used in approximate relationships given in Table 3.2 and in Table 3.3, <u>numeric</u>
C	=	capacitance value of the output capacitor, F
C_i	=	$(\omega_N^2(\beta C_V - \alpha D_V)/\kappa) + C_V$, V
C_{ir}	=	$(\omega_N^2(\beta_r C_{vr} - \alpha_r D_{vr})/\kappa) + C_{vr}$, V
C'_{ir}	=	$C'_{vr}[(\omega_N^2\alpha_1)/\kappa] + 1$, V
CU	=	symbol used to identify current stepup power stage
C_V	=	$[(-\kappa V_{Im}\sin\theta_0/\omega_N^2) - A_V - \beta(V_{Im}\sin\theta_0 - B_V)]/\alpha$, V
C_{vr}	=	$[(-\kappa V_{Im}\sin\theta_0/\omega_N^2) - A_{vr} - \beta_r(V_{Im}\sin\theta_0 - B_{vr})]/\alpha_r$, V
C'_{vr}	=	$[\alpha_2(V_{Im}\sin\theta_0 - B_{vr}) + (\kappa V_{Im}\sin\theta_0/\omega_N^2) + A_{vr}]/(\alpha_2 - \alpha_1)$, V
d_1 to d_3	=	numerical coefficients used in approximate relationships given in Table 3.2 and in Table 3.3, <u>numeric</u>
D_i	=	$\omega_N^2(\beta D_V + \alpha C_V)/\kappa + D_V$, V
D_{ir}	=	$\omega_N^2(\beta_r D_{vr} + \alpha_r C_{vr})/\kappa + D_{vr}$, V

D'_{ir}	=	$D'_{vr}[(\omega_N^2 \alpha_1)/\kappa] + 1$, V
D_v	=	$V_{Im} \sin \theta_0 - B_v$, V
D_{vr}	=	$V_{Im} \sin \theta_0 - B_{vr}$, V
D'_{vr}	=	$-[(\kappa V_{Im} \sin \theta_0 / \omega_N^2) + A_{vr} + \alpha_1 (V_{Im} \sin \theta_0 - B_{vr})]/(\alpha_2 - \alpha_1)$, V
f	=	frequency of the fundamental component of voltage across the reactor, Hz
FQ	=	symbol used to identify constant frequency controller
F_w	=	winding factor, numeric
$F_{w,max}$	=	maximum permissible winding factor, numeric
H	=	magnetizing force, A/m
H_g	=	magnetizing force in air gap, A/m
H_m	=	magnetizing force in magnetic material, A/m; corresponds to values on normal magnetization curve
H_{mDC}	=	average or direct component of H_m , A/m
H_{mQ}	=	selected quiescent or bias-point value of H_m , A/m
$H_{mQ,opt}$	=	value of H_{mQ} corresponding to optimum (minimum) turns for a specified value of inductance, A/m
I_{DC}	=	maximum of the average or direct component of inductor current, A
I_{Ie}	=	effective or rms value of input current, A
i_0	=	instantaneous value of output current, A
i_{01}	=	instantaneous value of output current when diodes are conducting, A
i_{02}	=	instantaneous value of output current when diodes stop conducting, A
I_0	=	average output current, A

i_p	=	instantaneous value of current in the primary winding of transformer, A
I_{Pe}	=	effective or rms value of current in the primary winding of transformer, A
I_{Pm}	=	peak value of primary current, A
i_{S1}, i_{S2}	=	instantaneous value of currents in one of the secondary winding of the transformer, A
I_{Se}	=	effective or rms value of current in each secondary winding of the transformer, A
I_{Sm}	=	peak value of secondary current, A
i_X	=	instantaneous value of inductor current, A
i_{X1}	=	instantaneous value of inductor current when diodes are conducting, A
i_{X2}	=	instantaneous value of inductor current when diodes stop conducting, A
I_{Xe}	=	effective or rms value of inductor current, A
$I_{Xe,max}$	=	maximum value of effective inductor current, A
I_{Xm}	=	peak value of inductor current, A
K_1	=	$\mu_0 (2\ell_m A_m H_{mQ} B_{mQ} - I_{DC}^2 L) / A_m B_{mQ}^2, m$
K_2	=	$(\mu_0 \ell_m H_{mQ} / B_{mQ})^2, m^2$
K_3	=	$\mu_0 \ell_m I_{DC}^2 L / A_m B_{mQ}^2, m^2$
K_4	=	$(V_{AC} / \sqrt{2} \pi f A_m)^2, T^2$
K_5	=	$2\ell_m, m$
K_6	=	$L / 2\mu_0 A_m, m^{-1}$
K_7	=	$-K_1 + \sqrt{K_1^2 - 4[K_2 - (K_3/\mu_\Delta)]}, m$
K_8	=	$I_{DC}^2 L / 2\ell_m A_m, HA^2/m^3$

$$K_9 = 1 + [1 - (\zeta/\delta)(A_{m,\min}/A_m)]^{1/2} = 1 + [1 - (\zeta/\delta)(\ell_{g,\min}/\ell_g)]^{1/2},$$

numeric

$$K_{10} = \begin{cases} (V_0/2P_{0,\max})(V_{I,\min}-V_Q)(B_{\max}-B_R)/(V_0+V_D-V_Q), VU, (AT)^{-1} \\ (V_0/2P_{0,\max})(B_{\max}-B_R), CU, (AT)^{-1} \\ (V_0/2P_{0,\max})(V_{I,\min}-V_Q)(B_{\max}-B_R)/(V_{I,\min}+V_0+V_D-V_Q), UD, (AT)^{-1} \\ (V_0/2P_{0,\max})(V_{I,\min}-V_Q)(B_{\max}-B_R)/((V_{I,\min}-V_Q)+V_0+V_D), 2UD, (AT)^{-1} \end{cases}$$

$$K_{11} = \frac{\mu_0 \ell_m}{A_m B_{mQ}^2 \mu_\Delta} [\mu_0 \mu_\Delta \ell_m / A_m H_{mQ}^2 - I_{DC}^2 L], m^2$$

$$\ell_g = \text{length of air gap, m}$$

$$\ell_{g,\min} = \text{minimum value of air-gap as determined from minimum air-gap volume requirements, m}$$

$$\ell_{g,\text{opt}} = \text{length of air gap corresponding to optimum (minimum) turns for a specified value of inductance, m}$$

$$\ell_m = \text{mean magnetic path length in the magnetic core material, m}$$

$$L = \text{inductance value of inductor, H}$$

$$L_I = \text{effective inductance associated with input voltage source as referred to the secondary side of the transformer, H}$$

$$L_p = \text{inductance of primary winding, H}$$

$$L_s = \text{inductance of secondary winding, H}$$

$$n = \text{harmonic number in the fourier series expansion of input voltage, numeric}$$

$$N = \text{number of turns on inductor winding, numeric}$$

$$N_{\min} = \text{minimum number of turns on inductor winding for a specified value of inductance, using a given core material, geometry and air gap, numeric}$$

$$N_p = \text{number of turns on the primary winding, numeric}$$

N_S	=	number of turns on each secondary winding, numeric
P.F.	=	power factor of the rectifier-filter circuit, numeric
$P_{O,max}$	=	maximum value of average output power, W
Q	=	quality factor of the filter at resonant frequency, numeric
R_I	=	effective resistance associated with input source as referred to the secondary side of the transformer, Ω
R_L	=	output load resistance, Ω
t	=	time, s
t_{off}	=	transistor cut-off interval, s
t_{on}	=	transistor conduction interval, s
T	=	period of one conversion cycle, s
TF	=	symbol used to identify constant off-time controller
TN	=	symbol used to identify constant on-time controller
U_y	=	option constraint quantity, $y = A, B, C, D, E, H,$ or J ; units depend on option
UD	=	symbol used to identify single winding voltage stepup/current stepup power stage
2UD	=	symbol used to identify two winding voltage stepup/current stepup power stage
V_{AC}	=	minimum of the rms or effective value of the fundamental alternating component of voltage across the inductor, V
V_D	=	diode forward voltage drop, V
V_I	=	converter DC input voltage, V
V_{Ie}	=	effective or rms value of ac input voltage to the rectifier-filter circuit, V
V_{Im}	=	peak value of the sinusoidal input voltage, V

$V_{I,max}$	=	maximum converter input voltage, V
$V_{I,min}$	=	minimum converter input voltage, V
v_h	=	instantaneous output voltage due to homogeneous part of the differential equation, V
v_0	=	instantaneous value of output voltage, V
v_{01}	=	instantaneous value of output voltage when diodes are conducting, V
v_{02}	=	instantaneous value of output voltage when diodes stop conducting, V
V_0	=	dc output voltage, V
V_{0e}	=	effective or rms value of output voltage, V
V_{0p}	=	peak-to-peak output ripple voltage, V
v_p	=	instantaneous output voltage due to forcing function of differential equation only, V
V_Q	=	transistor saturation voltage drop, V
VU	=	symbol used to identify voltage stepup power stage
$ Z(j2w) $	=	magnitude of the filter impedance seen from the source at the second harmonic of the sinusoidal ac supply, Ω
$ Z_1(j2w) $	=	magnitude of the parallel combination of filter load and capacitance at the second harmonic of the sinusoidal ac supply, Ω
α	=	$\sqrt{4\omega_N^2 - \kappa^2} / (2\omega_N^2)$, numeric
α'	=	$\sqrt{(\kappa_r^2 - 4\omega_N^2(\rho+1))} / (2\omega_N^2)$, numeric
α_1	=	$\beta_r + \alpha'$, numeric
α_2	=	$\beta_r - \alpha'$, numeric
α_r	=	$\sqrt{4\omega_N^2(\rho+1) - \kappa_r^2} / (2\omega_N^2)$, numeric

β	=	$-\kappa/(2\omega_N^2)$, numeric
β_r	=	$-\kappa_r/(2\omega_N^2)$, numeric
γ	=	N_S/N_P = turns ratio, numeric
γ_y	=	turns ratio N_S/N_P for option y where y = A,B,C,D,E,H, or J, numeric
δ	=	computed quantity used in calculating minimum air-gap volume (Reference 12), m^4/H
ϵ_1	=	error term computed in solution for discontinuous mode, numeric
ϵ	=	error term computed in solution for μ_Δ and \hat{B}_{mAC} , numeric
ϵ_{max}	=	value of ϵ corresponding to $\mu_{\Delta,max}$ and $\hat{B}_{mAC,max}$, numeric
ϵ_{min}	=	value of ϵ corresponding to $\mu_{\Delta,min}$ and $\hat{B}_{mAC,min}$, numeric
ζ	=	computed quantity used in calculating δ , N, and N_P (Reference 12), m^4/H
θ	=	ωt , radians
θ_0	=	delay angle between beginning of sine pulse and resumption of inductor current in the discontinuous mode, radians
θ_1	=	end of the conduction interval in the discontinuous mode, radians
κ	=	$\omega L/R_L$, numeric
κ_r	=	$\kappa + (\rho\omega_N^2/\kappa)$, numeric
κ_{cr}	=	critical value of the parameter κ , numeric
λ	=	coefficient of the exponent in the solution for the discontinuous mode, numeric
μ_{DC}	=	relative normal permeability of the magnetic material, numeric

$\mu_{DC,eff}$	=	effective relative normal permeability of the air-gapped structure, numeric
μ_{eff}	=	effective permeability of the air-gapped structure, numeric
μ_0	=	permeability of free space, $4\pi \times 10^{-7}$ H/m
μ_{Δ}	=	relative incremental permeability, numeric
$\mu_{\Delta,eff}$	=	effective relative incremental permeability of the air-gapped structure, numeric
$\mu_{\Delta,max}$	=	maximum relative incremental permeability corresponding to $\hat{B}_{mAC,max}$, numeric
$\mu_{\Delta,min}$	=	minimum relative incremental permeability corresponding to $\hat{B}_{mAC,min}$, numeric
$\mu_{\Delta Q}$	=	$\mu_{\Delta}(H_{mQ}, \hat{B}_{mAC,max})$ = maximum value of μ_{Δ} on relative incremental permeability curve corresponding to the selected quiescent or bias point H_{mQ} , numeric
v	=	$\ell_m A_m$ = volume of magnetic core, m^3
v_{min}	=	minimum volume of the powder permalloy or ferrite toroidal cores, m^3
ξ	=	damping ratio, numeric
ρ	=	R_I/R_L = ratio of source resistance R_I to output load resistance R_L , numeric
ϕ	=	phase of the equivalent impedance resulting from parallel combination of filter load and capacitance at the second harmonic of the sinusoidal ac supply, Ω
ψ	=	phase of the filter impedance seen from the source at the second harmonic of the sinusoidal ac supply, radians

ω	=	$2\pi f$, angular frequency of the input sinusoidal source, radians/sec
ω_0	=	$1/\sqrt{LC}$, the natural angular frequency of the filter with zero damping, radians/sec
ω_N	=	ω/ω_0 , normalized angular frequency of the sinusoidal input source, numeric
$\Delta\epsilon$	=	range factor for comparison of error term ϵ , numeric
ΔH_m	=	incremental change in H_m used in optimization algorithm to determine minimum turns for a specified value of inductance, A/m
$\Delta(\ell_g/\ell_m)$	=	incremental change in (ℓ_g/ℓ_m) in the algorithm for generating design curves, numeric
$\Delta W_{m,max}$	=	maximum amount of energy transferred by core over a switching cycle, J

BIOGRAPHY

BIOGRAPHY

Name: Anil Kumar Ohri

Date of Birth: [REDACTED]

Place of Birth: [REDACTED]

Universities Attended:	Dates:	Degrees:	Dates of Degrees:
I.I.T. Kanpur; India	1965-1970	B.Tech	May 1970
Duke University	1970-1972	MSEE	May 1972
Duke University	1972-present		

Major: Electrical Engineering

Minor: Mathematics

Publications:

1. ———, with H. A. Owen, Jr., T. G. Wilson and G. Ernest Rodriguez, "Digital Computer Simulation of Inductor-Energy-Storage DC-TO-DC Converters with Closed-Loop Regulators," Proceedings of 1974 Spacecraft Power-Conditioning Electronics Seminar, ESRO SP-103, ESRIN, Frascati, Italy, pp. 245-261, September 1974.
2. ———, with T. G. Wilson, H. A. Owen, Jr., "Design of Air-Gapped Magnetic-Core Inductors for Superimposed Direct and Alternating Currents," IEEE Transactions on Magnetics, Vol. MAG-12, No. 5, September 1976, pp. 564-574.
3. ———, with T. G. Wilson, H. A. Owen, Jr., "Analysis and Design of a Rectifier LC-Filter Circuit for Continuous- and Discontinuous-Conduction Modes," 1975 Proceedings of Applied Magnetics Workshop, IEEE Publication 75 CHO 964-7 MAG, pp. 3B4.1-3B4.22 (June 1975).

4. ———, with T. G. Wilson, H. A. Owen, Jr., "Design of Type C Core Single-Winding Energy-Storage Reactors for DC-to-DC Converters," to be presented at the 1977 INTERMAG, Los Angeles, June 6-9, 1977.

Positions Held:

1. Part-time Teaching Assistant in the Department of Electrical Engineering, Duke University, September 1970-May 1972.
2. Research Assistant in the Spacecraft Systems Research Lab., Duke University, part-time from June 1972 to September 1973, full-time from October 1973 until present.